Thermal Kinetic Inductance Detector (TKIDs) camera: A pathfinder mm-wave polarimeter

Thesis by

Lorenzo Minutolo

In Partial Fulfillment of the Requirements for the
Degree of
Ph.D. in Physics

CALIFORNIA INSTITUTE OF TECHNOLOGY
Pasadena, California

2024
Defended May 29th, 2024

ACKNOWLEDGEMENTS

I extend my heartfelt gratitude to Dr. James Bock for his invaluable guidance, insightful advice, and sharp perspectives on complex problems, which have been instrumental in shaping my academic journey.

I am immensely grateful to Dr. Roger O'Brient for his mentorship and encouragement and for fostering my growth as a scientist. His belief in my abilities and his incentive to explore creative solutions to challenging problems have been as invaluable as his will to import me to this side of the pond. Really. Standing ovation.

A huge thanks to Dr. Bryan Steinbach for his relentless mentoring during the good times and uncompromising support during the tough times. Thanks also for all the time spent in the desert, in the mountains, on a blackboard, and in a lab. I feel lucky every time. His guidance, both inside and outside the laboratory, has been transformative, and his frankness has helped me carve my own path.

I am deeply indebted to Dr. Albert Wandui, not only for his infinite patience (yes, I know) but also for his steadfast backing, for all the late nights spent working together, and for our invaluable adventures. His friendship has made this journey all the more rewarding.

I also want to thank the whole Caltech ObsCos group for being a friendly and supportive environment in which to develop technology. Special mention to Nancy Rappard for helping me deal with tons of bureaucracy: I would never have been able to work as fast without Her.

I could not have done it, not even by chance, without my wife, Giorgia, whose support and inspiration have been the driving force behind my hard work and dedication. Thanks for making me a better man and for lighting up every day we spend together. It really does make sense with you.

I am also grateful to Salvatore, Roberto, Serena and Adriana for the late-night calls, the laughter, the tireless support, the mozzarelle, and encouragement to dream big. Forza Napoli, of course.

Last but certainly not least, I extend my heartfelt thanks to my mother, Maria Rosaria, for instilling in me the values and determination to pursue my dreams. Without her teachings, this journey would never have begun.

ABSTRACT

Thermal kinetic inductance detectors (TKIDs) are novel, superconductive, frequency-multiplexed bolometric detectors that promise the same noise performance as traditional transition-edge superconducting bolometers, but with ease of scalability to large array formats. This research starts with TKIDs being in the early stage of development. Readout hardware and strategies were developed to characterize the first batches of devices, still in the chips form containing a few detectors. The success of the TKIDs chips lead to a more in-depth exploration of the detector physics and the possibility to scale from chips containing tens of detectors to tiles counting hundreds. Novel characterization techniques were developed to deal with the testing of the arrays in a laboratory environment. Finally, the characterization of a science grade tile is detailed.

PUBLISHED CONTENT AND CONTRIBUTIONS

[1] P. Ade, Z. Ahmed, M. Amiri, et al. "Improved Constraints on Primordial Gravitational Waves Using Planck, Wmap, and Bicep/keck Observations Through the 2018 Observing Season". In: *Physical Letter Review* 127 (15 Oct. 2021), p. 151301. DOI: `10.1103/PhysRevLett.127.151301`. URL: `https://link.aps.org/doi/10.1103/PhysRevLett.127.151301`.
L.M. contributed to raw data quality control, instrument diagnostic and contributed to the development of diangostic tools.

[2] Shubh Agrawal, Bryan Steinbach, James J. Bock, et al. "Strong Negative Electrothermal Feedback In Thermal Kinetic Inductance Detectors". In: *Journal of Applied Physics* 130.12 (Sept. 2021), p. 124503. ISSN: 0021-8979. DOI: `10.1063/5.0064723`. eprint: `https://pubs.aip.org/aip/jap/article-pdf/doi/10.1063/5.0064723/13254302/124503\_1\_online.pdf`. URL: `https://doi.org/10.1063/5.0064723`.
L.M. Modified the data acquisition software to suite the experimental requirements, performed quality control on the data acquired, and participated in the writing of the manuscript.

[3] Albert Wandui, James J. Bock, Clifford Frez, et al. "Thermal Kinetic Inductance Detectors for Millimeter-wave Detection". In: *Journal of Applied Physics* 128.4 (July 2020), p. 044508. ISSN: 0021-8979. DOI: `10.1063/5.0002413`. eprint: `https://pubs.aip.org/aip/jap/article-pdf/doi/10.1063/5.0002413/15252752/044508\_1\_online.pdf`. URL: `https://doi.org/10.1063/5.0002413`.
L.M. Instrumented the test cryostat, designed the readout electronics, contributed to the development of the software base for the data analysis, leaded the data acquisition and contributed to the writing of the manuscript.

[4] Lorenzo Minutolo, Bryan Steinbach, Albert Wandui, et al. "A Flexible Gpu-accelerated Radio-frequency Readout for Superconducting Detectors". In: *IEEE Transactions on Applied Superconductivity* 29.5 (2019), pp. 1–5. DOI: `10.1109/tasc.2019.2912027`.
L.M. contributed to the base concept of the research, chose the hardware, wrote the software, tested the final instrument, and leaded the writing of the manuscript. L.M. mintained the software for years. 2019-defense date, and adapted in to the requirements of a diverse panorama of experiments.

TABLE OF CONTENTS

Chapter 1

INTRODUCTION

1.1 Motivation

Modern inflationary cosmology has revolutionized the way we think about our Universe, involving new physics including dark matter, dark energy, and inflation. Our conception has been strongly driven by experiment, most notably precise measurements of the CMB and large scale structure. Inflationary expansion in the very early Universe may have generated a gravitational wave background. Such a background induces an odd-parity B-mode polarization pattern at degree angular scales. Precision polarized maps of the sky at millimeter wavelengths can be used to constrain the amplitude of the gravitational wave background, and thus the energy scale of inflation [1]. This energy could be as high as 10^{16} GeV, which may be associated with Grand Unification Theories, probing physics at energies beyond the reach of terrestrial particle accelerators.

Present-day CMB experiments require nK-deg map depth. Current detectors are limited by photon noise, even in the low photon environment of space and utilize large imaging arrays to achieve those depths. These experiments also control for galactic foregrounds by mapping at several frequencies. Future experiments in space plan 13,000 detectors [2] and CMB-S4 plans 500,000 detectors [3].

For the past 15 years, most suborbital CMB experiments have used TES (Transition Edge Sensor) bolometer arrays [4], read through SQUID (Superconducting Quantum Interference Device) multiplexers. Each detector must be wirebonded to its readout SQUID, a serial by-hand task that does not scale well to large formats. SQUIDs have low multiplexing factors that require large wire counts for row addressing and bias, further restricting array formats. SQUIDs also require extreme magnetic shielding. To mitigate the risk associated with many complex steps in SQUID assemblies, and reduce the cost and complexity of the electronics, our team has developed Thermal Kinetic Inductance Detectors (TKIDs), where the TESes in the bolometers are replaced by a thermally sensitive superconducting inductor within a high-Q resonant circuit. Like traditional KIDS, this allows passive RF multiplexing by designing each detector with a unique resonant frequency. Since the detectors' signals combine by coupling to a common RF feedline, all defined lithographically, they obviate the arduous wirebonding required by TES/SQUID integration. Unlike traditional KID designs, the antenna and absorber are electrically decoupled from the resonator, allowing independent optimization of both elements, which allows us to suppress the excess noise mechanisms (for example: two-level system noise and recombination noise) that plague the 1/f noise performance of photon-coupled KID architectures. Through such fine tuning, TKIDs realize background limited noise at low frequencies. Next generation CMB experiments require ~ 100,000 detectors with stable noise performance, so a working demonstration of a highly multiplexed stable TKID array would have breakthrough scientific implications.

The goal of the project documented in this thesis is to deliver a demonstrator camera compatible with the BICEP infrastructure and with performances that match the, already deployed, 150GHz TES detectors [5]. The deployment of such receiver in the BICEP Array mount could improve the TRL (Technology Readiness Level), detailed in Figure 1.1, of the technology up to “deployed in relevant environment“ TRL 5/6. This works document the steps followed from the very first chips (TRL 2) to validate the camera in a laboratory environment (TRL 4) and delivers a deployable instrument, laying the foundations for TRL 6.

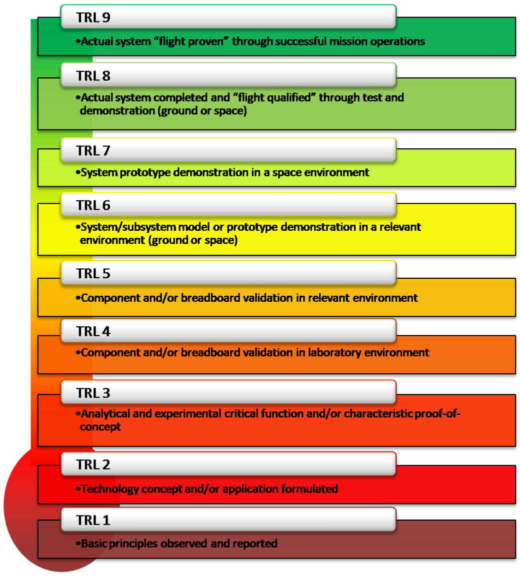

Figure 1.1: NASA TRL (Technology Readiness Level) diagram. Deployment of a TKID camera would raise the status of the technology to TRL 6, the scope of this work is to start from TRL 2, demonstrate TRL 4 and preparing the instrument for TRL 6 (demonstration in relevant environment).

As it is documented in the next section, the BICEP Array experiment represent an excellent framework to test new detector technology. A few key reasons are:

- The intrinsic modularity of a multi-wavelength observatory presents the opportunity of swapping a single receiver tube without impacting the rest of the experiment.

- The detector architecture used in the focal plane makes possible to reuse the antenna design and swap the thermometric element for a direct technology comparison.
- The unique location at the South Pole represent a good approximation of space's harsh environmental condition and logistic.

1.2 BICEP Array, scientific goal, and results

BICEP Array, as its predecessors BICEP 1 (2006), BICEP 2 (2011), Keck Array (2012-2017) BICEP 3 (2015), is an experiment focused singularly on determining the degree scale B-mode polarization of the Cosmic Microwave Background generated by primordial gravitation waves. In order to describe the technological requirements to perform such a measure, let us briefly describe the theoretical framework.

ΛCDM model

The inflation theory is build on the concept of an expanding universe. The standard model of cosmology or ΛCDM model is a model that provides a comprehensive framework for understanding the large-scale structure, dynamics, and evolution of the universe. At its core, the model is built upon a Cosmological Constant (Λ) driving the accelerated expansion of the universe and the presence of Cold Dark Matter. Although there are critics [6], the ΛCDM robustly predicts key observations [7] , including CMB anisotropies, and it is the most commonly accepted model for explaining cosmological history.

The equations that underpin the ΛCDM (Lambda Cold Dark Matter) model are formulated based on a fundamental observation regarding the distribution of matter and energy density in the universe. This observation reveals that on large scales, the universe exhibits a property known as homogeneity and isotropy. Homogeneity implies that the universe appears the same at every point in space, while isotropy suggests that it looks the same in all directions when observed from any given point. These two principles collectively imply that there are no preferred locations or orientations in the universe when considered on cosmological scales. Mathematically, the description of an isotropic and homogeneous universe is the Friedmann-Robinson-Walker Metric [8]:

$$\begin{aligned} ds^2 = -dt^2 + a(t)^2 \left[\frac{dr^2}{1-kr^2} + r^2(d\theta^2 + \sin^2\theta \, d\phi^2) \right] = \\ -dt^2 + a(t)^2 \left[\frac{dr^2}{1-kr^2} + r^2 d\Omega^2 \right] \end{aligned} \tag{1.1}$$

where ds^2 is the spacetime interval, dt is the differential time element, dr is the differential radial distance element, $d\theta$ is the differential polar angle element, and $d\phi$ is the differential azimuthal angle element. We wrap the last two into a solid angle differential $d\Omega$. The scale factor $a(t)$ represents the expansion of the universe with time, and k is the curvature parameter representing the spatial curvature of the universe. Where K=k is a parameter describing the curvature of the universe and can have values in the interval [-1:1]. Where $k = \pm 1$ describe a convex/concave universe, $k = 0$ a flat one (as measured using the CMB [9]). Since the expansion rate of the Universe $a(t)$ is changing over time it is useful to work in conformal time, τ:

$$d\tau = \int \frac{dt}{a(t)}.$$

Substituting in equation 1.1 we get:

$$ds^2 = a(t)^2 \left[d\tau^2 - \frac{dr^2}{1 - kr^2} + r^2 d\Omega^2 \right]. \tag{1.2}$$

We can now calculate the geometry of spacetime, and thus the universe dynamic, by defining the metric tensor, $g_{\mu\nu}$, as $ds^2 = g_{\mu\nu}\dot{d}X^{\mu}dX^{\nu}$. For the FRW metric we get:

$$g_{\mu\nu} = \begin{pmatrix} -1 & 0 & 0 & 0 \\ 0 & a(t)^2/(1 - kr^2) & 0 & 0 \\ 0 & 0 & a(t)^2 r^2 & 0 \\ 0 & 0 & 0 & a(t)^2\Omega^2 \end{pmatrix} \tag{1.3}$$

and plugging the tensor in the Einstein field equation:

$$G_{\mu\nu} = R_{\mu\nu} - \frac{1}{2} g_{\mu\nu} R = \frac{8\pi G}{c^4} T_{\mu\nu} \tag{1.4}$$

where $G_{\mu\nu}$ is the Einstein tensor, R and $R_{\mu\nu}$ are the Ricci tensor and scalar, respectively, $g_{\mu\nu}$ is the metric tensor calculated in 1.3 $T_{\mu\nu}$ is the stress-energy tensor representing the distribution of matter and energy, G is the gravitational constant, and c is the speed of light in vacuum. So for a co-moving observer the time-time component and the radial space-space component will be:

$$T_{00} = \rho c^2 \qquad T_{rr} = \frac{pa^2}{1 - kr^2} \tag{1.5}$$

where p and ρ are mass pressure and density. Knowing from equation 1.4 that $G_{\mu\nu}$ equate to $T_{\mu\nu}$ it can be calculated that:

$$G_{00} = 3(ca)^{-2}\left(\dot{a}^2 + kc^2\right) \qquad G_{rr} = -c^2(2a\ddot{a} + \dot{a}^2 + k)(1 - kr^2)^{-1} \tag{1.6}$$

and by plugging 1.5 and 1.6 into the Einstein field equation 1.4, we get the two dynamical relations for the time evolution of the cosmic scale factor $a(t)$:

$$\left(\frac{\dot{a}}{a}\right)^2 + \frac{kc^2}{a^2} = \frac{8\pi}{3}G\rho \tag{1.7}$$

and

$$2\frac{\ddot{a}}{a} + \left(\frac{\dot{a}}{a}\right)^2 + \frac{kc^2}{a^2} = \frac{8\pi}{c}Gp. \tag{1.8}$$

Combining energy conservation, that in Einstein's notation is $\nabla_\mu T^\mu_0 = 0$, to equations 1.7 and 1.8 we get:

$$\dot{\rho} = -3\frac{\dot{a}}{a}(p + \rho) \qquad \frac{\ddot{a}}{a} = -\frac{4\pi}{3}(\rho + 3p). \tag{1.9}$$

If now we contemplate an equation of state of the form $p = \omega\rho$ relating mass pressure and density, we can use equations 1.9 to find the solution:

$$\rho = \rho_0 a^{-3(\omega+1)}. \tag{1.10}$$

At this point we have to differentiate between the different components of the universe because of the different way they contribute to density and pressure.

- Radiation: consists primarily of photons (e.g., cosmic microwave background radiation) and relativistic particles. Due to their high kinetic energy, relativistic particles contribute differently to the energy density and pressure compared to non-relativistic matter. The equation of state for radiation is characterized by $p = \frac{1}{3}\rho c^2$, where p is the pressure, ρ is the energy density, and c is the speed of light in vacuum. The density parameter for radiation, denoted as Ω_{rad}, quantifies the fraction of the critical density contributed by radiation in the universe.

- Matter: Matter in the universe consists of non-relativistic particles such as baryonic matter (e.g., protons and neutrons) and dark matter. These particles have relatively low velocities compared to the speed of light. For non-relativistic matter, the equation of state is approximately $p \approx 0$, meaning that its pressure is negligible compared to its energy density. The density parameter for matter, denoted as Ω_{m}, represents the fraction of the critical density contributed by matter in the universe.

- Cosmological constant: often associated with dark energy, the cosmological constant represents a constant energy density filling space homogeneously. It is often parameterized by Λ and corresponds to a negative pressure component that drives the accelerated expansion of the universe. For the cosmological constant, the equation of state is characterized by $p = -\rho c^2$. The density parameter for dark energy, denoted as Ω_Λ, quantifies the fraction of the critical density contributed by the cosmological constant.

In order to use the concepts hereby introduced, and go back to the origin of the universe, we need to know the current proportion of matter, energy and dark energy. The data from the Plank collaboration [10] comes to our rescue: $\sim$ 70% dark energy and $\sim$ 30% matter (dark + baryon); radiation is negligible. Having this information, we can calculate the expansion rate when the Universe went through the epochs of radiation domination, matter domination, or as currently, dark energy dominated period. It is customary to define the Hubble parameter:

$$H(t) = \frac{da/dt}{a} = \frac{\dot{a}(t)}{a(t)}. \tag{1.11}$$

If we impose a flat universe, $k = 0$, in equation 1.9, we get a critical density:

$$\rho_c = \frac{3H^2}{8G\pi} \tag{1.12}$$

and, consequently a total density:

$$\Omega_t = \frac{\rho}{\rho_c}.$$

Let us now express the density of each component of the universe as a ration with its specific critical density and rewrite the first Friedman equation 1.7 using the Hubble parameter in 1.11. What we get is:

$$H^2 = H_0^2 \left[\Omega_{0,\mathrm{matter}} \cdot a^3 + \Omega_{0,\mathrm{radiation}} \cdot a^4 + \Omega_{0,\mathrm{curvature}} \cdot a^2 + \Omega_{0,\Lambda}\right] \tag{1.13}$$

Where Ω_0 refers to current conditions and we reintroduced k just to mention that we can envision universes with a density $\Omega_k \neq 1$ and a non-flat curvature. Regardless of the geometry determining the future cosmic evolution, the ΛCDM model envisions an expansion phase. Hubble's 1929 observations [11] revealed the expanding nature of the universe and allowed the scientific community to hypothesize about its hot, dense origin: the Big Bang. In an expanding universe the average temperature scales as:

$$T = T_0 a^{-1} \tag{1.14}$$

Where a is the scale factor from 1.13 and T_0 is the current temperature, $T_0 = 2.72548 \pm 0.00057K$ [12]. At the same time the photon's wavelength reduces with:

$$\nu \propto a^{-1} \tag{1.15}$$

Equations 1.14 and 1.15 tell us that as we go back in time, getting smaller and smaller a, the temperature increases as well as the energy of the particles involved. The main processes that governed particles interaction in the early universe were: Bremsstrahlung, Compton and double Compton scattering. For Hydrogen atoms to form, we have to wait for the universe to expand enough to cool down the plasma and let the reaction $e^- + p^+ \longrightarrow H + \gamma$ become prevalent. Assuming the equilibrium of ionized particles, we can use the Saha equation to describe the free electron fraction as:

$$\frac{X_e^2}{1 - X_e} = \frac{1}{n_e + n_h}\left[\left(\frac{m_e T}{2\pi}\right) e^{-\epsilon_0/T}\right] \tag{1.16}$$

where $\epsilon_0 = 13.6eV$. The equation above shows that the universe remained ionized $X_e \sim 1$ until $T << \epsilon_0$. The Recombination happened approximately 300k years after the big band, when the temperature of the universe was $\sim 300K, 0.3eV$. The quick photon decoupling, i.e., the universe becoming transparent, impressed in the now propagating photons the properties on the surface on which they last scattered, the so called last scattering surface. With the expansion of the universe the wavelength of the photons carrying this information got stretched in the microwave band, what we currently call CMB. The Cosmic Microwave Background, discovered by accident in 1965 by Arno Penzias and Robert Wilson [13] as a 3.5K isotropic radiation. The first measurement of the CMB frequency spectrum was performed by the COBE FIRAS instrument and agreed nicely with a blackbody spectrum of temperature $2.72548 \pm 0.00057K$ [12]

CMB polarization

Photons originated from the last scattering surface encode information about early stages of the universe expansion. Specifically the spectrum of CMB temperature anisotropies (deviation from a blackbody distribution) has peaks encoding information about the acoustic oscillations happening at recombination time due to overdense regions in the plasma balancing with radiation pressure. If we consider the quadrupole component of the radiation field, just before recombination, undergoing Thompson scattering, as illustrated in Figure 1.2 we obtain that the acoustic peak in the CMB anisotropy is polarized.

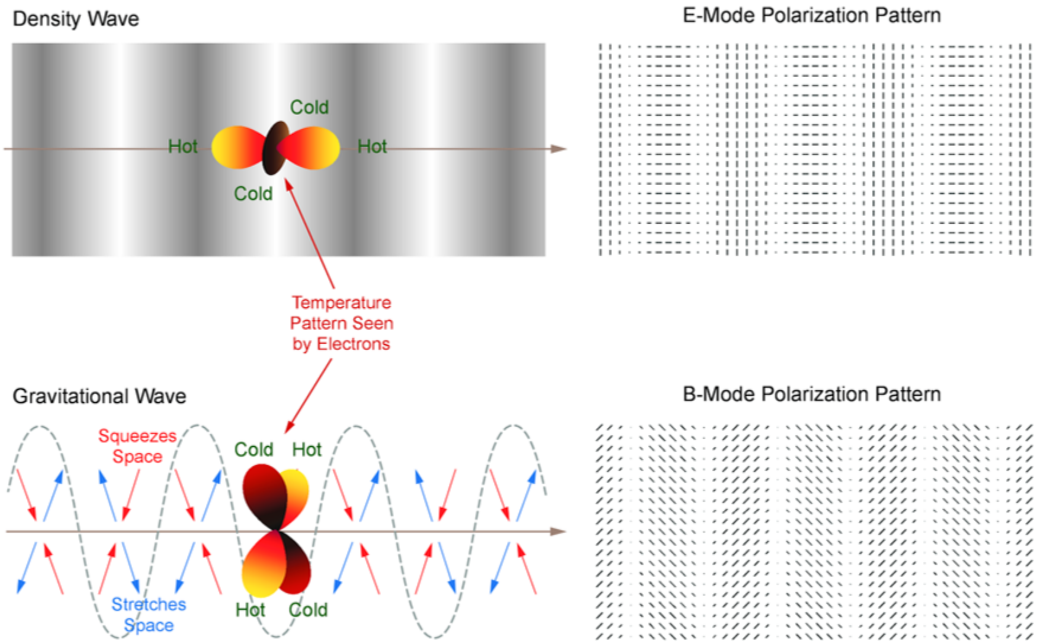

Figure 1.2: Figure taken from [14] illustrating Thompson scattering in the presence of a quadrupole field. In the figure's top portion, the black and white pattern represents the plasma's acoustic oscillation, and the jet-scale volume represents the temperature pattern the electrons see. For an acoustic wave, the polarization produced by the scattering of the quadrupole component of the radiation field results in perpendicular or parallel polarized radiation with respect to the propagation direction. In the bottom part of the figure, the jet-scale volume represents the temperature pattern seen by electrons when affected by a gravitational wave. The quadrupole Thompson scattering results in radiation polarized at 45^o with respect to the propagation direction.

The polarization anisotropies can be written as:

$$(Q + iU) \cdot \hat{n} = \sum_{l,m} a_{l,m} Y^{\pm 2}_{l,m} \hat{n} \tag{1.17}$$

where Q and iU are the vertical and horizontal component of the pattern, $Y^{\pm 2}_{l,m}$ are spin-2 or tensor-spherical harmonics and $a_{l,m}$ is a coefficient describing the intensity of the specific component. This is quite problematic to discuss as we cannot practically plot the spectrum of a spin-2 tensor. What is customary is to define two scalar spin-0 fields, $E(l)$ and $B(l)$ so that the $E(l)$ component describe the intensity of orthogonally polarized pattern and the $B(l)$ the intensity of polarization vectors with vorticity around any point. The full mathematical procedure is thoroughly explained in [15]. Because the polarization E and B and the temperature T are spin-0 fields, we can write the autospectra, considering the universe isotropic, as:

$$C_l^{XX} = \frac{1}{2l+1} \sum_m < a_{lm}^* a_{lm} > \qquad X = [T, B, E] \tag{1.18}$$

The ΛCDM model gives predictions for each [16], reported in Figure 1.3. As [17] and [18] demonstrate, scalar perturbations, lie the acoustic plasma oscillations, can generate T and E anisotropies in the CMB, but not B. Tensor perturbation can generate all modes. The fact that B-mode polarization can only be generated by tensor perturbations makes it a unique tool for studying gravitational waves before the recombination time.

Inflation

The leading theory explaining the presence of gravitational waves before the recombination time is the inflationary theory. Inflation refers to the period of time from the Big bang to 10^{-32} seconds. Inflationary theory explains the presence of large scale structures in the current universe with the fluctuation of a quantum field in the microscopic inflationary region. This region quickly expands to bigger proportions shifting the fluctuations out of causal range and planting the seeds for the growth of structure in the Universe.

The inflationary theory solves a list of problems that were found in the Big Bang theory [19]. The Universe's current appearance suggests it began with extremely precise initial conditions at the Big Bang. Inflation seeks to address this by introducing a dynamic process that guides the Universe toward this particular state. Consequently, within the framework of the Big Bang theory, a universe resembling ours becomes considerably more probable. A short description of these problems follows:

- **Horizon problem**: The horizon problem addresses the challenge of understanding the uniformity and isotropy of the universe as dictated by the cosmological principle. In the context of the Big Bang theory and the components described in the Standard Model, distant regions of the observable universe have never interacted causally due to their rapid separation surpassing the

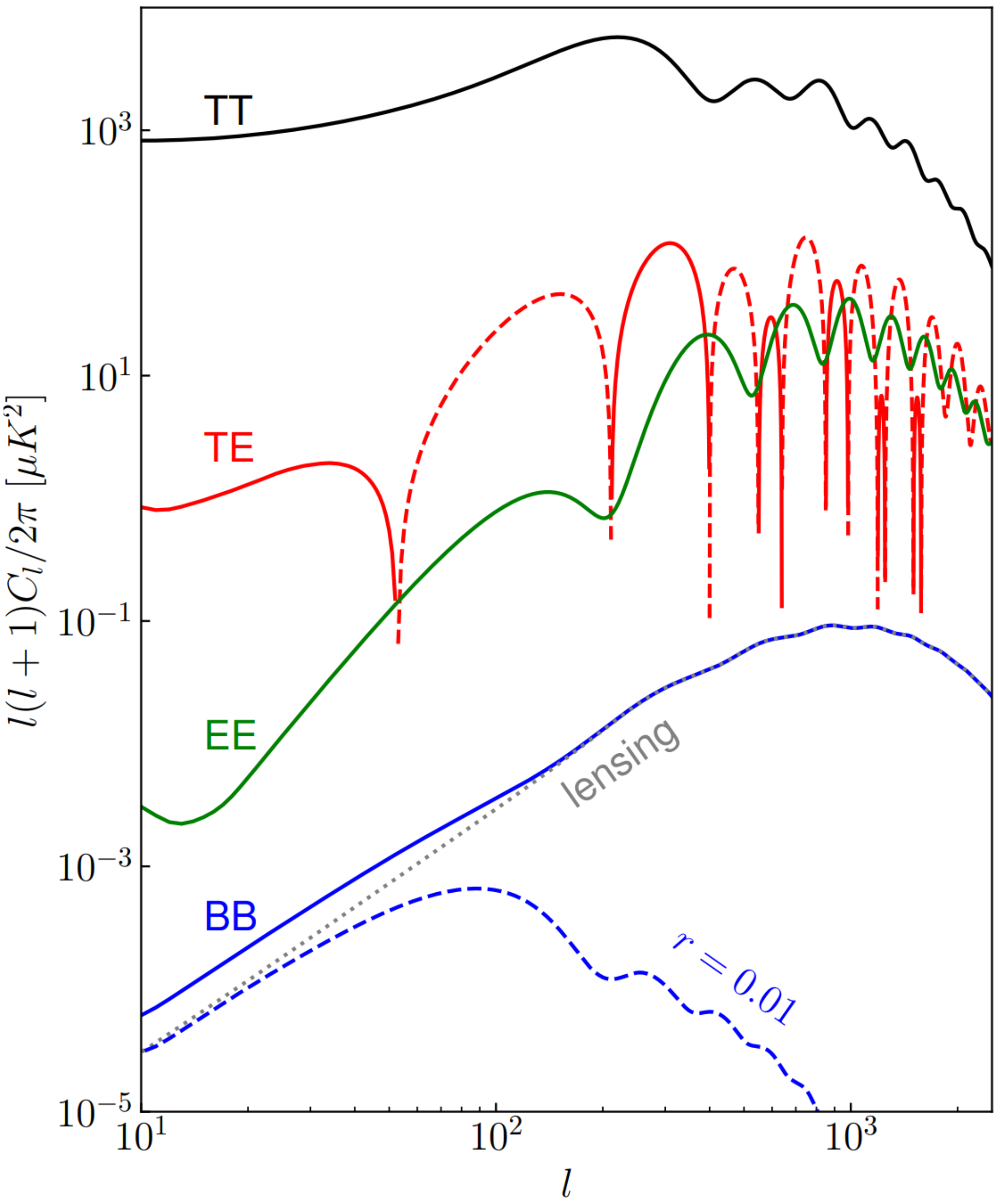

Figure 1.3: Figure taken from [16] illustrating the prediction for the autospectra of temperature and E,B polarization patterns according to the ΛCDM model. On the Y axis there is the scaled intensity coefficient and on the X axis there is the scale of the fluctuation expressed in modes, the index of the spherical harmonics. The dash blue line shows the expected unlensed B mode autospectrum assuming $r = 0.01$.

speed of light. Consequently, there is a lack of explanation for the thermal equilibrium between these regions.

- **Flatness problem**: It became known in the 1960s that the density of matter in the Universe was comparable to the critical density necessary for a flat universe, see equation 1.12. Hence, irrespective of the universe's geometry, the influence of spatial curvature on its expansion should not surpass that of matter significantly. However, with the universe's expansion, curvature diminishes slower than matter and radiation. Tracing back in time poses a fine-tuning challenge since the curvature's contribution must be exponentially small.

- **Magnetic-monopole problem**: Despite extensive searches and theoretical expectations, no evidence for the existence of these magnetic monopoles has been found. The absence of magnetic monopoles is particularly problematic because their existence could help explain various cosmological puzzles, such as the origin of galactic magnetic fields and certain aspects of the early universe's evolution. Inflation would justify the absence of magnetic monopoles by envisioning their presence instantly after the Big Bang and their dilution thanks to the rapid expansion of the universe.

During the exponential expansion, the inflation field's quantum fluctuations stretch out and subsequently serve as the foundation for the formation of large-scale structures. In the most basic scenario, a solitary scalar field ϕ can propel the inflation process. if we have a single field in the spacetime:

$$\phi(t,\vec{x}) = \hat{\phi}(t) + \delta\phi(t,\vec{x}). \tag{1.19}$$

We can calculate the perturbation in the metric tensor:

$$g_{\mu,\nu}(t,\vec{x}) = \hat{g}_{\mu,\nu}(t) + \delta g_{\mu,\nu}(t,\vec{x}) \tag{1.20}$$

And express it in scalar,vector and tensor components by defining the following:

$$g_{0,0} \equiv -(1+2\vec{\Psi}) \tag{1.21}$$

$$g_{0,i} = 0 \tag{1.22}$$

$$g_{i,j} \equiv a^2\delta_{i,j}(1+2\Phi). \tag{1.23}$$

We define the inflation field with no vector component, equation 1.22, because even if there was one, it would decay when the universe expands [20]. The perturbated metric results in:

$$g_{i,j} = \begin{bmatrix} 1+h_+ & h_\times & 0 \\ h_\times & 1-h_+ & 0 \\ 0 & 0 & 1 \end{bmatrix} \tag{1.24}$$

where h_+ is the scalar component and $h_\times$ is the tensor one. The linear approximation of the metric perturbation allows each mode to evolve independently in Fourier space, furthermore, we can label the modes using their wave number $k = \vec{K}$. Because the universe is rapidly expanding but the comoving wavelength is not, we say that a mode is out of the horizon when:

$$k < aH \tag{1.25}$$

where a is the universe' expansion rate and H is the Hubble constant. From an overdensity spot point of view, when a mode exits the horizon, the potential it casts remain frozen and starts to evolve again as soon as it reenters. As the modes with the same wavelength enter the horizon simultaneously, they naturally have a phase alignment. The coherence of the perturbation mode is a prediction of the inflation that explains the peaked spectrum of the CMB anisotropies [21]. At the end of the day, the metric in equation 1.24 produces an energy distribution that we are going to parametrize by observing the variance of the power spectrum at horizon crossing (when it freezes). The parametrization will have the scale index of the power law distribution n_s, the vector and scalar component expressed as a ratio $r = \Delta_s/\Delta t$, proportional to the energy scale of the inflation field. While the power law index n_s has been very well constrained, $= 0.9649 \pm 0.0042$ (95% CL) [22], the lower limit to the tensor-to-scalar ratio r has not yet been constrained. A constrain on r reflects directly in the exclusion of possible models for the inflation field, results at the time of writing, summarized in Figure 1.4 are of $r < 0.035$ [23]

1.3 Measuring r: BICEP Array

Looking at Figure 1.3, we can see that the B-mode spectrum is not exclusively a result of the tensor components of the inflation field. The B-mode spectrum we expect to see has different phenomena that mask the inflation generated spectrum. In Figure 1.3 the only one reported is the gravitational lensing but other foregrounds are also present. As we can observe in Figure 1.5, taken from the BK18 paper [23]

- **Gravitational lensing**: a phenomenon predicted by Einstein's theory of general relativity, occurs when the gravitational field of a massive object, such as a galaxy or a galaxy cluster, bends the path of light passing nearby. This bending effect distorts the appearance of background objects, causing them to appear magnified, stretched, or even duplicated. In the context of the Cosmic Microwave Background (CMB), gravitational lensing alters the paths of

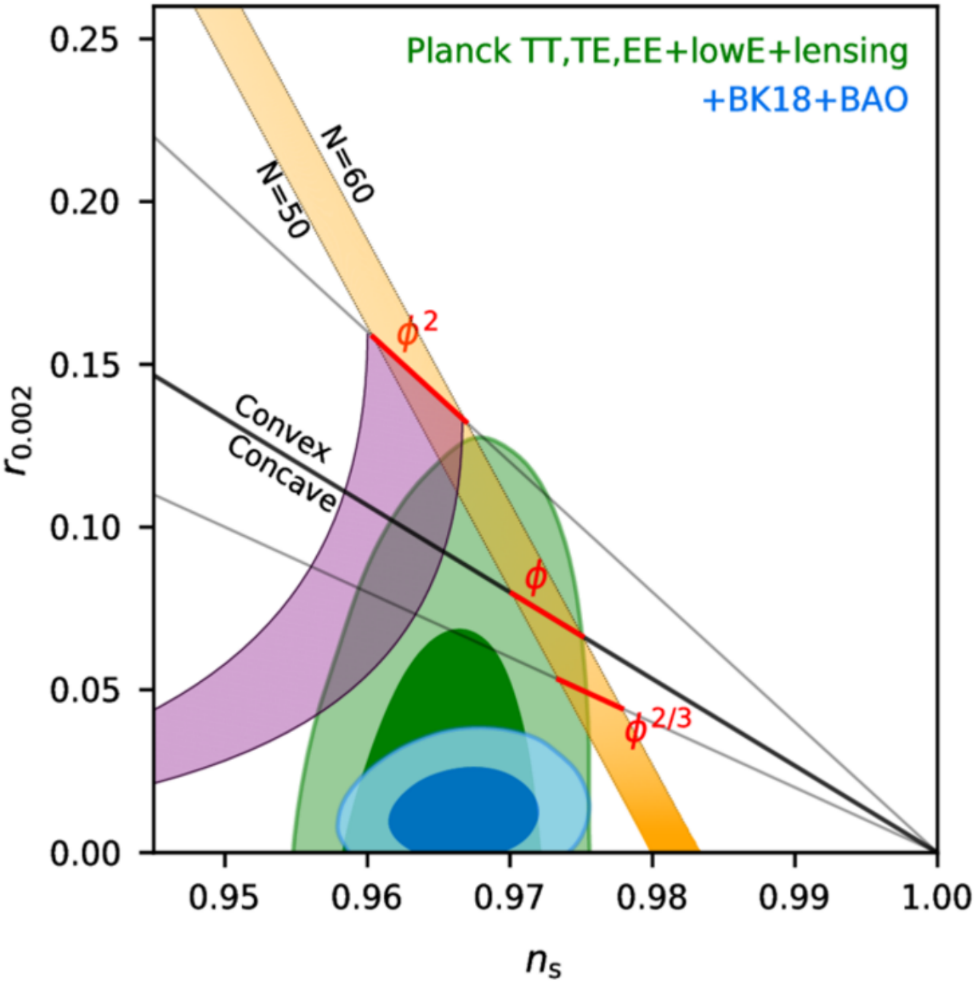

Figure 1.4: Constraints in the r , n_s space for different inflation fields from [23]. New limits on r exclude most of the multi-field models for cosmic inflation. Some single-field models with polynomial potentials are plotted as black lines with 50 and 60 e-fold boundaries marked out. The purple band represent a natural inflation [24].

CMB photons as they travel through the large-scale structure of the universe, leading to a distortion in the observed polarization patterns [25]. Specifically, gravitational lensing mixes the E-mode and B-mode polarization of the CMB because the lensing process converts some of the primordial E-mode polarization into B-mode polarization. This mixing occurs due to the asymmetric nature of gravitational lensing, where the deflection of light rays by intervening mass distributions induces a curl component in the polarization field, generating B-mode polarization from the original E-mode polarization.

- **Thermal Dust Radiation**: interstellar dust grain heat up by absorbing lights emitted from stars and cool down by emitting highly polarized radiation [26]

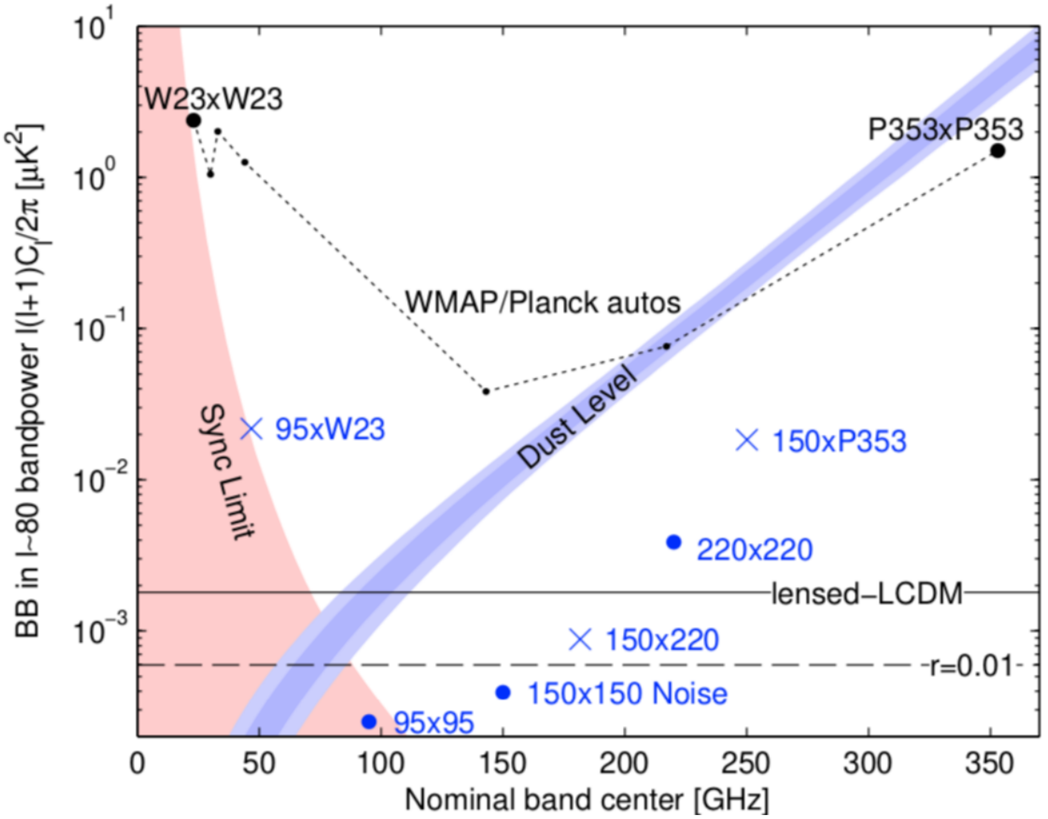

Figure 1.5: Another plot from [23]. This plot shows the B-mode spectrum expectation values and noise uncertainties, for the mode $l \sim 80$ in the observed patch of sky for BK. The color bands are the 95% synchrotron upper limit (red) and the 1 and 2 σ constraint on dust (blue). The black horizontal dashed line is the expected bandpower for the primordial BB assuming $r = 0.01$ dots and crosses are the noise uncertainties for auto and cross spectrum of BK data while black dots are the noise uncertainties of external data involved in the analysis.

according to a modified blackbody spectrum [27] around 20K, mostly in far-infrared and sub-millimeter. Dust radiation dominates the higher frequency band of CMB observation. Polarization measurements are deeply affected as the asymmetric distribution and shape of dust clouds interacts with the galactic magnetic field and results in the polarization fraction of dust emission to be $\sim 20\%$ [28].

- **Syncrotron Radiation**: the interaction between the galactic magnetic field and relativistic particles results in the particle gyrating and emitting highly polarized radiation, where direction and intensity is up to the properties of the local magnetic field [29, 30]. The synchrotron radiation dominates frequency bands around 23GHz for multipole $l \sim 80$.

Separating the components of the foreground becomes an essential task for any hope of measuring r and characterizing the inflation field. Specifically if one has to use a multi-component, multi-spectrum likelihood analysis to constrain the tensor-to-scalar ratio, data in multiple frequency bands must be acquired.

BICEP Array is an experiment specifically designed for this task. Being the latest iteration of the Keck/BICEP collaboration series of telescopes [31], BICEP Array consists in four co-moving camera tubes scanning a patch of sky at 6 different frequencies. The four tubes are designed so that the distribution of frequencies is 30/40 GHz dual polarization, 95GHz, 150GHz and 220/270 dual polarization. The novelty of this experiment consists in the number of detector deployed [32]. Increasing the number of detectors allows for a faster sky signal integration and thus, for a better constraint on the upper limit of r in less time.

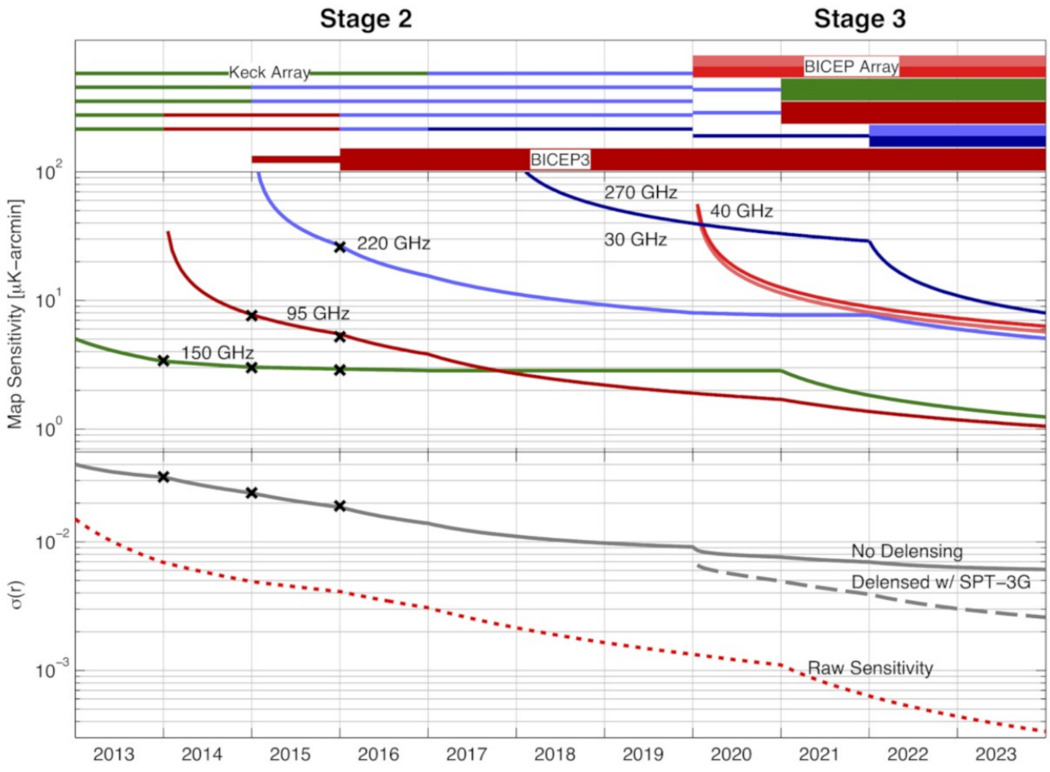

Figure 1.6: Constraint on $\sigma(r)$ in function of time (and effort), taken from [32]. The top part is the frequency distribution over the various receivers deployed by the BICEP/Keck collaboration. The middle part describes the evolution of the map depths at each frequency. The bottom part is the sensitivity on r, the tensor-to-scalar ratio, after accounting for foreground and distortion effects. In dashed red line represent the theoretical sensitivity in absence of foreground.

In a photon noise limited scenario, increasing the number of detectors on sky is the only way to speed up the constraining of r. The TESs (Transition Edge Sensors) [33] developed for the experiment are designed to have an internal noise lower than the statistical noise of the photons they are trying to measure. Each frequency band has its own requirement [34] since the photons incoming from the sky have different physical origins. Scaling the number of cryogenic detectors to the $\sim$ 100.000 proves to be a significant challenge. Classic TESs readout schemes require the implementation of complex cryogenic electronics [5] and a staggering number of fragile boar to waver connection (wirebonds). The necessity of scaling superconductive bolometric detectors is not unique to the BICEP collaboration but rather a necessity of the whole scientific field [35, 36]. The importance of testing novel way to pack more superconductive detectors together is underlined also in the 2020s NASA decadal [37]

1.4 Desired camera performances

The purpose of the previous sections was to introduce the technological motivation and the scientific framework that encompass the development of a TKIDs camera. In short: important scientific goals, like the measure of r, require instruments with a number of detectors that stretches the current technology's scalability; The BICEP Array experiments provides a well structured framework, precise requirements and the possibility to directly compare different technologies. Furthermore, the deployment of a new technology at the BICEP Array site would greatly enhance its TRL (Technology Readiness Level), see Figure 1.1.

Number of detectors

The number of detectors that we intend to deploy in the camera is dictated by the infrastructure compatibility requirements and the trade-off between demonstrating the scalability of the technology and delivering a test instrument in a reasonable time frame. The BICEP Array telescope mount [38] supports two different types of receives, shown in Figure 1.7: a 550mm aperture one and a smaller 250mm aperture (Keck-style). We chose to implement our camera in the Keck-style receiver for two fundamental reasons. First, smaller mechanical parts made the R&D process more streamlined and the logistic simpler. Secondly, the logistics of implementing a 550mm receiver would have significantly impacted the delivery time of the instrument; specifically, because this is a demonstration camera, populating the full focal plane of a large aperture receiver would not have added value to the test. Once the receiver style is set, the dimension of the focal plane unit (FPU) is inherited from legacy designs. The micro-fabrication process compatible with the FPU dimensions is what we call the 4in tile. 4 in tiles are square silicon tiles with a diagonal of 4in on which the structure of our detectors is lithographed and deposited. The FPU of a Keck-style receiver can accommodate four 4in tiles in total. The purpose of developing the TKID camera is to compare frequency multiplexed and time-domain multiplexed detectors as the thermometric element of a polarization sensitive pixel: we want the same slot antenna design used for the 150GHz TES counterpart [39] as the optical radiation absorber. The constraints given on the tile size and the pixel size lead to a very small margin of choice: each tile will have a 8×8 matrix of dual polarization pixels for a total of 128 detectors per tile. A detailed description of the tile design and fabrication process is available at [40, 41]

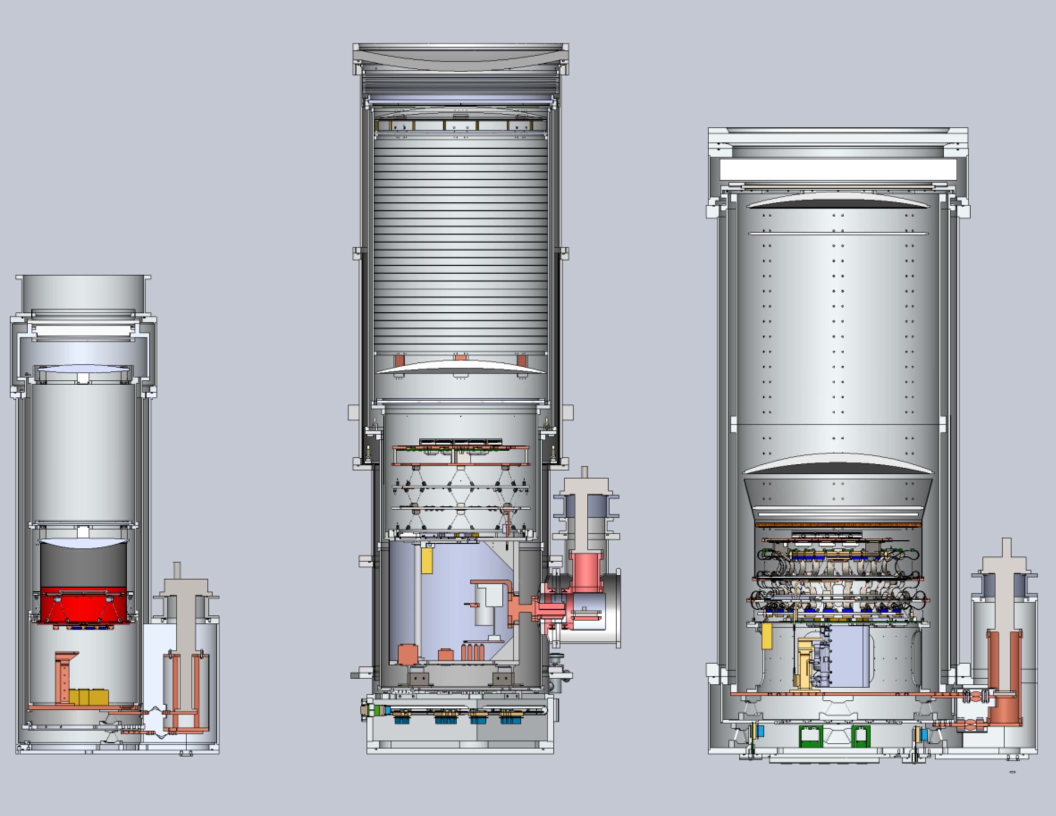

Figure 1.7: Figure taken from [38] showing a cross section of different telescopes deployed by the BICEP/Keck collaboration during the years. The BICEP Array mount supports the deployment of the Keck style, 250mm aperture tube (leftmost) and BA style 550mm aperture (rightmost). The Keck style cryogenic receiver has been chosen for for the development of a TKIDs test camera because of its faster turn around time and easier logistic due to smaller mechanical parts.

Noise performance

The noise and bandwidth requirements for TKIDs must match or be better than the TESs counterpart. The choice of the optical frequency, 150GHZ, determines the incoming photon noise while the bandwidth requirements comes directly from the scanning strategy. For the degree-scale observation performed by BICEP2 at 150GHz, the optical load from the atmosphere, through the optical filter stack, is P_{opt} =4.9pW [42]; the telescope data acquisition rate is 200Hz and the noise performance required to be phonon noise limited can be calculated considering a single mode detector for which the bandwidth $\Delta\nu << \nu$ as:

$$NEP_{\gamma}^{2} = 2h\nu_{opt}P_{opt} + 2\frac{P_{opt}^{2}}{\Delta\nu_{opt}} \tag{1.26}$$

where ν_{opt} is the frequency of incoming photons, 150 GHz in our case, $\Delta\nu_{opt}$ is the detector bandwidth ($0.25\nu_{opt}$) and P_{opt} is the optical power incident on the detector. The resulting photon noise is $45aW/\sqrt{Hz}$ [43] Given the scanning strategy of BICEP Array [23], the bandwidth were to consider the $45aW/\sqrt{Hz}$ number is between 0.1 and 10 Hz.

Optical performance

With the exclusion of optical efficiency, the optical performance required for a functional demonstrator, are significantly lower than the science grade detector performance. The requirements drop comes from the data analysis step at which we want to benchmark the TKIDs technology. What are interested in demonstrating are mostly the noise performance and the compatibility of the fabrication process with the antenna patterning and deposition. The map making process [44] with data coming from TKIDs has no scientific relevance hence the B/E/T mode mixing introduced by the antenna far field and near field irregularities are not cast into technological requirements. Nevertheless, we need to demonstrate a good optical efficiency, a negligible direct stimulation of the thermometric element and the feasibility of fabricating dual polarization slot antennae alongside TKIDs.

Chapter 2

THERMAL KINETIC INDUCTANCE DETECTORS

Thermal Kinetic Inductance Detectors (TKIDs) combine the excellent noise performance of traditional bolometers with a radio frequency (RF) multiplexing architecture that enables the large detector counts needed for the next generation of millimeter-wave instruments. In this chapter, we will explain in detail the working principle of this detector technology and explore its development milestones.

2.1 Kinetic Inductance Detectors

An electric field applied near the surface of a superconductor causes the Cooper pairs to move. The pairs have a mass of $2m_e$ since energy is stored as kinetic energy. Because the magnetic field penetrates a short distance inside the superconductor, like in aluminum $\lambda = 50nm$, magnetic energy can be stored similarly to the electric one. The overall effect is that a superconductor has a surface inductance $L_s = \mu_0\lambda$ due to the reactive energy flow between the superconductor and the electromagnetic field. While the superconductor offers zero resistance to direct current, a resistive impedance R_s is measurable in the AC regime. Losses at signal frequency ω are caused by the small fraction of electrons that are not in Cooper pairs called "quasiparticles." The impedance of the superconductor is then: $Z_s = R_s + j\omega L_s$. If the working temperature $T << T_c$, were T_c is the transition temperature of the material, then $R_s << \omega L_s$ [45].

Photons and phonons with energy $h\nu > 2\Delta$ may break one or more Cooper pairs. The absorption of a high-energy photon creates N_{qp} quasiparticles which recombine into Cooper pairs on timescales τ_{qp} where $\tau_{qp} \sim 10^{-1}$ to 10^{-6} depending on the superconductor. The absorbed photons would then raise the quasiparticle density by δn_{qp} above its thermal equilibrium value. KIDs exploit the dependence of the surface impedance Z_s on the quasiparticle density: even if the changes in δZ_s are moderate, a resonant circuit built around the superconductor allows for the construction of a very sensitive detector. Changes in L_s and R_s affect the resonance by changing the phase and amplitude of the signal transmitted through the circuit.

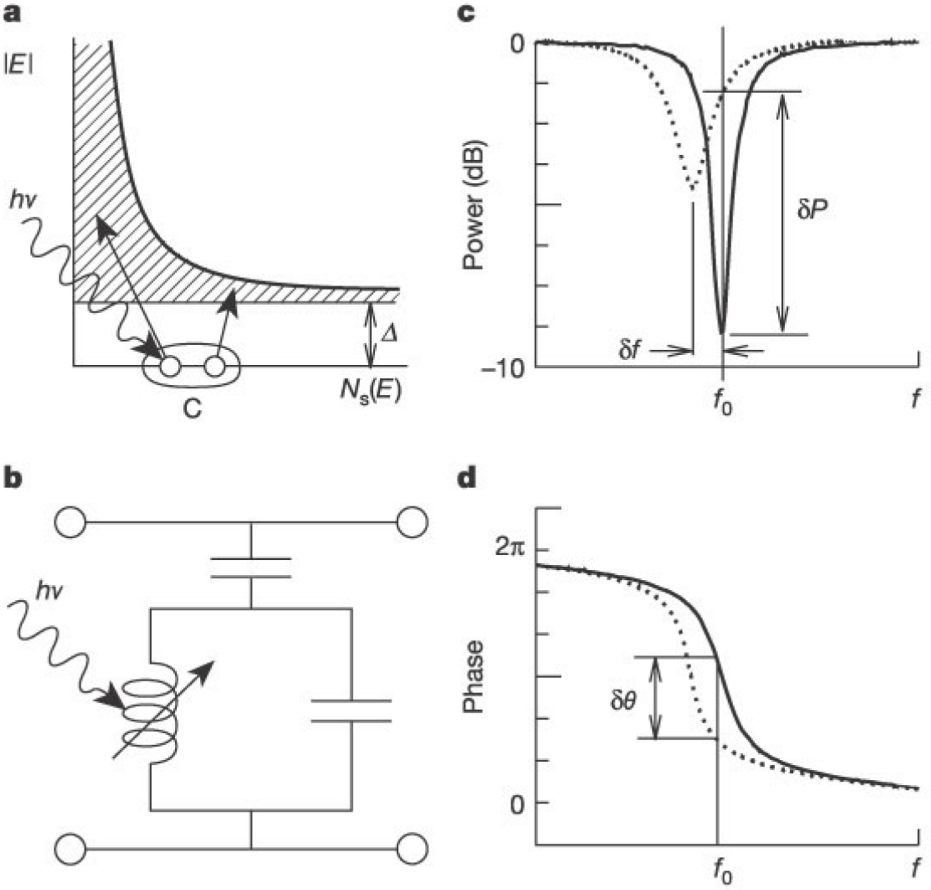

Figure 2.1: Classic diagram taken from [45] describing the working principles of Kinetic Inductance Detectors (KIDs). **(a)** Photons or phonons with energy $h\nu > 2\Delta$ are absorbed in a superconducting film cooled to $T << T_c$ and create a number of quasiparticles by breaking cooper pairs. In the diagram, Cooper pairs are shown at the Fermi level and the shaded area describes a qualitative representation of the quasiparticles' density of states $N_s(E)$ in function of energy E. **(b)** The increase in quasiparticle density changes the (mainly inductive) surface impedance, $Z_s = R_s + j\omega L_s$, of the film which is used as a part of a microwave resonant circuit. The diagram represent a capacitively coupled resonator. **(c)** and **(d)** are, respectively, the change in phase and amplitude of the circuit transfer function as seen from the transmission line

The electrical model for the circuit represented in Figure 2.1b is the series RLC circuit where the input impedance is:

$$Z_{in} = \left(R + \frac{1}{j\omega C} + j\omega L\right) \tag{2.1}$$

where R is the thin film DC resistance, ω is the probe signal frequency, L is the total inductance and C the total capacitance. Setting $\omega_0 = 1/\sqrt{LC}$ as the resonant frequency we get from 2.1:

$$Z_{in} = j\sqrt{\frac{L}{C}}\left(\frac{\omega}{\omega_0} - \frac{\omega_0}{\omega}\right) + R = j\sqrt{\frac{L}{C}}\left(\frac{\omega^2 - \omega_0^2}{\omega_0\omega}\right) + R. \tag{2.2}$$

For a small frequency deviation around ω_0, we can consider the transfer function to be:

$$Z_{in} = j\sqrt{\frac{L}{C}}\delta\omega/\omega_0 + R. \tag{2.3}$$

Now, defining the internal quality factor Q_i as the ratio of stored energy versus dissipated power, in a series RLC circuit one gets:

$$Q_i = \frac{2E_m}{W_{diss}(r)} \cdot \omega_0 = \frac{1/2 \cdot |I|^2 L}{1/2 \cdot |I|^2 R} \cdot \omega_0 = \cdot\omega_0 L/R = 1/(RC\omega_0) \tag{2.4}$$

So substituting Q_i in the expression for Z_{in} we get:

$$Z_{in} = R \cdot \left(1 + j\frac{2Q_i\delta\omega}{\omega_0}\right). \tag{2.5}$$

If we consider a perfect, symmetric transmission line with impedance Z_0 capacitively coupled with our RLC resonator we get that the scattering parameter between the input and output port S_{21} is:

$$S_{21} = \frac{Z_0}{Z_0 + Z_{in}/2}. \tag{2.6}$$

Rescaling Q_i with a total and coupling quality factor such as:

$$Q_r = \frac{1}{R + Z_{in}/2}\sqrt{\frac{L}{C}} \qquad Q_c = \frac{\sqrt{L/C}}{Z_{in}/2}, \tag{2.7}$$

we obtain the simplest form of KID transfer function:

$$S_{21} = 1 - \frac{Q_r/Q_c}{1 + j2Q_r x} \tag{2.8}$$

where $x = \delta\omega/\omega_0$. The transfer function in equation 2.8 does not reflect the wide range of resonator shapes encountered in our experiments, however it results in a really good approximation for reconstructing x from a complex S_{21} once the quality factors and the resonant frequency have been measured. Noticeably this functional form allows for multiple resonators to be coupled with the same transmission line with minimal interaction. A free spectral range in the order of a few Q_r^{-1} and different ω_0s enable multiple devices to detect signal without influencing each other local S_{21}. In other words: KIDs allows for a multiplexing scheme that can potentially reach the mega-pixel [46] scale without sacrificing the simplicity of having a single transmission line.

2.2 Thermal Kinetic Inductance Detectors

Thermal Kinetic Inductance Detectors (TKIDs) represent a distinctive adaptation of Kinetic Inductance Detectors, offering analogous advantages in multiplexing capabilities. TKIDs incorporate a superconducting resonator within a bolometer structure. Unlike TES bolometers, which monitor superconductor resistance changes, TKIDs gauge temperature fluctuations of a thermally isolated island through alterations in the kinetic inductance of the superconducting resonator circuit. With all power thermalized on the bolometer island, TKIDs permit electrical decoupling of the absorber from the resonator circuit, a departure from conventional KID configurations. This unique feature endows TKIDs with heightened engineering flexibility, allowing for independent optimization of the resonator and absorber components. The idea behind TKIDs technology is not new [47], and has been developed for different applications like X-ray photon detection [48] and THz radiation detection [49]. The originality of our implementation of TKIDs resides in targeting the detection of mm-wave in a sub-kelvin operational regime. Similar to other bolometers, TKIDs comprise a thermally isolated island where absorbed optical power, denoted as P_{opt}, is transformed into heat. This absorbed power elevates the island's temperature, T_i, surpassing that of the heat sink, maintained at a temperature denoted as T_b. The thermal island possesses a heat capacity denoted as $C(T)$, and it is connected to the heat sink through a weak link characterized by a thermal conductance, $G(T)$. The temperature differential across this thermal link generates a net power flow, P_{leg}, from the island to the heat sink. As explained in [43], the readout circuit of a TKID consists of a KID in which large capacitor C sets the resonance frequency f_0 , and smaller additional capacitors C_c couple the resonator to both the microstrip transmission line and to ground. The inductor, which acts as the thermometer, is on the island. A schematic representation of the electro-thermal system is reported in Figure 2.2 while SEM pictures of a fabricated device are reported in Figure 2.3. The total inductance L has a geometric inductance L_g due to the shape of the inductor wire and a kinetic inductance L_k from its superconductivity.

The kinetic inductance of a superconducting film, characterized by its thickness (t), length (l), and width (w), can be calculated based on the film's normal sheet resistance (R_s) and its superconductor gap energy (Δ). This relationship is expressed as $L_k = l/w \cdot L_s$, where $L_s = \hbar R_s/\pi\Delta$. This equation also defines the surface kinetic inductance (L_s), often used in electromagnetic simulations of superconducting resonators. The gap energy (Δ) is determined by the superconducting transition temperature (T_c) through the equation $\Delta = 1.763 k_b T_c$. Variations in L_k

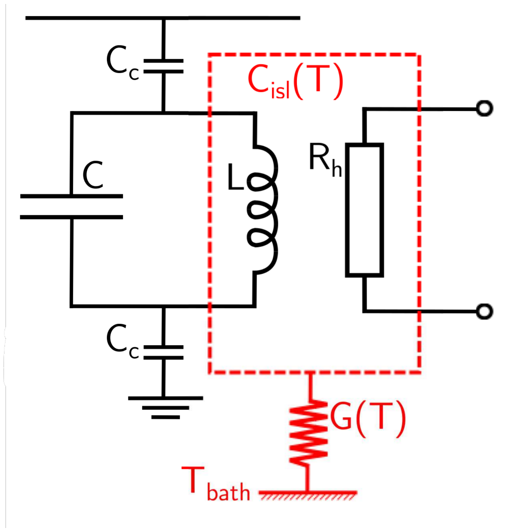

Figure 2.2: Electric scheme representation of a TKID taken from [43]. The red dotted box represents the thermally isolated island. The heater represented in this diagram is a valid representation for both: the resistor dumping the antenna's power and the calibration heater. Some device has both resistor on the islands to allow for a precise optical characterization.

due to temperature changes affect both the resonance frequency and the internal quality factor (Q_i) of the resonator. A higher kinetic inductance fraction, denoted as$\alpha_k = L_k/(L_g + L_k)$, enhances the responsivity to thermal fluctuations. Achieving a large α_k can be accomplished by minimizing geometric inductance through design considerations or selecting materials with higher resistivity or larger T_c values. Our TKID design also includes a gold resistor on the island that is ultimately wired out of the cryostat for calibration use. The heater resistor R_h is extremely useful for characterization and calibration purposes because it allows us to simulate a precise optical loading on the island with a power defined by controlling the current flowing into R_h. The absorber is in thermal contact with but electrically isolated from the inductor. This design allows for independent modification of the absorber (the antenna in this case) without affecting the resonator. Consequently, a Thermal Kinetic Inductance Detector (TKID) can seamlessly substitute a Transition Edge Sensor (TES) in a bolometer setup, leveraging existing radiation-coupling technologies like planar phased array antennas, horns, or lenslets [50]. Figure 2.2 shows a schematic of the thermal and electrical circuit of a TKID pixel that summarizes the discussion.

2.3 Device physics and noise

The goal of this section is to create a physical model of an ideal TKID bolometer so that the detector that we build has an internal noise below the photon noise requirement calculated in section 1.4 ($45aW/\sqrt{Hz}$). The main paper detailing the design of TKIDs is [43] and details all the principles here reported. Populating the TKIDs camera with photon noise limited detector is essential to demonstrate that the TKIDs technology is a suitable candidate for scaling superconductive bolometers.

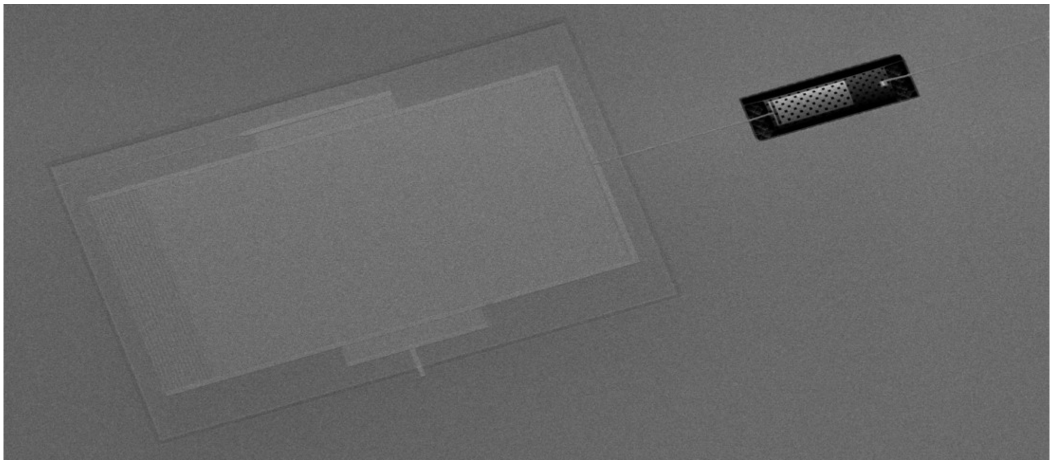

(a) Overview of the frequency multiplexed thermometric element. The light grey structure on the left encompasses the frequency setting capacitor and the coupling capacitor. The transmission line leading to the island is barely visible. The dark rectangle on the right is the TKID island, zoomed below.

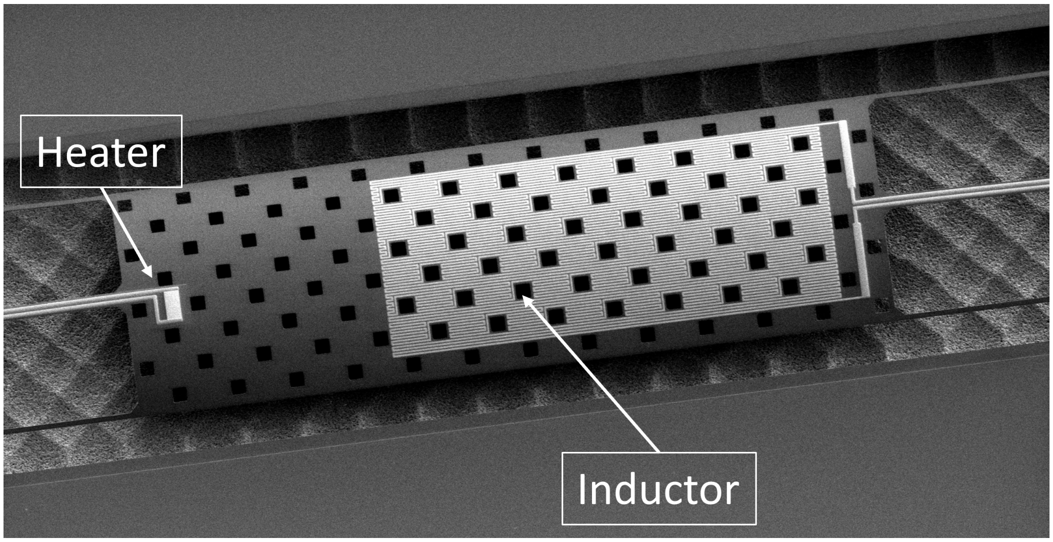

(b) Zoom in on the TKID island. In the picture, the inductor and heater structures are marked. The heater structure dissipate the power coming from an antenna. The calibration heater is a similar structure that is present on some of our devices and is similarly configured except for the wiring leading outside of the cryostat. The legs suspending the island over the released region are barely visible at the edge of the picture. The square holes pattern on the island facilitate the release process and avoids pressure build ups.

Figure 2.3: SEM (Scanning Electron Microscope) acquisitions of the thermometric element of a TKID. The top picture **(a)** is a larger image showing the whole resonating circuit. The bottom Figure **(b)** is a zoom in on the weakly thermally linked region of the bolometer: the island.

The way we approach our noise budget is to quantify the possible contributions to the detector noise other than the noise of the photon coming from the 150 GHz sky. The main sources of noise internal to detector that we expect are all well studied [51, 52, 53], in order of importance:

- Phonon noise: the phonons present of the island break cooper pairs in the inductor generating noise. There is a popoulation of phonons associated with the island temperature T_i even in absence of temperature fluctuations or power in the antenna's heater
- Generation–recombination (gr) noise: thermal fluctuations causing occasional quasiparticle excitations in the superconductor.
- Amplifier noise: the noise introduced by the RF cryogenic low noise amplifier necessary for the readout
- Two-level system (TLS): TLS noise comes from the interaction between the material's defects, such as impurities or film contamination, and the superconducting condensate. These defects create potential energy barriers that trap quasiparticles, leading to fluctuations in the local energy landscape.

The main goal of the design is to make sure that the most intense source of noise, phonon noise, is below the photon noise level. In order to understand the phonon noise we need to understand the thermal architecture of the device. Bolometer theory is well known [52], so after simple calculations we will focus on how the change in the thermometric element, from TES to KID, affects the design of the device. The thermal response of a TKID can be described using the following differential equation:

$$C\frac{dT}{dt} = -P_{\text{leg}} + P_{\text{read}} + P_{\text{opt}} \tag{2.9}$$

where P_{read} is the readout power dissipated by the inductor due to non-zero AC impedance. P_{leg} is the net heat flow through the thermal link suspending the island and P_{opt} is the power dissipated by the heater coupled to the antenna. C is the thermal capacity of the island. and T is the temperature of the island. We can model P_{leg} as $P_{\text{leg}} = K\left(T^n - T^n_{\text{bath}}\right)$, with K a coefficient, and n the power-law index. The thermal conductance of the thermal link is the derivative of P_{leg} with respect to the island temperature, $G(T) = n\ K\ T^{n-1}$. We will discuss P_{read} in more detail in the readout section. One of the key difference in swapping TES with a KID is that the operating temperature of the thermometric device P_{read} is much smaller than the incoming optical power P_{opt}. This means that, in normal operational regime, there is negligible electro-thermal feedback. Therefore, neglecting P_{read}, the temperature of the island T_i is set by the bath (silicon tile) temperature T_0 and the equilibrium condition $P_{\text{opt}} = P_{\text{leg}}$. We design our devices to handle $\sim 5pW$ of power with a bath temperature of $250mK$; this results in a design $T_i = 380mK$. T_i is really important in the design process as, given a target multiplexing factor and operating band, sets the quality factor of the resonators. The signal we are targeting can be expressed in terms of δP_{opt}, where $P_{\text{opt}} \sim P_{\text{atm}} + \delta P_{\text{opt}}$ and P_{atm} is the South Pole atmosphere at 150 GHz and the internal loading of the cryogenic telescope. Expanding equation 2.9 we can get the small perturbation to $\delta T_i \equiv \delta T$ given δP_{opt}. In Fourier space we get:

$$\delta T(\nu) = \frac{\delta P_{\text{opt}}}{G(T_o)} \cdot \frac{1}{1 + j2\pi\nu\tau_{\text{bolo}}}. \tag{2.10}$$

In equation 2.10, $G(T_o)$ represents the thermal conductance at operating temperature and is determined by considering the total optical loading P_{opt}. Given the bandwith constraints that will be introduced later and the packing required by the device count, we get $G(T_o) \sim 55$ pW/K. The handle used to control this parameter is the design of the legs supporting the island, visible in Figure 2.3 (b) as small segments going sideways respect to the island. Incorporating different films on the legs and changing the legs dimensions will radically change the thermal conductance $G(T_o)$ of the device without impacting the antenna design. The decoupling between the selection of the P_{opt} dynamic range and the absorber design represents one of the strength of the TKIDs technology. In equation 2.10, τ_{bolo} is the bolometer time constant, set by the ratio of thermal capacitance and thermal conductance (at each given temperature), it determines the bandwidth of the device. The selection of this parameter is handled via the manipulation of the thermal capacitance of the island. Removing less material from the island results in a lager thermal capacitance. The device bandwidth, $\nu_{\text{BW}} = 1/(2\pi\tau_{\text{bolo}})$ must be much larger than the science frequency band, i.e., $\nu_{\text{BW}} > \dot{\theta}/\theta_{\text{FWHM}}$ where $\dot{\theta}$ is the scan rate of the telescope and θ_{FWHM} is the beam size. τ_{bolo} is expected to be on the order of a few milliseconds, setting the device bandwidth at tens of Hz, which is fast enough for ground-based degree scale ($l \sim 80$) CMB observations. Having set the base parameter of our thermal design we can now estimate our phonon noise in therm of noise equivalent power (NEP) as:

$$\mathrm{NEP}^2_{\mathrm{ph}} = 4F(T_o, T_{\mathrm{bath}}) k_B T_o^2 G(T_o), \tag{2.11}$$

where the factor $F(T_o, T_{\mathrm{bath}})$ accounts for the temperature gradient across the bolometer legs[51]. For our design parameter we expect the leading source of noise to be $\mathrm{NEP}_{\mathrm{ph}} = 16aW/\sqrt{(}Hz)$.

At this point it is useful to describe how the fluctuations of the island temperature T_i reflect in changes in the transmission function of the device S_{21}. Changes in the island temperature $\delta T_i(t)$ result in the resonator properties to change. Specifically, a change in temperature affects:

- The resonant frequency: we define the generic quantity $\delta x = (f_r(t) - f_0)/f_0$ as the relative change of the resonant frequency respect to the case, f_0, where $P_{\mathrm{opt}} = 0$.
- The resonator power dissipation profile: an other generic quantity $\delta q_i = Q_i^{-1}(t) - Q_i^{-1}$ where again we take as a reference the original internal quality factor of the resonator. Note that we are only considering the changes in the internal quality factor as the rest of the coupling structure is off the island and thus thermally static.

Supposing now that the timing of the thermal fluctuations fits well in the detector bandwidth, we can expand S_{21} from equation 2.8 as:

$$\delta S_{21}(\nu) = \frac{Q_i}{4} \chi_c \chi_g e^{-2j\phi_g} \left[\delta q_i(\nu) + j2\delta x(\nu)\right] \tag{2.12}$$

where we defined $\chi_c \equiv \frac{4Q_r^2}{Q_i Q_c}$ as the coupling efficiency so that $\chi_c = 1$ at optimal coupling ($Q_r = Q_i/2$) and $\chi_g \equiv \left[1 + 4Q_r^2 x^2\right]^{-1}$ as the detuning efficiency so that these quantities relate the probe signal power P_g to the power dissipated by the resonator P_{read} as $P_{\mathrm{read}} = \frac{1}{2} \cdot \chi_c \cdot \chi_g \cdot P_g$. When the coupling is optimal and the detuning is zero, half of the input power is dissipated by the resonator [54]. In the case of TKIDs, only the inductive portion of the resonator is located on the thermal island. Therefore, the expression derived for P_{read} represents the maximum contribution of the readout power to the total loading on the island. In order to compute the small variations around the resonant frequency δx and total width of the resonator δq_i we need to consider the electrodynamics of Bardeen–Cooper–Schrieffe (BCS) superconductors [55]. Usually, we simplify by assuming that the superconductor state is completely determined once we know the quasiparticle density n_{qp}. The method of generating quasiparticles is a fundamental difference between standard KIDs and TKIDs. In KIDs, quasiparticles receive energy directly from photons, while in TKIDs, thermal phonons primarily generate quasiparticles. In aluminum TKIDs, the anticipated lifespan of quasiparticles τ_{qp} typically falls within $O(100\mu s)$, significantly shorter than the thermal time constant of the detector. Considering thermal quasiparticle generation as the primary mechanism, the overall quasiparticle density simplifies to the thermal quasiparticle density predicted by BCS theory:

$$n_{\text{th}} = 2N_0\sqrt{2\pi k_B T\Delta} \cdot \exp\left[-\frac{\Delta}{k_B T}\right]. \tag{2.13}$$

As expected, n_{th} depends on the temperature T, the gap energy Δ and the single-spin density of states at the Fermi level N_0. Changes in the quasiparticle density with temperature can be directly related to changes in the resonant frequency and dissipation using the Mattis-Bardeen equations by introducing β; the ratio of the frequency response to the dissipation response. β is a function of the probe frequency f and temperature T and for a thermal quasiparticle distribution, it is given by the equation:

$$\beta(f,T) = \frac{1 + \sqrt{\frac{2\Delta}{\pi k_B T}} \exp\left[-\frac{hf}{2k_B T}\right] I_0\left[\frac{hf}{2k_B T}\right]}{\frac{2}{\pi}\sqrt{\frac{2\Delta}{\pi k_B T}} \sinh\left[\frac{hf}{2k_B T}\right] K_0\left[\frac{hf}{2k_B T}\right]}. \tag{2.14}$$

K_0 and I_0 are the zeroth-order modified Bessel functions of the first and second order, respectively. At our targeted $T_o = 350$mK and $f \sim [400, \quad 800]$ MHz, $\beta >> 1$. In fact we measure $\beta \sim 10$ for our devices. This means that the resonator frequency shift channel provides a larger signal for thermometry than the resonator dissipation. Using β, we find that $Q_i \delta q_i = \left(\delta n_{\text{qp}}/n_{\text{qp}}\right)$ and $Q_i \delta x = \frac{1}{2}\beta(f,T)\left(\delta n_{\text{qp}}/n_{\text{qp}}\right)$.

Combining everything together we get the electrical response of a TKID to a small thermal fluctuation of the island:

$$S \equiv \frac{\delta f_r}{\delta P_{\text{opt}}} = \frac{\partial f_r}{\partial x}\frac{\partial x}{\partial n_{\text{qp}}}\frac{\partial n_{\text{qp}}}{\partial T}\frac{\partial T}{\partial P_{\text{opt}}} = f_r(T)\frac{\kappa(T)\beta(f,T)}{2\,Q_i\,G(T)\,T} \tag{2.15}$$

where

$$\kappa(T) \equiv \frac{\mathrm{d}\ln n_{\text{qp}}}{\mathrm{d}\ln T} = \left(\frac{1}{2} + \frac{\Delta}{k_B T}\right)$$

.

Other therms contributing to the internal noise of the detector are the generation–recombination (gr), TLS, and amplifier noise from the readout chain. All the noise terms add in quadrature:

$$\mathrm{NEP}^2_{\mathrm{total}} = \mathrm{NEP}^2_{\mathrm{photon}} + \mathrm{NEP}^2_{\mathrm{ph}} + \mathrm{NEP}^2_{\mathrm{gr}} + \mathrm{NEP}^2_{\mathrm{amp}} + \mathrm{NEP}^2_{\mathrm{TLS}}. \tag{2.16}$$

We consider each of these terms in turn and describe the conditions under which each of them remains sub-dominant to the phonon noise level. Generation-recombination noise occurs in TKIDs due to the stochastic nature of quasiparticle production and recombination processes. The behavior of the average quasiparticle population dynamics can be comprehensively described using non-equilibrium statistical mechanics [56]. The recombination rate of the quaiparticles is:

$$\Gamma_{\mathrm{rec}} = \frac{1}{2} V_{\mathrm{sc}}\, R\, n^2_{\mathrm{qp}} \tag{2.17}$$

where V_{sc} is the volume of the superconductor and R is a material property (recombination constant for Aluminum in this case). The lifetime of quasiparticles in case of a small perturbation of the density is given by:

$$\tau_{\mathrm{qp}} = 1/\left(R \cdot n_{\mathrm{qp}}\right). \tag{2.18}$$

Putting together equations 2.17 and 2.18, we can write the quaiparticle number as the one side spectrum $S_{\mathrm{gr}}(\nu)$ given as [56] :

$$S_{\mathrm{gr}}(\nu) = \frac{2\tau_{\mathrm{qp}}\, n_{\mathrm{qp}}\, V_{\mathrm{sc}}}{1 + (\pi \nu \tau_{\mathrm{qp}})^2} \tag{2.19}$$

where there is a factor two coming from the fact that the energy relaxation time is half the quasiparticle lifetime [57]. The generation-recombination noise equivalent power NEP_{gr} is the square root of the power spectrum divided by $V^2_{\mathrm{sc}} \cdot \left(\partial n_{\mathrm{qp}}/\partial P_{\mathrm{opt}}\right)^2$,

$$\mathrm{NEP}_{\mathrm{gr}} = \frac{G(T)T}{n_{\mathrm{qp}}(T)\, \kappa(T)} \cdot \sqrt{\frac{2}{RV_{\mathrm{sc}}}}. \tag{2.20}$$

Equation 2.20 shows that at high temperatures, gr noise is suppressed because the quasiparticle density increases exponentially with temperature. In addition, the responsivity, given in equation 2.15, is independent of the superconductor volume. Once again, the flexibility of decoupling the design of the radiation absorber and the thermometric element results in the possibility of reducing the generation-recombination noise by increasing the volume of the inductor. This is often not the case in traditional KID design because a large superconductive volume is associated with poor optical efficiency [58].

The next noise contributing phenomena that we are going to consider is the two level system noise (TLS). TLS noise in resonators is sourced by fluctuations in the permittivity of amorphous dielectric in the resonator. These fluctuations couple to the electric field of the resonator. Unlike the noise terms already considered, there is no microscopic theory of TLS noise. Instead, we apply the semi-empirical TLS noise model which is extensively covered in Gao's thesis [59]. TLS effects in the resonator also modify the internal quality factor and also introduce an additional temperature-dependent frequency shift. These two effects are given by

$$Q_{\mathrm{TLS}}^{-1} = F\delta_{\mathrm{TLS}} = F\delta_0 \tanh\left(\frac{hf}{2k_BT}\right) \cdot \frac{1}{\sqrt{1 + P_g/P_c}}, \tag{2.21}$$

$$x_{\mathrm{TLS}} = \frac{F\delta_0}{\pi}\left[\mathbb{R}\mathrm{e}\left[\Psi\left(\frac{1}{2} + \frac{hf}{2j\pi k_BT}\right)\right] - \ln\left(\frac{hf}{k_BT}\right)\right]. \tag{2.22}$$

Here, δ_{TLS} is the TLS contribution to the dielectric loss tangent, F is a filling factor that accounts for the fraction of the total electrical energy of the resonator that is stored in the TLS hosting material. An intuitive way to visualize F is as the fraction of energy stored in the material impurities. δ_0 is the loss tangent constant and Ψ is the digamma function[60]. At a probe tone power P_g and tone frequency f, TLS effects introduce a power dependence to the quality factor characterized by a critical power P_c. The fractional frequency shift is expected to be only weakly power dependent and positive with temperature increase. In the limit that $k_BT \ll hf$, the TLS loss drops off as $1/T$. Our target operating temperature is high enough to allow us to ignore the TLS effects on the resonator frequency and quality factor and only use the Mattis Bardeen relations.

The TLS noise power spectrum S_{TLS} in Hz^{-1} in the limit of strong electric fields is given as[59, 54]

$$S_{\mathrm{TLS}}\left[\mathrm{Hz}^{-1}\right] = \kappa_{\mathrm{TLS}}\left(\nu, f, T\right) \frac{\displaystyle\int_{V_{\mathrm{TLS}}} |\vec{E}(\vec{r})|^3 \, \mathrm{d}^3 r}{4\left[\displaystyle\int_{V} |\epsilon(\vec{r})\, \vec{E}(\vec{r})|^2 \, \mathrm{d}^3 r\right]^2}, \tag{2.23}$$

where $\kappa_{\text{TLS}}\ (\nu, f, T)$ captures the dependence on temperature and readout frequency, $\vec{E}(\vec{r})$ is the electric field, $\epsilon(\vec{r})$ is the dielectric constant, V_{TLS} is the volume of the TLS hosting media and V is the total volume. The electric field terms exhibit the measured $P_g^{-1/2}$ dependence on the readout power.

In order to compare TLS noise in devices with different geometry and operating conditions, it is more useful to use the microwave photon number N instead of the electric field. $N = E/(hf_r)$, where the E is the energy stored in the resonator. $E = \frac{1}{2} \cdot Q_i \cdot \chi_c \chi_g \cdot P_g/(2\pi f_r)$, from the definition of the internal quality factor. We must also account for the known saturation of the power dependence of TLS effects at low electric fields[60]. We can include this saturation factor and make the temperature and readout frequency dependence of κ_{TLS} explicit by rewriting S_{TLS} as

$$S_{\text{TLS}}\left[\text{Hz}^{-1}\right] = \kappa_{\text{TLS,0}}\left(\frac{\nu}{300\text{MHz}}\right)^{-\alpha}\left(\frac{T}{380\text{mK}}\right)^{-\beta}(1 + N/N_c)^{-\gamma}, \tag{2.24}$$

where $\kappa_{\text{TLS,0}}$ is a constant that sets the overall TLS noise level. The exponents typically have measured values[54] $\alpha = 1/2, \beta = 1.5 - 2$ and $\gamma = 1/2$. N_c captures TLS saturation at $N \ll N_c$ with the correct limit when $N \gg N_c$. We estimate $N_c \sim 7 \times 10^6$ from measured TLS critical powers of our devices, $P_c \sim -95$ dBm. For a practical estimation of TLS parameters we refer to Figure 14 of [54] to estimate $\kappa_{\text{TLS,0}} \sim 7.4 \times 10^{-23}$ Hz^{-1}. We specify $T = T_o$ and $f = 600$MHz, to obtain an upper limit of $S_{\text{TLS}}(1\text{Hz},\ T_o,\ -95\text{dBm}) \sim 5.2 \times 10^{-19}$ Hz^{-1}.

We can obtain the TLS NEP by dividing the TLS power spectrum by the power-to-fractional-frequency-shift responsivity

$$\text{NEP}^2_{\text{TLS}} = \frac{1}{\left(\partial x/\partial P_{\text{opt}}\right)^2} S_{\text{TLS}}. \tag{2.25}$$

In order to satisfy $\text{NEP}^2_{\text{TLS}} \ll \text{NEP}^2_{\text{ph}}$, the following condition must hold:

$$S_{\text{TLS}} \ll 4\chi k_B T_o^2 G(T_o)\left(\frac{\partial x}{\partial P_{\text{opt}}}\right)^2. \tag{2.26}$$

When we specify our design parameters, the condition reduces to $S_{\text{TLS}} \ll 1.6 \times 10^{-17}$ Hz^{-1}. The condition is satisfied because of the high responsivity $\partial x/\partial P_{\text{opt}} = 420$ ppm/pW^{-1} at T_o. The almost two orders of magnitude gap between the expected

TLS noise level and the upper tolerable limit gives us confidence that TLS noise will have negligible impact on our devices during normal operation.

The last noise contribution to consider is the additive noise of the amplifier. For an amplifier with noise temperature T_N and and at readout power P_g, the NEP contribution is given by[54]

$$\mathrm{NEP}_{\mathrm{amp}} = \frac{1}{\left(\partial x/\partial P_{\mathrm{opt}}\right)} \cdot \frac{Q_c}{2\,Q_r^2}\sqrt{\frac{k_B T_N}{P_g}}. \tag{2.27}$$

The amplifier noise contribution can be made small by using an amplifier with a low enough noise temperature or by biasing the resonators with a large readout power. Cryogenic low noise amplifiers with $T_N < 8$ K are readily available commercially and will be described in the next Chapter of this thesis.

We validate the model of noise we have built by measuring the noise of of a test device. The optical power is injected on the island via the gold calibration heater and the antennae of the device are not used because of the testbed in dark configuration. The full description of the setup, the RFI/EMI controlled environment, the readout technique and the pipeline for processing the raw data will be explained in Chapter 3. Although it may be premature to discuss Figure 2.4 and more closely in Figure 4.7 at this point, it shows the general agreement between the above prediction and the measurement, therefore confirming the validity of our electrothermal model.

2.4 Fabrication

Each TKID array comprises 64 dual orthogonal polarization detector pairs arranged in an 8x8 grid. Photons reaching the focal plane couple to the TKID bolometer through a planar phased array antenna. A picture of one of our tiles mounted to the focal plane is displayed in Figure 2.5 We have largely kept our antenna unchanged from the initial design first developed for TES bolometers on the Keck Array and subsequently deployed in BICEP3 and BICEP Array. We made only minor modifications to ensure the antenna layout is compatible with the TKID features on the same tile. Each antenna consists of 12x12 slot sub-antennas. The signals from each slot combine coherently in a microstrip summing tree to generate a well collimated beam that matches the f/2.2 telecentric refractive optics of a Keck receiver. For the TKID array, we adjusted the pixel to pixel spacing to 8.16 mm to accommodate the TKID interdigitated capacitors (IDCs). Each antenna couples to 2 bolometers, one for each polarization.

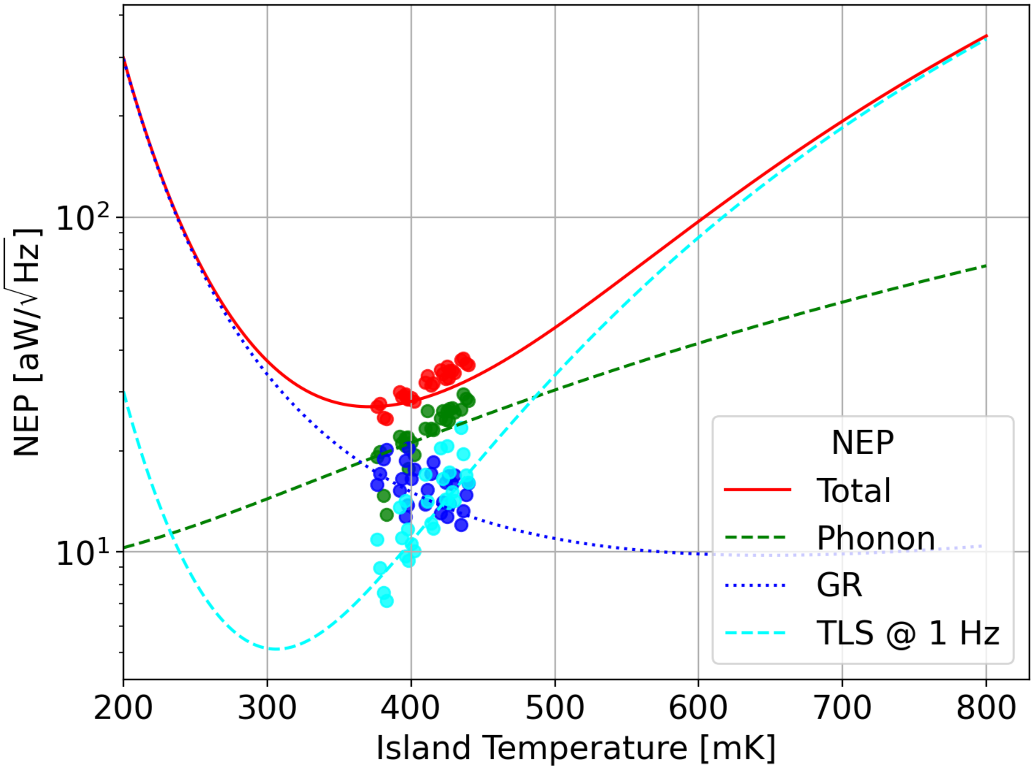

Figure 2.4: Overlap of theoretical noise model and noise measurements of TKIDs devices. The Y axis represent the noise equivalent power level, the X axis is the island temperature of the devices. The lines on the plot represent the theoretical predictions for the device noise in a dark configuration (optical load coming from the gold heater and not from the antenna) where the numerical parameter have been set according to the devices characterization. Specifically the red trace is the total NEP expected, the dashed green line is the expected phonon noise, the dotted blue line is the generation-recombination noise and the light blue dashed line is the two level system noise. The TLS component also includes the amplifier noise. The markers represent the results of the analysis performed on noise collected on the first generation of devices, see section 2.6. An example of noise acquisition with fitting is present in Figure 4.6 and a zoom in version of this plot is available in Figure 4.7.

Figure 2.5: Picture of a TKIDs tile (receiver side) mounted to the FPU. The islands containing the inductive elements are visible as the iridescent small rectangles; the dual polarization antennas are the bigger squares. The 8x8 grid is clearly recognizable and so is the absence of the corner antennas. The 8 corner detectors do not have an antenna by design and are referenced in this work as dark devices. The tile is held in place via four Beryllium-Copper cantilever clips.

Our targeted CMB science band centers at 150 GHz, with a 25% bandwidth. We determine both the upper and lower science band edges using microstrip filters. The filter is a 3rd order bandpass Chebyshev LC filter implemented using short sections of high impedance coplanar waveguide (CPW) inductors and short microstrip stubs as capacitors. The filter design represents a compromise between the bandwidth requirements and loss. Additional filtering in the optical path is achieved using a 6icm edge filter that we mount on the 2K stage of the receiver.

After filtering, we thermalize the optical power from the antenna for a single polarization on a meandered lossy 2.2 mm long gold microstrip line on the suspended bolometer membrane. The gold microstrip line remains open-ended, causing the incoming wave to reflect at the far end of the microstrip, resulting in an effective absorption length twice the physical length of the meander. The resistive and superconducting sections of the microstrip maintain the same width and are well matched. The ground plane underneath the gold meander electrically decouples the lossy gold microstrip from the superconducting aluminum inductor with a transition temperature $T_c \sim 1.2K$ on the island. We embed the inductor in a superconducting resonator circuit completed by coupling to a niobium IDC through niobium microstrip lines. The IDC capacitance sets the resonator frequency, and a smaller set of coupling capacitors couple the resonator to a hybrid CPW/microstrip readout line.

Each bolometer island is suspended from the tile on 6 silicon nitride legs. The 2 central legs are wide; one carrying the microstrip line from TKID inductor to capacitor and the other carrying the DC bias lines for a small Au calibration heater. The 4 outer legs are thinner; one carries the microstrip line from the antenna and the rest only have niobium ground plane deposited. The nitride layer is $\sim 350\ \mu$m thick. There is no additional metallization and the island thermal heat capacity is set by the nitride and oxide dielectric layer thickness as well as the Au, Al, and Nb metal layers.

To assess the wafer yield, each 4-inch wafer is wirebonded and cooled down to 100 mK before the bolometer islands are released in the final fabrication step. Unpaired resonators in a dual polarization pixel cannot be used for science data taking. Even so, these resonators are indispensible in characterizing the array. Our goal is to couple optical power through the antenna-filter path with its well defined beam and spectral response. However, a non-negligligble amount of power can couple directly to the TKID through the IDC or the bolometer itself. To study these, for all unpaired pixels, we etch opens the microstrip line from the antenna in 2 places to isolate bolometer from the antenna. These dark devices, after island release, can then be used to make measurements of the direct stimulation directly.

The Au calibration resistors are crucial for lab characterization but are not required for science measurements. To limit the complexity in the design and biasing, we bundle the calibration heaters in 8 separate channels, one for each row, each containing 16 heater resistors in series. This design enables us to access calibration data on every device of the array but creates some uncertainty on the amount of calibration power dissipated in a single resonator. Even so, the uncertainty is well constrained by the high uniformity of our gold films as measured during fabrication.

2.5 Quality control

This section is meant to provide an overview of our quality control protocol and will assume most of the fabrication process for the devices as the fabrication process, the design and actual fabrication work of the devices are an original part of a different work and deserve a space that deviates from the scope of this thesis. Although the fabrication standards, expertise, and equipment used are among the best available globally, the TKIDs fabrication process involves numerous steps, an apparently unlimited number of parameters, and ample room for error. The design of the devices aims to minimize single points of failure; however, the technology inherently relies on a crucial electrical connection: the RF line coupling to the resonators. The quality of this connection determines the outcome of the fabrication process. If the RF line is shorted or grounded at any point, the entire array of resonators is compromised, and the sample must be corrected or discarded. In order to deal with fabrication related problems we developed a quality control protocol. The fabrication process of TKIDs involves the deposition of the different geometries composing the device layer by layer.

The patterning of each layer can encounter different problems. Without going in the specific litographing technique used for each material or step we will focus on the zoology of problems encountered in this steps. This first step, as reported in Figure 2.6 is iterated ideally for every critical layer. A couple of examples are visible in Figure 2.7. Specifically in Figure 2.7b the RF feedline is visibly shorted with ground causing the S_{21} of the whole tile to be extremely attenuated and drastically reducing the signal to noise ration (SNR) of the tile. Am error in the RF transmission line patterning is fatal as the bias power need to overcome the short to ground makes all the devices before the short to be driven by an excessive amount of power while the devices after the short would no be biased at all. In this case a simple rerouting of the transmission line around the short fixed the problem. The patches do not necessarily need to be impedance matched as the length is such that the impact on the overall impedance of the line is negligible. In Figure 2.7a, an error in the inductor lithography is clearly visible. In this case there are two possible solutions: discard the affected device as its absence will not affect the rest of the devices on the tile or repeat the patterning step so to lay down the complete geometry. These two cases are partial crops of a significantly larger image taken with a Keyence microscope. These images are helpful in the detection of defects because they are the composite hundreds of images taken with very high magnification. The resulting image is the full view of the tile (4 in) and contains resolvable details in the $5\mu m$ scale. this results in a huge image with a data weight of around 1GB. Normal image editors and viewer often struggle at opening and navigating fluently such big images.

For the purpose of navigating the images we developed a web application that would take advantage of the Seaborn libraries [61] and the underlying tasselization algorithm to load on screen only the data necessary to the user. Some interactivity provided the user with tools to tag the kind of defect, interface visible in Figure 2.8 and finally output a report with the coordinate for each error and the associated visualization. An example of the report page is visible in Figure 2.9. Such reports

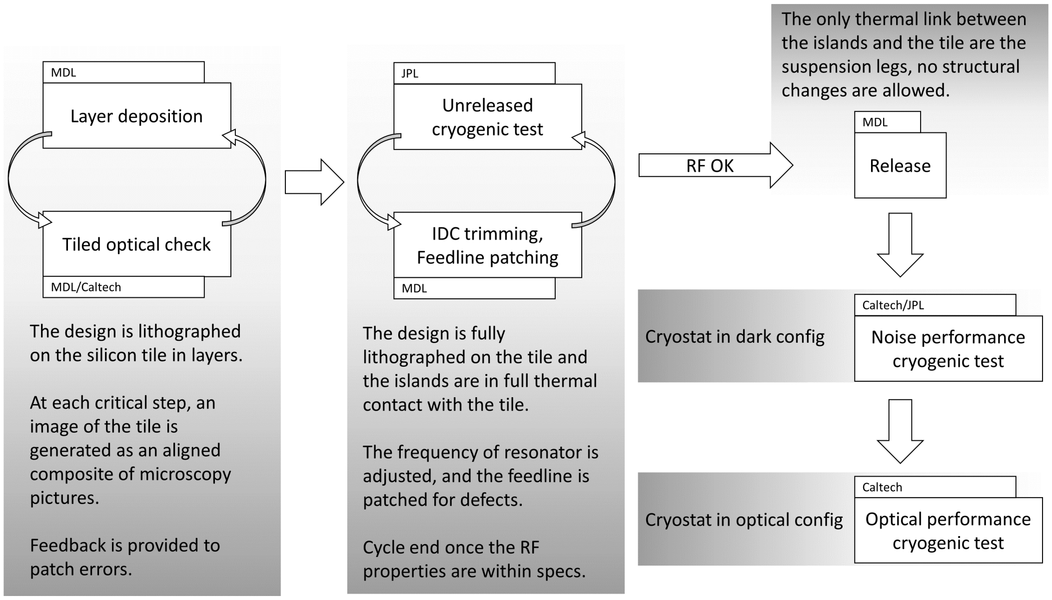

Figure 2.6: Diagram of the quality control cycle for 4 in tiles. There are four distinct phases in the process. The diagram reports a short description and the location where the test/procedure takes place: the Jet Propulsion Laboratory (JPL), the Micro Device Laboratory (MDL) is an internal JPL lab, The Caltech lab, situated in the basement of Cahill. The first phase is the layering of the tile: the geometric design is lithographed on the silicon tile in layers. After each critical layer deposition the tile is inspected. The inspection, reported as tiled optical check in the diagram, consists in the manual check of geometric features in images taken with a high magnification optical microscope. The term tiled refers to the stitching of multiple images taken with the microscope. The result of the stitching is a very large image that allows the person checking for defects to follow the geometric features and easily spot defects. A defect spotted in this phase can be easily corrected by repeating the layer deposition or applying more aggressive cleaning strategies. Once the planar geometry of the tile is defect-free, we cool down the array to check the RF properties. We measure the properties of the transmission line, S_{21}, and we extract the resonant frequency of the coupled devices. Due to fabrication and material variability the spacing of the resonant frequency of the detectors may be sub-optimal and cause cross-talk or overlap effects that would be detrimental to the final yield of the array. We design a strategy for trimming the inter-digitated coupling capacitors to adjust the resonant frequency of each single device. After the trimming the waver undergoes an additional cryogenic test until the RF performance, the free spectral range and the resonator yield i deemed acceptable. At this point the wafer re-enter the clean room at the MDL and gets released. The release process subtracts the material underneath the island leaving only the legs as thermal link between the tile and the island of each device. This step allows the temperature of the island to be directly dependant on the power dissipated by either the calibration heater or the antenna. At the same time, the fact that the islands is anchored to the tile exclusively by tiny legs, makes the device very susceptible to mechanical simulations and further clean room processing risks to break the legs, effectively bricking the device. After the release process the device is tested for noise performance in a cryostat with no optical window or dark. The diagram reports the configuration of the cryostat as the Caltech cryostat, named sK0, can be reconfigured to be either optical or dark.

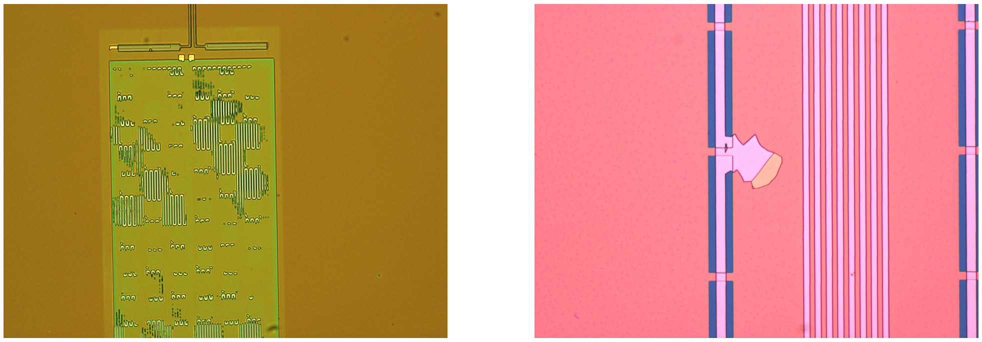

(a) The inductor on one of the islands was not completely lithographed. The bright yellow rectangle is the unreleased island of a TKID, the inductor patterning clearly went wrong.

(b) The RF line center conductor (light pink) on one of the tiles was shorted to ground (blue).

Figure 2.7: Fabrication defects examples. Such defects significantly impacted the development cycle.

would then be used by the clean room team to better drive a local inspection and evetual fixing of the device.

The difference between the first two steps of 2.6 is the actual testing of the device functionality. While in the first step the assessment is based on a prediction of performance on the basis of design adherence, the second step requires the device to be wirebonded, cooled down and tested. Once all the optical tests on the tile layers are completed, the tile is hybridized. The hybridization process simply consists in the electrical connection of the bond pads to the printed circuit board (PCB) via wirebonds. The PCB connecting to the wafer will expose the RF connection via standard connector (SMA series usually). The PCB than gets assembled in an holder. The holder is a metallic box suitable for transporting the device across labs and embedding the device in the cryostat for dark testing. An example of hybridized test chip is available in Figure 2.11. Once the TKID tile is hybridized in a dark holder we usually perform a LED map of the device. The LED map step consists in operating, at cryogenic temperatures, a grid of LEDs suspended on each device on the array with the intent of mapping the position of the devices. Although I personally developed hardware and software (micro-controller based, optically-isolated, LED mapper controller) for the LED mapping step, a thorough description of the process will be available on Dr. Wandui's thesis [40] which is more focused on device design and fabrication. For the purpose of describing the quality control process we will say that the LED mapping allows to trigger a

Figure 2.8: Web software interface displaying the buttons to draw rectangles on a tasselized images. Each color corresponds to a kind of defect. The category of the defect does not reflect any specific layer but rather the effect of the defect on the functionality of the array. A feedline problem cannot be ignored. A heater problem can potentially be ignored if fixing it would risk creating feedline problems. All the other problems, in blue, do not affect more than one device and can potentially be ignored. The user can pan and zoom freely, the backend records the absolute position of the box respect to the tile center and builds a report. In this specific screenshot we can observe two defects on the capacitor (blue boxes) and one on the feedline (red box). In the screen we can clearly see two islands (yellow patches) and the patterning of the dual polarization slot antennas (horizontal and vertical blue segments). A page taken from such report as an example is available in Figure 2.9.

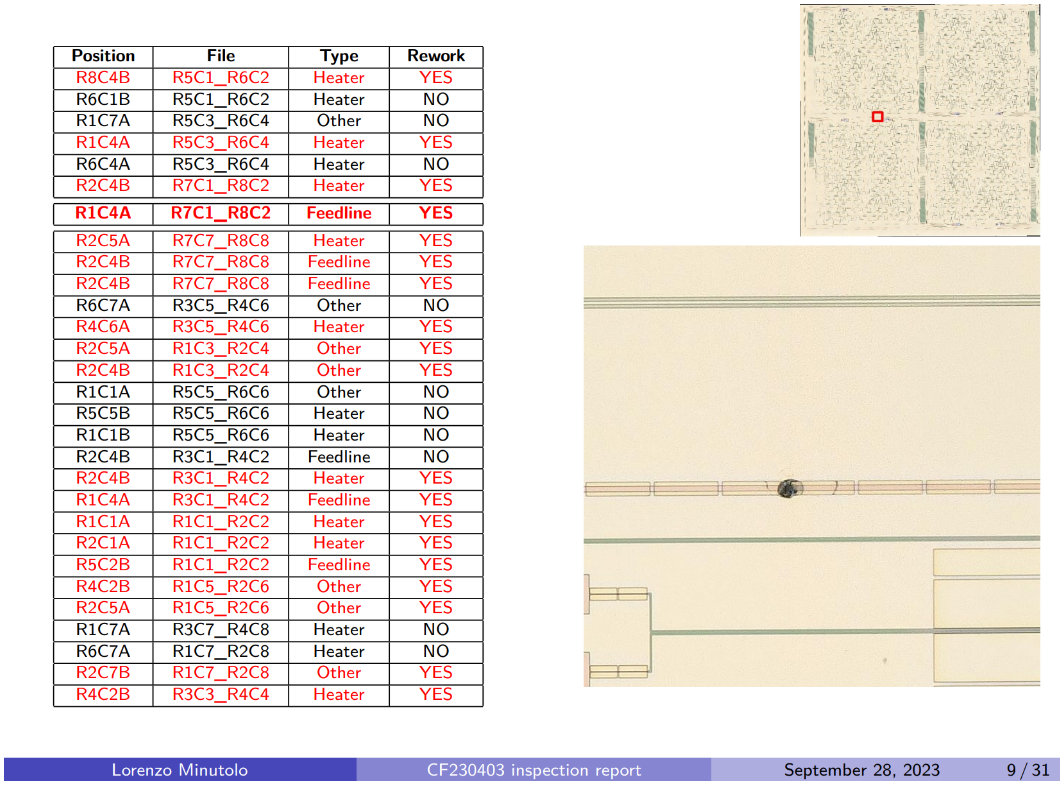

Position	File	Type	Rework
R8C4B	R5C1_R6C2	Heater	YES
R6C1B	R5C1_R6C2	Heater	NO
R1C7A	R5C3_R6C4	Other	NO
R1C4A	R5C3_R6C4	Heater	YES
R6C4A	R5C3_R6C4	Heater	NO
R2C4B	R7C1_R8C2	Heater	YES
R1C4A	**R7C1_R8C2**	**Feedline**	**YES**
R2C5A	R7C7_R8C8	Heater	YES
R2C4B	R7C7_R8C8	Feedline	YES
R2C4B	R7C7_R8C8	Feedline	YES
R6C7A	R3C5_R4C6	Other	NO
R4C6A	R3C5_R4C6	Heater	YES
R2C5A	R1C3_R2C4	Other	YES
R2C4B	R1C3_R2C4	Other	YES
R1C1A	R5C5_R6C6	Other	NO
R5C5B	R5C5_R6C6	Heater	NO
R1C1B	R5C5_R6C6	Heater	NO
R2C4B	R3C1_R4C2	Feedline	NO
R2C4B	R3C1_R4C2	Heater	YES
R1C4A	R3C1_R4C2	Feedline	YES
R1C1A	R1C1_R2C2	Heater	YES
R2C1A	R1C1_R2C2	Heater	YES
R5C2B	R1C1_R2C2	Feedline	YES
R4C2B	R1C5_R2C6	Other	YES
R2C5A	R1C5_R2C6	Other	YES
R1C7A	R3C7_R4C8	Heater	NO
R6C7A	R1C7_R2C8	Heater	NO
R2C7B	R1C7_R2C8	Other	YES
R4C2B	R3C3_R4C4	Heater	YES

Lorenzo Minutolo | CF230403 inspection report | September 28, 2023 | 9 / 31

Figure 2.9: Example of a page from an inspection report. The table on the left reports all the defects found in the octant. An octant is a microscope composite picture of eight devices. In the first column, the position of each tagged defect is reported to the closest coupling capacitor in the format RowColumnPolarization. The second column has a link to the specific file used. The "type" column report the kind of tag for the defect and the last column requires or not a rework of the tile. On the upper right there is a full view of the octant and a marker identifying the approximate position. The bottom right is a magnified version of the defect. The row with a double border indicated the current defect. The goal of such reports is to inform the fabrication team of the defects we spot on the device and guide a real time inspection and the eventual clean room patching.

frequency shift in a localized device. By knowing the design frequency, the actual frequency and the position of the TKID we can calculate the required frequency shift so that the difference between the design and the actual resonant frequency is minimized. Knowing the required shift, we determine via simulation (using Sonnet EM software [62]) how many fingers of the IDC to cut in order to move the resonant frequency. Once the capacitors have been trimmed we hybridize and cool down the device again and measure the new resonant frequencies to check for spacing uniformity. The result of the process can be observed in Figure 2.10. We can clearly observe that the distribution of the FSR between devices becomes more peaked. A uniform FSR between devices helps to avoid the overlap in resonant frequency and minimized the cross-talk between devices.

The release process consists in removing the material underneath the island leaving only the legs as a link between the islands and the tile. The mechanical properties of the legs are such that after the release process a tile cannot be sent back to the clean room for processing as most of the necessary cleanings and more generally most of the processing, would brake the legs and destroy the devices. The release effectively freezes the device properties. After that step, characterization activities can take place. Optical and noise characterization before the release process is not particularly useful to yield science grade devices as the thermal physics of the device radically changes with the release (it becomes a bolometer). The characterization steps will be discussed in Chapter 4.

2.6 Development milestones

Until this point we treated TKIDs devices as either ideal or bundled in a beautifully designed, densely packed array. The road between these two points deserves a mention in this work. The first generation of TKIDs fabricated at JPL for the purpose of cosmological measurement was back in 2016 and was just a prototype chip with few resonators on it. In 2017 the first device with few released devices was hybridized and tested. A picture of the first prototype is in Figure 2.11. That device worked according to design but had no antennas, only test heater for calibration. The first antenna coupled TKIDs chip was tested at JPL in a cryostat in dark configuration in 2018 and iterated the performance of the first prototype. We needed to wait one more year, 2019 to have a testbed capable of making the measures required to verify the optical functionality. A picture of the ACT-TKIDs (Antenna Coupled TKIDs) chip mounted in the Caltech cryostat (sK0) before the close-up is available in Figure 2.12. Optical results were very promising and noise performance were

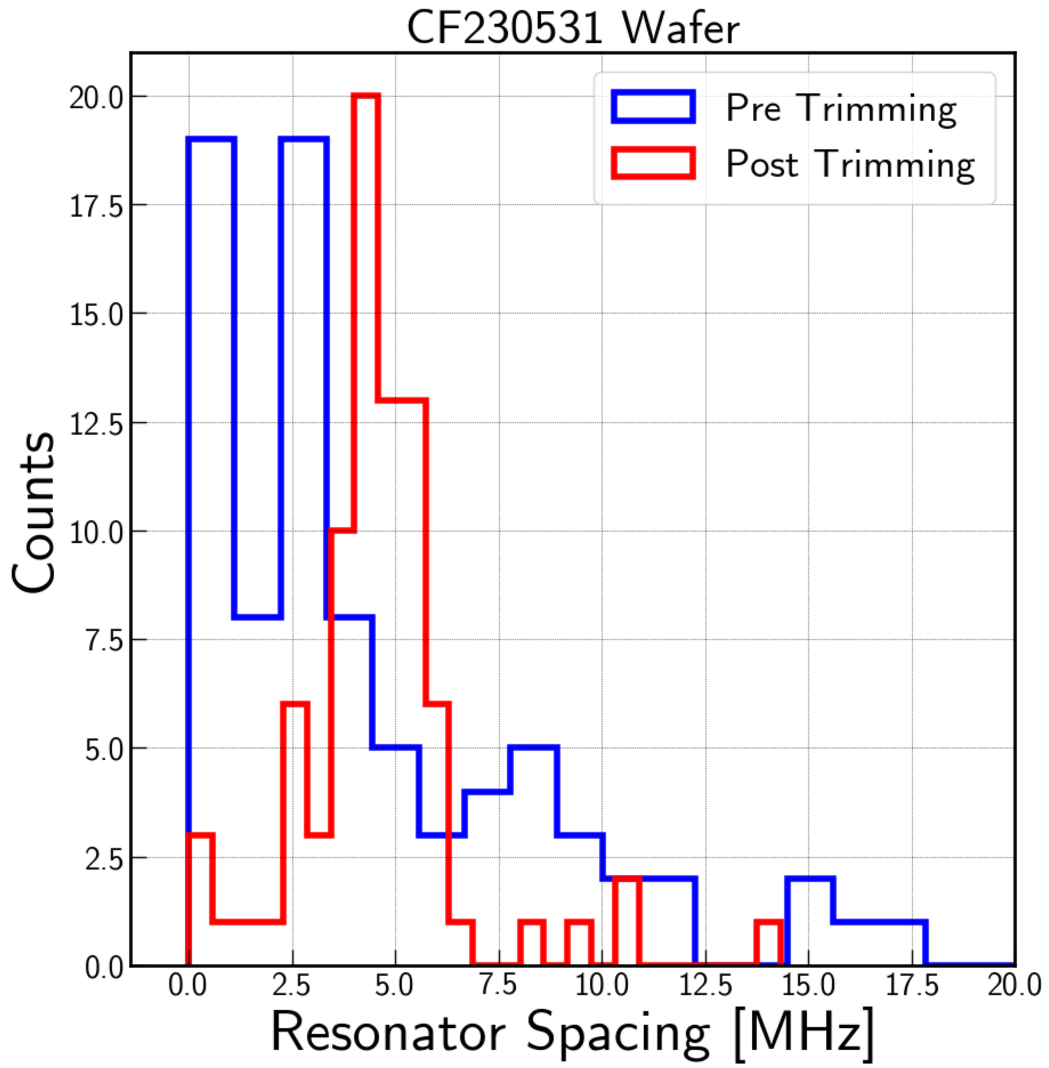

Figure 2.10: Histogram of the resonant frequency before and after the capacitor trimming. Figure probably taken from Dr. Wandui's thesis [40], work in progress at the time of writing. On the T-axis there is a count of devices, on the X-axis there is the distance between two neighbouring devices in frequency space. The effect of trimming the resonator capacitor to shift the resonant frequency is that the spacing between the resonator is more uniform. A uniform spacing helps to avoid overlaps of resonant frequencies and minimized the crosstalk between devices in a fixed band.

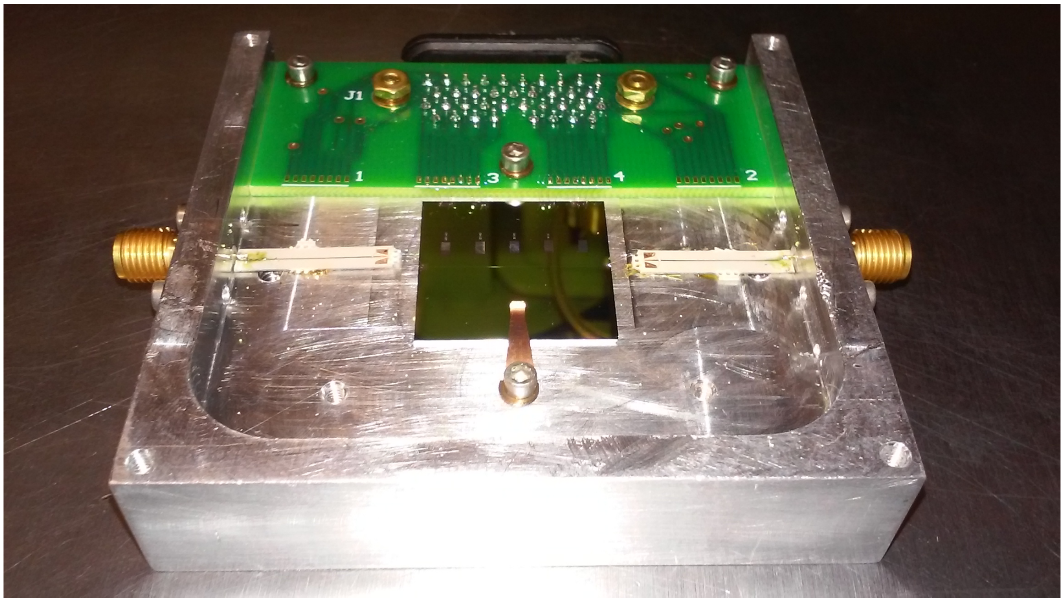

Figure 2.11: Hybridized test chip fabricated and tested in 2017. A few devices are visible as iridescent details on the silicon chip in the center. The silicon chip is hel in place with a copper clip. The RF line is hybridized to a couple of launchers, terminating in standard SMA connectors. The calibration heaters are hybridized to a PCB that wires each heater terminal out via a micro-D connector. The Aluminum support allows for a cover to be installed for dark testing.

consistent with the 2018 tests. The success of the chip-scale devices prompted the development of the first science grade tile with the design reviewed in section 2.4. 2019 was the beginning of an interesting historical event [63] that drastically reduced the fabrication output of the Micro Device Laboratory (MDL) at JPL as well as the accessibility of the facilities used to test the devices. Even with restricted facilities we managed to fabricate and test at least two different generations of 4 in tiles. These two middle generations suffered various problems during fabrication that made them not suitable for science observation. A shift in the instrumentation used to fabricate the tiles, as well as the development of the fabrication quality control protocol discussed in section 2.5, resulted in the first two science grade tile being tested in a deployment ready apparatus, see Figure 2.13. Most of the testing reported on this thesis is performed on these two tiles.

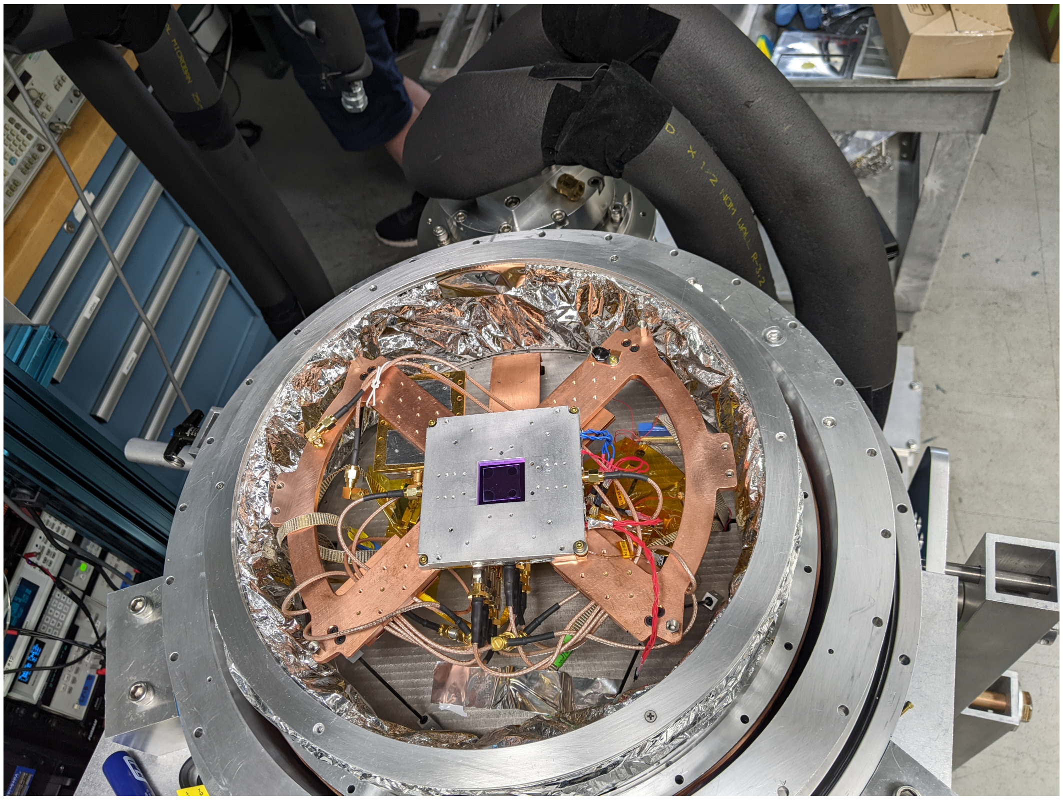

Figure 2.12: AC-TKIDs (Antenna Coupled TKIDs) chip mounted in sK0 at Caltech, ready for optical characterization. In the Figure the 300K, 50K, 4K shields are visible as aluminum rings around the butterfly shaped copper plate. The copper plate sits at base temperature when the cryostat is in operation and allows for quick installation of FPUs or test chips. The copper plate ultra cold (UC) stage is a novel addition to the Keck cryostat that is inspired by the main BICEP Array cryostat. The mechanical modifications to the Keck cryostat will be discussed in detail in Chapter 3

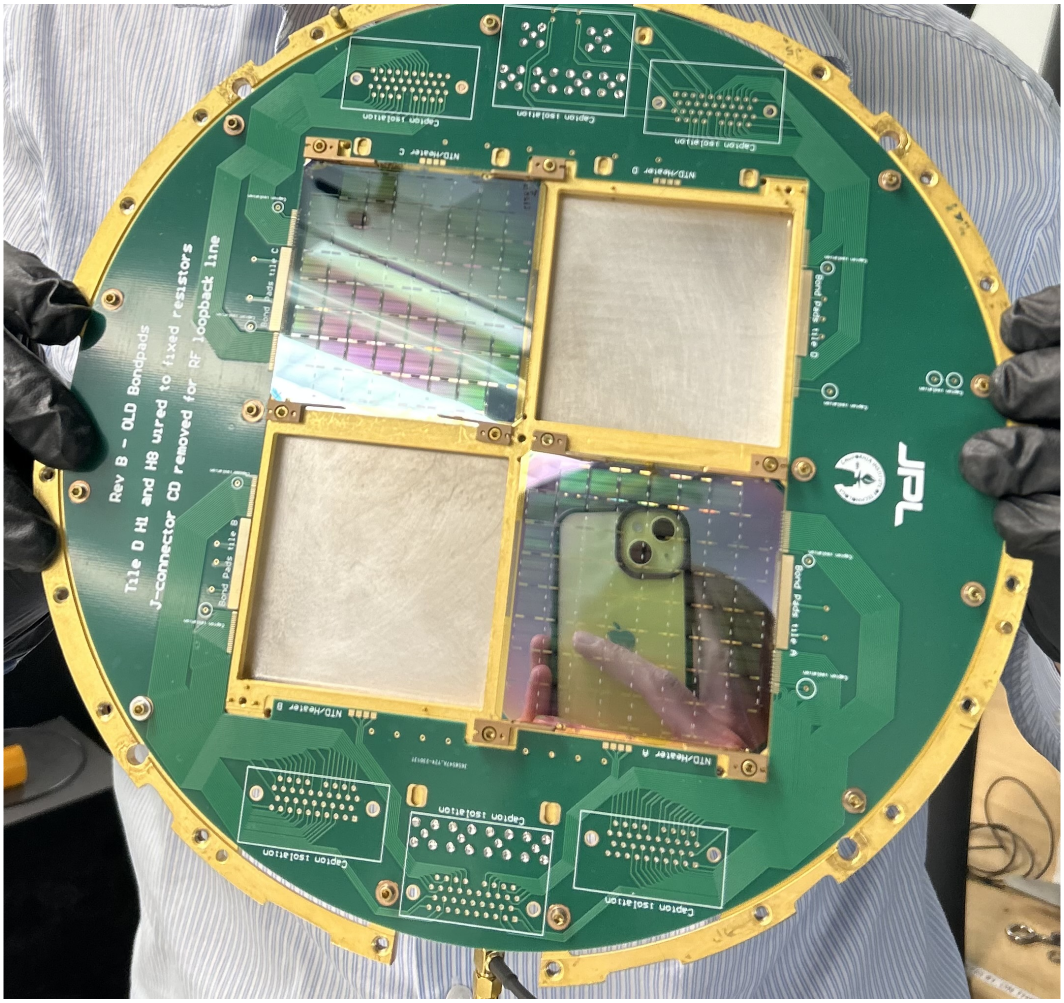

Figure 2.13: Focal Plane Unit (FPU) with two tiles hybridized on it. In the Figure I am holding the FPU assembly with no backshot cover exposing the telescope side of the two tiles. The gold plated thermalization plate edge is visible as the FPU contour. The traces connecting the calibration heaters to the connectors are exposed on the top layer of the PCB. The PCB is version B, not the final revision, some technical annotation are visible. The design and assembly of the FPU will be discussed in detail in Chapter 3. The device in this picture is the main deliverable of this work. The successful deployment of such device would represent a significant TRL advancement for TKIDs technology.

Chapter 3

INSTRUMENT SYSTEM ENGINEERING

This chapter will explore the system engineering behind the cryogenic mm-wave polarimeter, the principles used to accelerate its development and trade-offs needed to make it a deployable solution.

3.1 Cryogenic system

The cryogenic system used in this work are mainly the Adiabatic Demagnetization Refrigerator (ADR) system at JPL and a prototype Keck cryostat at Caltech (K0/sK0).

Adiabatic Demagnetization Refrigerator

Most of the noise characterization has been performed in a Model 103 Rainier Adiabatic Demagnetization Refrigerator (ADR) [64] cryostat from High Precision Devices (HPDs) with a Cryomech PT407 pulse tube cryocooler [65]. The practical advantage of using ADR systems resides in the short cycle time, which is ideal for rapidly testing samples from the clean room. The time efficiency of the ADR cycle has been fundamental for getting the quality control iterations described in section \ref{sec:qc} completed in a reasonable time frame. The ADR cryostat does not have the UC cooling power of the Caltech sorption fridge cryostat and does not need it: we operate the ADR cryostat exclusively in dark configuration. The lack of an optical window also reduces the number of parts in the mechanical assembly, allowing the system to reach 4 K (standard temperature for operating the ADR) on the cryocooler in ∼ 2 days. No particular instruction is needed to load the samples; a single person can complete the whole operation. The cryostat is also used as a benchmark for the fundamental noise study of the detector because, being very light, it has never induced microphonic noise in the samples. The RF chain in this cryostat is limited to 1 transmission line and follows the same principles that will be discussed in section 3.3. The main difference from the transmission line standpoint is the use of Niobium-Titanium (NbTi) [66] RF coaxial cable assemblies instead of more innovative solutions used in sK0. Mechanically, the UC stage can accommodat

Keck cryostats: K0 and sK0

The main cryostat used in this work is one of the first prototype of Keck cryostat [67] named K0 throughout this thesis. K0 is operated in the Cahill basement at Caltech. Although the K0 cryostat is very similar to the standard Keck cryostat described in [67], a host of mechanical modifications have been implemented to speed up the turnaround time for testing devices and to accommodate a frequency multiplexed readout chain instead of a TDM one. This section will first introduce a standard Keck cryostat and then focus on the main modifications that were made.

The Keck cryostat, depicted in Figure 3.1, incorporates a Cryomech PT410 two-stage pulse tube cooler installed with vibration isolating bellows. According to Cryomech's specifications, the first stage of the PT410 can maintain a temperature below 50 K while dissipating up to 45 W of power. This significant cooling capacity enables the sinking of three separate infrared blocking filters to the 50 K stage of the pulse tube. Similarly, Cryomech's specifications indicate that the second stage of the PT410 maintains a temperature of approximately 3.5 K with 0.5 W of conducted power, rising to around 4.25 K at 1.0 W, a condition nearly unaffected by the power applied to the first stage. We have extensively tested the cryogenic performances of K0 and compared them to the datasheet. This comparison allowed us to quantify the thermal performance impact of each new modification. Furthermore, these tests allowed us to diagnose cryogenic problems with ease. Figure 3.5 shows the cryogenic performance dataset.

Due to the finite cooling capacity of the PT410, meticulous attention has been paid to the design of mechanical supports to minimize parasitic loads on the 4K stage and to the design of heat straps to optimize their thermal conductivity. Each cold stage is supported mechanically at the back end of the cryostat by three sets of two-member carbon fiber trusses. These trusses consist of two carbon fiber rods epoxied into aluminum blocks. The old trusses that came with the cryostat broke following a rapid, accidental depressurization of the cryostat and had to be replaced. A new compatible mechanical design and fabrication process was developed and tested; see Figure 3.2.

At the front end, the cold stages are supported by three v-shaped grade 6 titanium “boomerangs“. These pieces exhibit high stiffness in the radial direction but flexibility along the cryostat's axis, allowing for a significant differential thermal contraction between the 300 K and 50 K stages. Titanium was selected for its high stiffness and its favorable yield-strength to thermal conductivity ratio at low

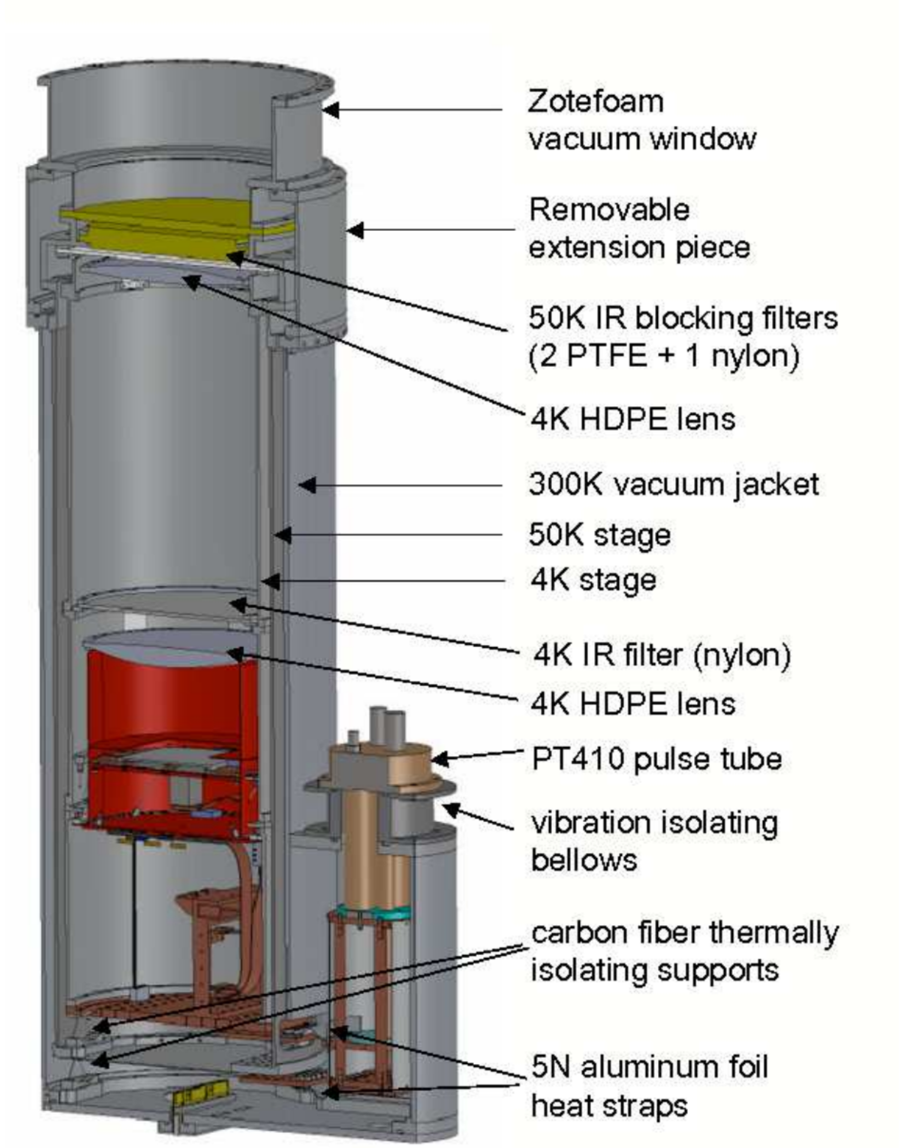

Figure 3.1: Cross section of the original Keck cryostat, Figure taken from [67]. While the concept, the components functionality and the general assembly of the cryostat remained the same, many modifications were performed to speed up the turnaround time of devices testing. This Figure illustrate the general assembly of the cryostat and the main optical and thermal components.

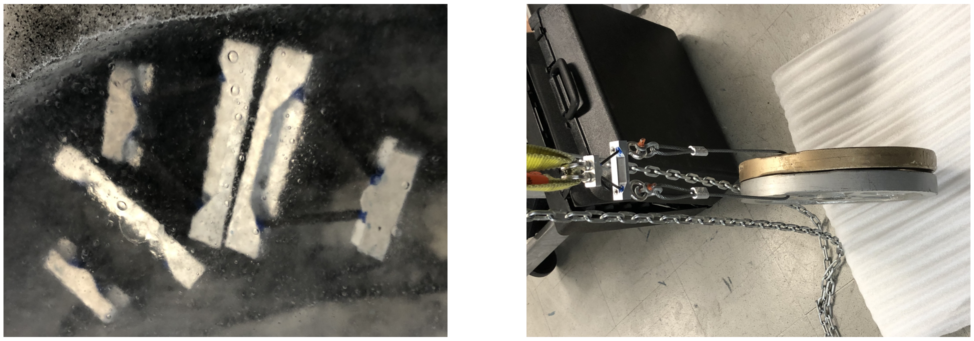

(a) Thermal shock process of the leg assembly.

(b) Mechanical testing of the leg assembly after thermal shock, 100 kg

Figure 3.2: A few steps from the fabrication process of new cryostat legs. Cryostat legs are a cryogenic mechanical component that allows a stage of the cryostat to sit on top of the inner support ring of another stage. The legs must support the heavy axial weights of most of the internal components of the cryostat and, at the same time, limit the thermal conductivity between the two stages. The material of choice is carbon fiber because of the axial strength that can be achieved with small diameter rods. In this Figure we show the complete assembly under test before being installed in the cryostat. In Figure **a**, we are thermalizing the assembly with a bath of liquid nitrogen with the purpose of creating thermal shock. In Figure **b**, we are testing the radial strength of the assembly using a pulley and some weights (100kg). Only the replicas of the assembly that manage to withstand both these processes are considered for cryogenic operations.

temperatures, necessary to accommodate the radial differential thermal contraction between stages. The boomerang (and why they are necessary) are clearly visible in Figure 3.3 alongside a clear picture of the stage nesting.

Another significant difference in the cryostat build respect to Figure 3.1 is the replacement of aluminum foil heat straps with electron beam welded braided copper heat straps. These new heatstrap are the standard on BICEP Array cryostats and the items availability meant that we could get $\sim$ 1.5 K less temperature drop between the pulse tube head at 50 K and the 50 K lenses.

The main difference between K0 and its evolution, sK0 is the 300K volume and the assembly disassembly strategy. In orfer to access the 4K volume of K0, as well as the US stage, every cylindrical tube of the cryostat had to be released from the leg and boomerang support and extracted from the external 300 K tube. Once the 4 K cylinder and the UC stage were free from the rest of the cryostat, all the internal heatstraps, connecting the fridge to the IC and UC plates had to be disassembled. The whole disassembly process would take around 5 FTE (Full Time Equivalent)

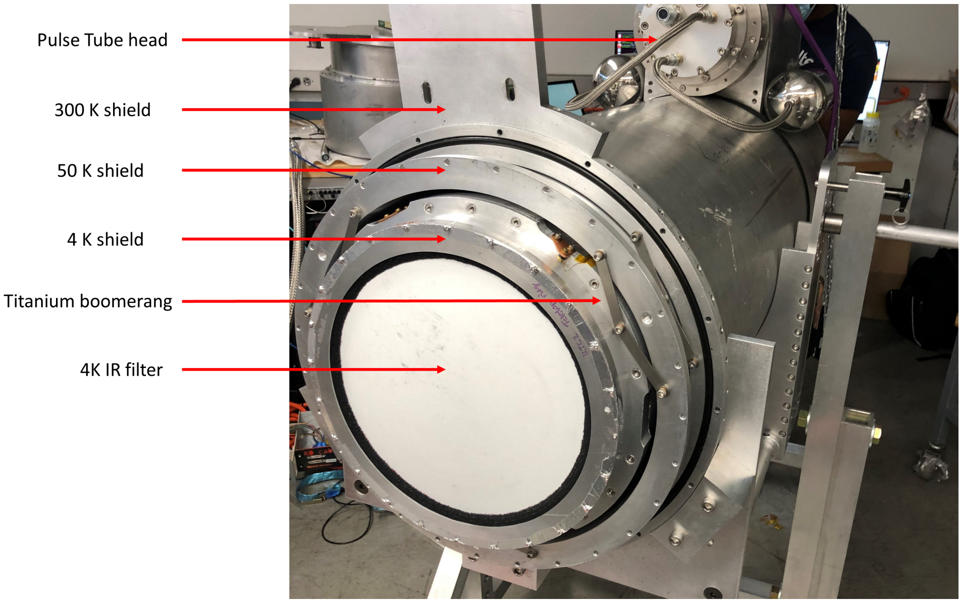

Figure 3.3: View of K0 during the assembly process, Multiple components of the cryostat are exposed and the nested configuration of the stages is clearly visible. It was not uncommon to rotate the telescope during the assembly and disassembly phases to better access the bottom panel of the cryostat. In this specific picture, Dr. Wandui is attaching the heatstraps.

to be completed and 7 FTE to be reverted in an operational form. Disassembling the cryostat is a very frequent operation during superconductive detectors R&D activities as each sample change or optical configuration change would result in having to access the UC stage. The modification that lead to a short version of K0, as the same suggest sK0, is the shortening of the 300 K shell and the shortening of the 50 K shell. Shorter tubes meant that the disassembly of the optical stack alone would allow access to the UC stage and thus simplify a lot the operations. Less material to cool down also meant faster cooldown time to 4K and decreased radiative heat from the 300 K shell to the 50 K shell due to the reduction in exposed area. The new turnaround time with this modification allowed 1 FTE to disassemble and reassemble the cryostat in a different configuration or with a different sample. Both 300 K shells, for K0 and sK0, are visible in Figure 3.4 alongside a few of the new shells we designed and ordered.

When modifying the Keck cryostat to make use of the sK0 shells, we toke the time to characterize the performance of the pulse tube in both configurations, K0 and sK0, and compare them to the nominal datasheet provided by Cryomech [65]. In order to do this, we assembled the cryostat without any component except the 4 K and 50 K shells. We added a heater per each stage and used them to dump

Figure 3.4: Picture of the unpacking of the sK0 shells. The K0 cryostat (in grey) is much taller than the sK0 300 K shell (in blue). We designed the sK0 shell so that we could access the UC volume of the cryostat without having to fully disassemble the telescope. The implementation ofg this new mechanical assembly lead to a much faster testing turnaround time, from 10 FTE minimum to 1.

a controlled amount of power. The results are available in Figure 3.5. The plot illustrated the temperature of each stage when a power load is applied to each stage. The performances of sK0 were mixed in comparison to K0. While the 50 K stage consistently resulted in higher temperature, even without load, the 4 K stage outperformed K0. Most likely this effect is caused by the Multi Layer Insulation (MLI) [68] not being optimal. Because of supply chain issues, in order to optimize the lead time for the commissioning of sK0, we had to hand saw the MLI using Aluminized Mylar. The performance of sK0 were more than enough to complete the optical characterization of the science grade tiles.

At the core of both K0 and sK0 there is a Chase $^4He/^3He$ sorption refrigerator [69], similar in performance to the GL10 [70]. The heatstraps connecting the Helium refrigerators to the IC and UC volume are designed and manufactured in house. With a shortened and more easily accessible cryostat, we needed to implement a mechanical assembly that would allow us to quickly swap focal planes, test chips and tile holders without having to disconnect the UC heatstraps. We redesigned the Keck UC volume by implementing a flexible UC stage, some techical drawing is available in Figure 3.6. Instead of directly connecting the UC strap to the backshort plate and the thermalization plate, the heat straps connects to a Copper plate that sits

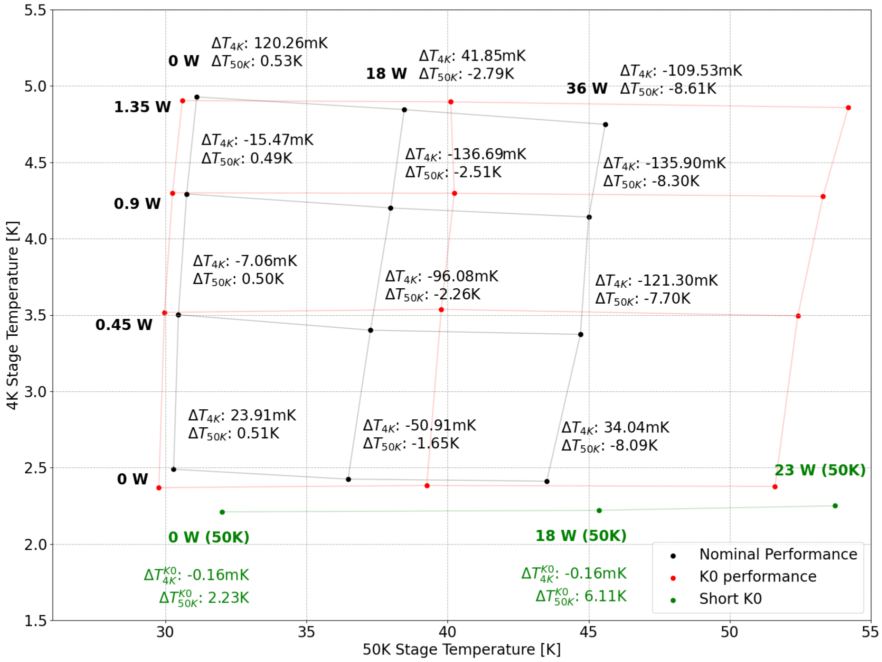

Figure 3.5: Comparison between measured K0, sK0, and datasheet [65] cryogenic performance. The black dots are the representation of the nominal performances. The red marker are measured K0 performance and the green dots are measured sK0 performance. On the Y-axis there is the equilibrium temperature of the 4 K stage, on the X-axis there is the equilibrium temperature of the 50 K stage. Various powers are applied to the 4 K and the 50 K stage, the power value is available at the left and top of the points as a bold text. We also report the variation respect to nominal performance in terms of ΔT_{4K} and ΔT_{50K}. While the 50 K stage consistently resulted in higher temperature, even without load, the 4 K stage outperformed K0. Most likely this effect is caused by the Multi Layer Insulation (MLI) [68] not being optimal. Because of supply chain issues, in order to optimize the lead time for the commissioning of sK0, we had to hand-saw the MLI using Aluminized Mylar.

on the carbon truss legs. The copper plate, Figure 3.6B, has mounting holes for UC heatstrap mounting protected by steel Keen inserts and it is permanently installed in the cryostat and does not need to be changed between runs. The additional weight introduced by the UC stage Copper plate could have caused the whole leg suspended UC stage to be more susceptible to pulse tube induced vibration. We compensated the weight variation by re-machining the backshort plate, Figure 3.6A, in Aluminum instead of Niobium. The original backshort plate was machined in Niobium to provide the detectors with better magnetic shielding: the idea behind the Niobium magnetic shield is that it becomes superconductive at a higher temperature respect to the detectors and allows the expelled magnetic field to dissipate. TKIDs do not share the same concerns TESs have about magnetic susceptibility. More specifically, the fields we expect to deal with in the laboratory or deployment environment have an intensity order of magnitude lower respect to the fields used to generate any effect in KIDs [71]. We thermalize the FPU assembly, Figure 3.6C, to the UC Copper plate using Copper reach-around solid strap, Figure 3.6D. In Figure 3.6B, a threaded hole pattern is visible on the top view of the UC Copper plate. The threaded hole pattern is used to guarantee the compatibility with different devices other than the FPU, such as tile holders and test chips. An example of non-FPU setup is reported in Figure 2.12.

3.2 Electronic system

This section aims to describe the essential electronics used to run the experiments. We will mainly focus on a general description of the predominantly commercial housekeeping system and the fully custom calibration instrument we built.

Housekeeping

An essential part of any cryogenic system is the housekeeping. Housekeeping is needed to monitor and control the internal temperatures of the cryostat and operate the Helium sorption fridge. The challenge of integrating the readout system in K0 and sK0 is the stratification of components and the management system that has historically been adopted with the cryostat. We will mostly ignore the housekeeping system of K0 and directly describe the system implemented simultaneously as the K0 to sK0 transition. The transition forced us to disassemble the cryostat entirely, and we felt it was the right moment to reorganize the whole system. Instead of listing each component used by the housekeeping, we will describe the functional aspects of each category.

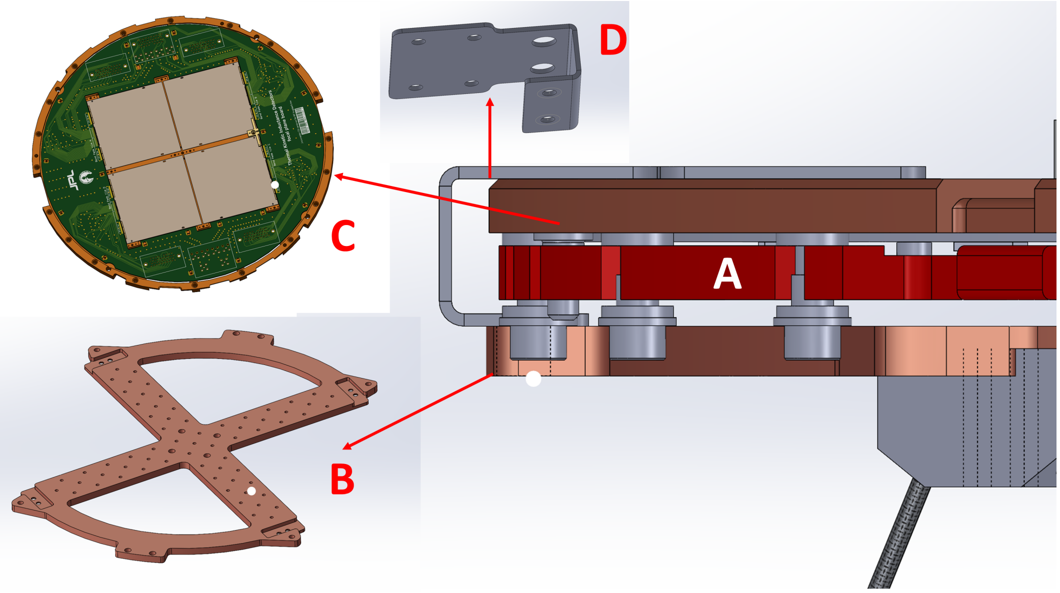

Figure 3.6: Technical drawings of the newly developed UC stage for sK0. **A** Aluminum backshort plate. **B** UC stage Copper plate that allows FPU, tiles holders and test chips to be quickly mounted on the stage. **C** FPU unit without the backshort. Top copper thermalization plate and signal distribution PCB are visible. **D** Reach-around Copper thermal strap.

- **Cernox thermometers**: Cernox is actually a registered trademark so famous it gave the name to cryogenic thermistors. The operation principle is quite standard: the resistance of a material changes with temperature. Given a calibration curve, one can recover the temperature information. The implementation however is not trivial. The change in resistance caused by a temperature shift in the order of a few mK is minuscule respect to the resistance of the cryogenic DC wires running in the cryostat. For this reason a 4 wire measurement is needed. The instrument of choice to perform the resistance measure is the Lakeshore 370 AC resistance bridge [72], or LS370, visible in Figure 3.10. The LS370 allows us to measure the resistance of up to 16 Cernoxes using a 11 Hz sine wave and using as little as 100nA to perform the measure. The channel multiplexing is sequential and it takes roughly 5 seconds for a resistance to be measured. Due to the cost of calibrated thermometers, we use Cernoxes only in locations where power dissipation is a concern such as inside the sorprion fridge, on the UC and IC heatstraps and on the FPU.

- **Diode thermometers**: In a fashion similar to the thermistors above, specially designed diodes from Lakeshore are commonly used when a sub mW power dissipation is not a problem. The working principle is a subtle change in voltage gap induced by a temperature change. The advantage of using diodes for measuring the temperature is that only two terminals are needed and the calibrated diodes are much cheaper. We use diodes for measuring all the temperature in the cryostat above 4K such as the temperature of the pulse tube head, the optical lenses and the cold electronics. The instrument of choice for the diodes readout is the Lakeshore Model 218 cryogenic temperature monitor [73], visible in Figure 3.10. This instrument uses DC to read out the diodes and switches between up to 16 channels at 32 Hz.

- **Heaters**: Heaters are needed in our cryostat for three main purposes: diagnostic, fridge cycling and temperature control. The diagnostic heaters are mounted on all the heatstraps of the cryostat and allow us to measure the performance of the pulse tube refrigerator, as in Figure 3.5, as well as the quality of thermal junctions. Thermal junctions have been routinely disconnected and reconnected as part of the integration process of new devices, hence the need to quantify the quality of the junction (thermal grease application uniformity, surface cleaning and smoothing, metal oxide presence and junction pressure can greatly affect the heat transfer). Fridge cycling also makes use of heaters, specifically for controlling the ^4He and ^3He pumps and heat switches. There is no particular instrument used to drive the heaters, two HP 3632A bench-top power supply, visible in Figure 3.10, had enough channels and bandwidth for temperature regulation, diagnostic and fridge cycling.

The manganin (a trademarked name for an alloy of typically 84.2% copper, 12.1% manganese, and 3.7% nickel) wires connecting the heaters and thermometers terminate on a sealed bottom flange exposing 3x Micro-d 100pos connectors, visible in Figure 3.7. We inherited the bottom flanges from the standard readout scheme of Keck cryostats supporting TDM readout architecture; the high density cables were dedicated to both readout and housekeeping. We decided to keep the bottom flanges and repurposed them for housekeeping and calibration signals. The cabling displayed in Figure 3.7 is a custom cable designed to transport the signal from the housekeeping elements to signal distribution box. The custom design of the cable was required due to the nature of the high-density, military grade connectors: there are no available cable harnesses for these connectors and the one that were previously used with K0 had terrible RFI/EMI performances. The new design of the cables envisioned a double shielding for the whole bundle and an individual ground

Figure 3.7: Bottom plate of the cryostat with custom housekeeping cables connected. Two 100 way cables are sufficient to operate the cryostat and diagnose most of the cryogenic problems. A third slot on the same plate is left unused. In the picture the RF front-end plate is visible (central) sporting 8 SMA RF connectors. An addition housekeeping-like plate is visible with the label “Tile C“. This last plate is used to route the calibration signals for the TKIDs array.

shield for each of the $\pm I$ and $\pm V$ couples needed for the 4 wires measurement as well as for the diodes pair readout. The cables were designed, prototyped and tested in house using in house machined harnesses and MDM100 pigtails assemblies. Once the design was optimized, 5 copies of the cable assembly were ordered to Pickering Engineering [74] for production.

The cable assemblies visible in Figure 3.7 carry all the signals needed for the operation and monitoring of the cryostat. The distribution of these signals among the intended instrument is performed by a custom designed PCB, the signal distribution box. An annotated routing document of the signal distribution box is reported in Figure 3.8. The role of the box is to split the signals coming from the high density cable assemby to the respective instrument while avoiding noise crosstalk between the lines. To achiebve such goal, the $\pm I/V$ connection pairs and the power supply lines were considered as 50 Ω differential transmission lines (matched to

±200 mils). The layer topology consists in 4 signal layers interleaved with 4 ground planes. Of the 4 ground planes, half are referenced to the UC stage and the other are referenced to the cryostat shells. This distinction is needed because the two parts are separated by a substantial resistive impedance. The principle behind the routing strategy programmed in the autorouter of Altium designer is to isolate the differential pairs belonging to different instruments with the most amount of ground-connected copper possible.

Software-wise, each instrument had a GPIB port communicating with a single dedicated machine executing the pyHK software [75]. The software automatically record data, executes automated actions and exposes a web interface for controlling the instrument cluster and exploring past data. A screenshot of the web interface with a cryogenic cycle visible is available in Figure 3.9. pyHK's automation features were used for cycling the cryostat overnight and stabilize the temperature of the FPU via a software PID loop during most of the measurements.

Battery operated calibration bias

A fundamental subsystem of the experiment is the instrument used to bias the calibration heaters on the TKIDs. Each tile has 8 calibration lines and each line is connects 16 resistors in series. The resistors must be measured in cryogenic conditions because both the resistor and the on-tile connections have different properties at sub-Kelvin temperatures. In order to measure the resistances of the heaters at cryogenic temperatures, each heater line exposes two bondpads on the tile edge, each is wirebonded to the FPU signal distribution board onto 2 different pads. This allows us to connectorize 4 terminal per heater line and perform 4 wire measurements using the same instrument used for housekeeping, the LS370 [72]. The resulting measures are extremely close to the design value, see Figure 3.11. This adherence to the design specification gives us confidence that the distribution of the resistance across the series is uniform.

The biasing of these resistors allows the direct deposition of power on the TKIDs island. TKIDs are designed to be extremely sensitive to temperature fluctuations on the island. The design specification is a NEP floor at 1 Hz of 20 $aW/\sqrt{Hz}$. In order to be able to simulate the design optical load and to calibrate the design at that power (6 pW), the noise introduced by the bias resistor must be below the noise of the detector. Different instruments have been tested for the purpose, ranging from benchtop power supplies and high resolution function generators to

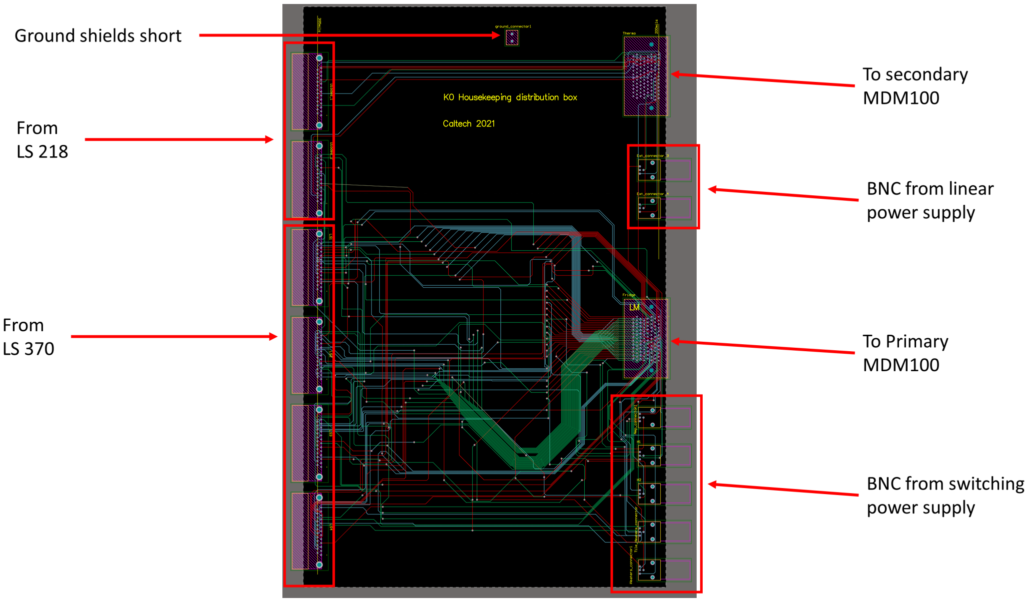

Figure 3.8: Signal distribution box routing design document with connector functionality annotation. Although there is no active component on this board, and the only components used are connectors, the topology of the routing plays an important role in noise control. The logic behind the connector placement hides the DB25 connectors in the back, two of them attached to the LS218 and 4 of them attached to the LS370 because these connections are rarely undone; the front panel exposes the switching and linear power supplies isolated BNC connectors as the choice of the instrument was not immediate at the time of design; all these connectors are routed onto 2x MDM100 connectors leading on the bottom plate of the cryostat. The routing of the traces aims to minimize the crosstalk between different lines. Each $\pm I/V$ couple has been treated as a differential 50 Ω transmission line. Each couple of line has been routed on 4 of the 8 copper layer present on the board. 2 of the layers on the boards are reserved for grounding and another 2 layers are reserved for RF grounding. The difference in the ground arises from the fact that there is a substantial resistive impedance between the shielding of the UC volume and the rest of the cryostat shields. The two grounds can be shorted using the appropriate terminal (connected to a panel switch). The routing of the instrument traces tends to create the maximum amount of ground connected copper between differential pairs belonging to different instruments. The routing strategy was implemented as a autorouter strategy in Altium designer 14. Manual adjustments were performed for practical reason after the autorouting.

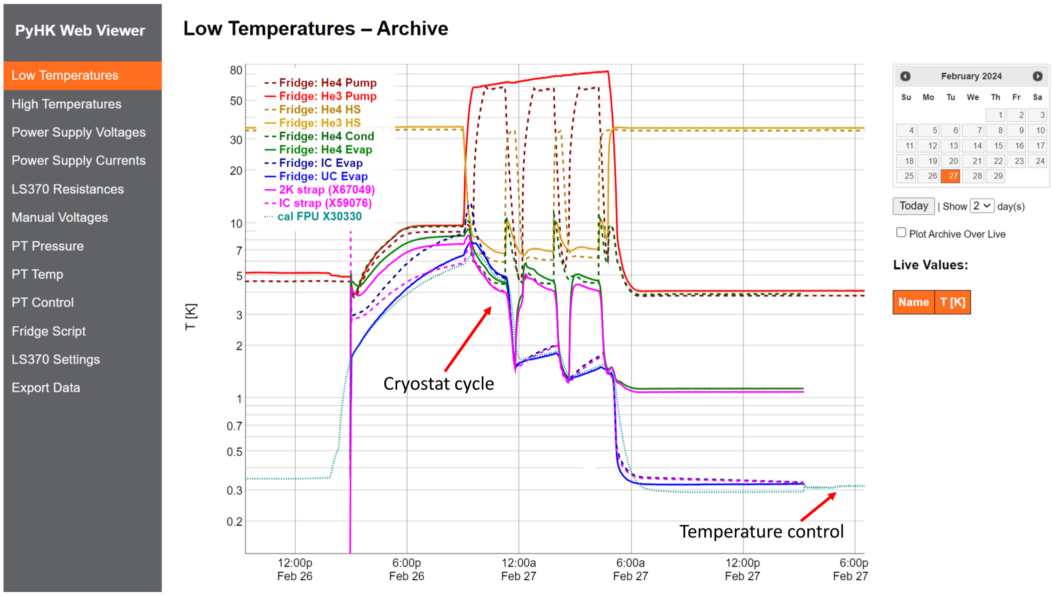

Figure 3.9: Screenshot of the pyHK webviewer. On the left there is a panel that allows tthe configuration of the instrument cluster, on the right there is a panel for exploring historical data. The data plotted represent a typical sK0 day: first there is the sorption fridge cycle during the night and then most of the thermometers are disabled to allow more bandwidth on the FPU Cernox for temperature control via PID loop. Credit for this software goes to [75]. The cryostat cycle is a standard helium-3/4 sorption cycle [76] in which we repeat the Helium 4 cycle trice in order to condensate more working fluid. A single Helium-3 cycle is sufficient to provide the extra cooling power to reach 250 mK in optical configuration and 200 mK in dark configuration.

specialized commercial precision current source, battery operated and not. While some of these tools had a noise low enough to perform optical efficiency measure and other studies on the device, the power calibration and the acquisition of a NEP spectrum of the internal noise of the device required a different approach. We designed a battery operated, fully analog circuit capable of keeping the cryostat in a stable state, supply power to the cryogenic low noise amplifiers (LNAs) in the readout chain, and generate the bias and calibration signal for the TKIDs. The goal is to consolidate the essential functionalities needed to perform the measures and pack them into a single, more controllable, circuit that can run the whole experiment for a few hours while providing a cleaner noise environment. The top view board planning of the instrument is reported in Figure 3.12.

We designed the battery box to use the instrument cluster to stabilize the cryostat in a state with enough condensed helium to run a full day of experiments, disconnect the housekeeping instrument cluster, and connect the newly designed battery box.

Figure 3.10: Instrument cluster for K0/sK0 housekeeping and detector readout. On the left rack there is the room temperature RF readout chain that includes an Ettus SDR, a GPU sevrer, a packet broker and a box containing RF amplifiers, filters and linear power supplies. On the right rack there is the housekeeping server, the LS370 for controlling the Cernoxes, the LS218 for reading out the diodes, the switching power supplies for operating the heaters and the signal distribution box. This picture was taken during the commissioning phase of the lab.

Once connected, the battery box keeps the cycle of the cryostat running, the RF readout chain active, and allows the user to bias the detectors programmatically. For this purpose we design a battery logic that uses rechargeable chemically stable batteries [78] to provide unregulated power. We regulate the power using a standard configuration of the LT30XX chip family. The LT30XX [77] chip family is an ideal candidate to provide a stable, low noise power supply for different reasons: these DC-DC voltage regulator have a very high power supply reject ratio (PSRR) that allows for some RFI pickup in the battery cabling; the voltage is selected using a single resistor that we can choose to be an ultrastable 1PPM/C unit; these voltage regulators have internal thermal compensation logic. The clean power supply is then used in different functional blocks across the PCB:

- **Heat switches control**: an ulterior LT30XX is used to convert the positive power supply to the voltage required to drive the Helium 3/4 heat switches in the cryostat sorption refrigerator. Using another LT30XX represents an over-engineering for the task of dumping power in a resistor. The design flexibility offered by the chip and the possibility to select the voltage with a

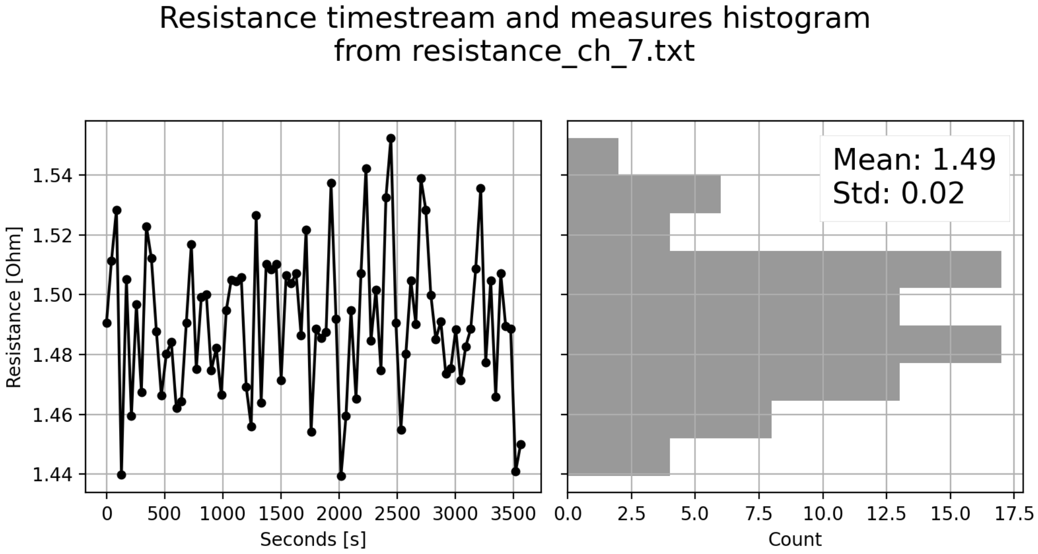

Figure 3.11: Four wires resistance measure of a heater channels on a TKID tile, performed with the LS370 resistance bridge. On the left plot there is the timestream of the measurements, on the left there is an histogram of the measures. Each heater is supposed to be 0.1 Ω. There are 16 heater in series hence we expect a resistance of 1.6 Ω . We measure a resistance of ∼ 1.5 Ω . The small deviation is most likely due to some imperfection in the gold deposition process during fabrication. We assume each heater to have a resistance value of 1.5 Ω/16 in our calculation for the power dissipated on the island during testing and calibration.

panel varistor, not to mention the reduction in component diversification on the board drove the design choice.

- **LNA power supply**: We want the cryogenic low noise power supply to be active when conducting any kind of measurement. The already very clean power supply is used to drive a LT6655, an ultra-stable, thermally compensated reference diode [79]. The voltage from the LT6655 is used to drive a differential instrumentation operational amplifier. The role of this last amplifier is to allow for some current draw (30mA max per LNA).

- **Heater bias**: Biasing the heater is the main purpose driving the design of this instrument. The bias signal can be described as a square wave plus an offset. The offset dictates the simulated optical load of the islands (6pW of power dissipated on each of the detectors in series, see Figure 3.11). The square wave around the offset (amplitude « offset) is used in the calibration phase to measure the respone of the detector at the given bias. The offset voltage V_o generation is identical to LNA power supply bias. The square wave generation

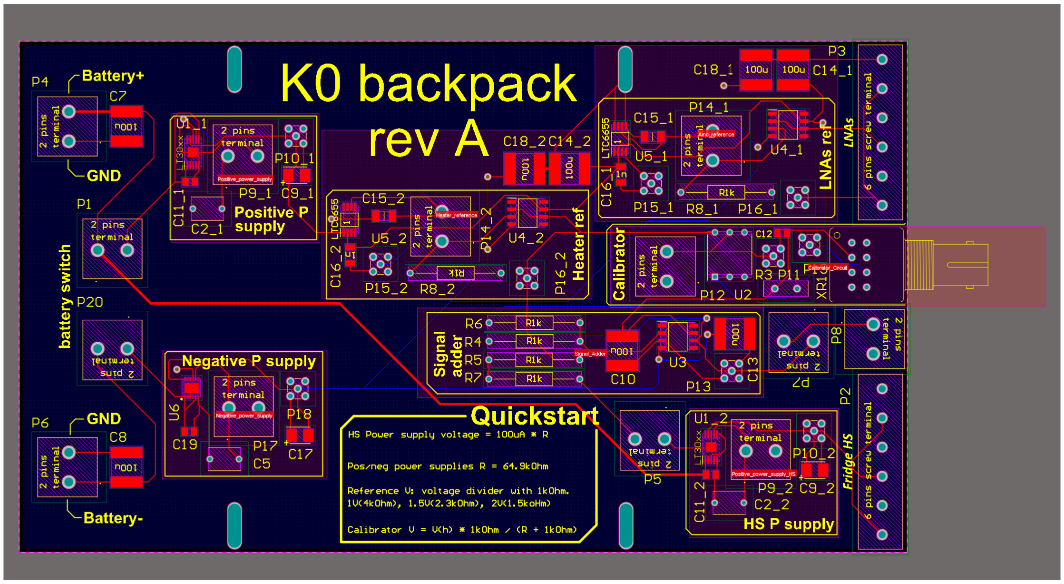

Figure 3.12: Board planning for the sK0 calibration battery box. The revision A here reported has a physical layout organized by functional blocks and allows the user to modify various parameters of the device by placing different resistors in the parts named “2 pins terminal“. Starting from the left we first encounter an few unboxed (without yellow overlay contour) components that connect the PCB with two batteries and a panel ON/OFF switch that also allows for battery recharging. The battery logic is followed by the two power supply blocks. Each is realized using a standard configuration of the LT30XX chip family from analog devices [77]. These power supplies take the voltage from the battery, which can be anywhere in the [6 - 30] V range and regulate it down to a user defined value, 5.5 V in our initial design. The "Heater ref" generates the main static offset of the bias signal that will determine the simulated optical load of detectors, the "calibrator" interprets an optical signal and converts it to a voltage difference which is a configurable percent of the main bias. The signal adder uses a very stable operational amplifier to sum the calibrator and reference signal. The final signal is then applied to the heaters via bias resistor to moderate the current and select the power level. The "HS P supply block" provides power to the heat switches internal to the cryostat so that the UC volume keeps thermal contact with the sorption fridge. The "LNAs ref block" provides a very stable power supply to the cryogenic low noise amplifiers. The final terminal blocks allow easy connection of the PCB with the panel mounted MDM100 connector and the optical fiber link allows for device programming while maintaining electrical insulation from the potentially dirty RFI/EMI environment of the instrument cluster rack.

> consists in the generation of a new voltage V_c from the attenuation of the offset signal and the addition of the two signals. The final signal generated by the on-board signal adder circuit is the offset plus the square wave modulated by an optical fiber input. In the presence of optical fiber signal the heater bias V_b will result in $V_b = V_o + V_c$. if there is no signal on the optical fiber $V_b = V_o$. This logic enables the programmatic control of the calibration signal without any elecrical connection between the housekeeping instrument cluster and the cryostat. The current output of the heater bias logic is controlled by two identical, high precision, 1PPM/C resistors.

The battery box circuit is then assembled in a connectorized meal box and the internal temperature is controlled via the continuous readout of a thermistor. Double conductive Copper tape is applied on each metal seam for RFI tightness. The box is operated on an anti vibration foam layer.

Under these condition we used an HP 3563A signal analyzer to extract the noise spectrum of the generated bias signal (static, no optical fiber signals). The results are reported in Figure 3.13

3.3 RF system

This section aims to describe the radio-frequency system apparatus used to read out the TKIDs in K0 and sK0. We describe the general readout chain first, the room temperature analog electronics components, and finally the cryogenic RF signal distribution.

RF readout chain

The RF readout chain for TKIDs treated in this work has been optimized for a continuous fixed tone comb readout and has been designed to be easily transported and installed in an other-than-sK0 Keck style cryostat. The readout starts with the probe signal generated at the resonator frequency (usually 300 MHz for test chips and 600 MHz for science-grade tiles). The probe signal undergoes filtering and attenuation so that no spur frequencies enter the cryostat, and the base noise level is the 300K noise of a resistor (-173.82 $dBm/\sqrt{Hz}$). The initial attenuation is also calculated to deliver an optimal -95 $dBm/\sqrt{Hz}/resonator$ on-chip. Coppper coaxial cables connect the SMA flange on the bottom side of the cryostat with the 300 K side of a bundled Cryoflex cryogenic RF cable assembly. The Cryoflex cryogenic RF cable assembly, or simply Cryoflex in this thesis, is a bundle of 8 RF transmission

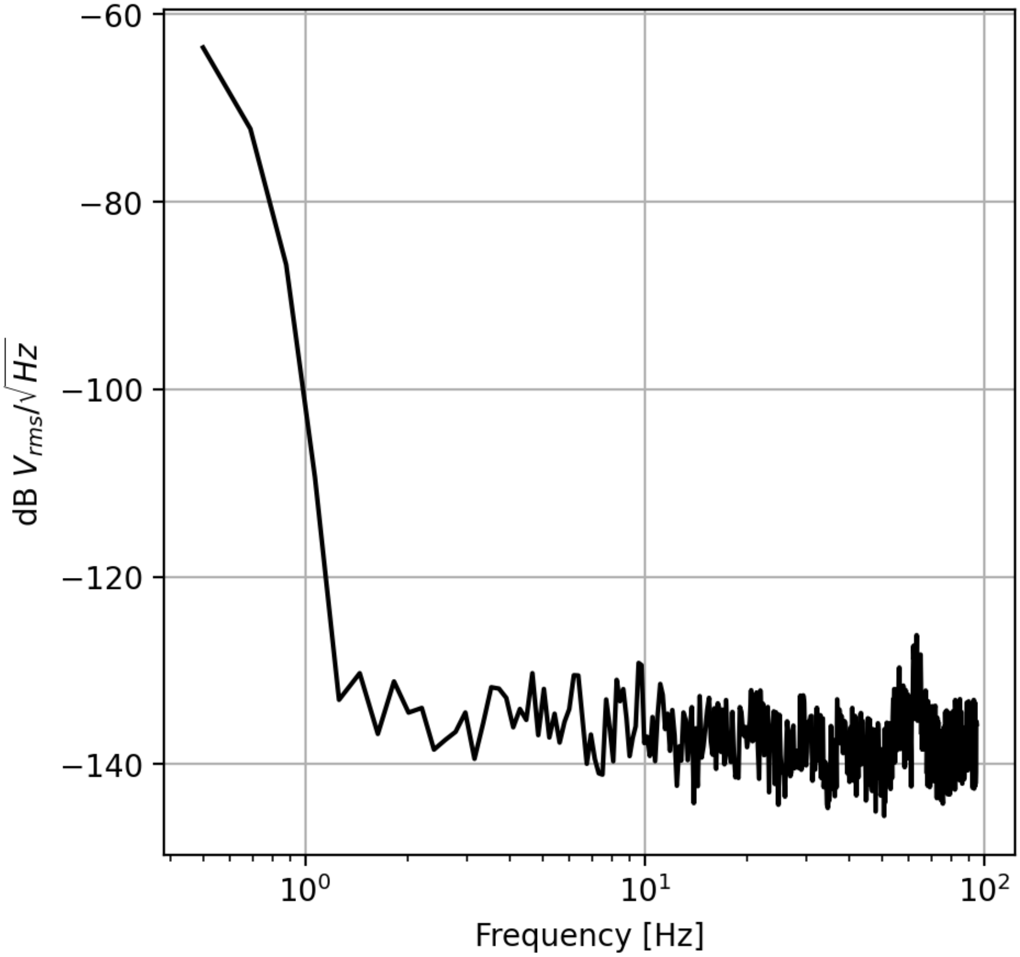

Figure 3.13: Voltage noise spectrum of the calibration battery box in static signal output mode. The data has been acquired using a HP 3563A signal analyzer. The X axis is frequency and the Y axis is decibels referred to a $1V_{rms}$. The -140 $V_{rms}/\sqrt{Hz}$ level correspond to a noise of 0.141 μV_{rms}. Applying this bias to a 0.1 Ω resistor (such as the heater design), through 100 $k\Omega$ of current limiting bias resistor would result in a noise of 1.4 $aW/\sqrt{Hz}$ or $1.4 \cdot 10^{-18} W/\sqrt{Hz}$ which is well below the target noise of 20 $aW/\sqrt{Hz}$. This instrument is suitable for biasing the TKIDs for device noise exploration.

lines; each side of the cryoflex has a Gold-plated Copper splitter interface that allows for coaxial SMA connections and easy mounting and thermalization on the cryostat hardware. The RF lines exit the thermalization plate and run on a flexible Kapton-like tape that is 1/4 inch wide until they re-enter another thermalization plate with connectors. These microstrip-based products, specifically the CryoFlex 3 product line [80], allowed us to modify the cryogenic configuration of the line and the thermalization interfaces without having to deal with fixed coaxial cables. The problem with fixed cryogenic coaxial cables is that changing the bend will significantly degrade the performance once they are bent in a specific shape. Furthermore, cryogenic coax cables require pass-through clearances that are not always available in a cryostat designed for a TDM architecture. These cables enable the whole readout chain to be implanted in a non-predisposed cryostat with minimal effort.

The Cryoflex cable runs from 300 K to the 4 K stage and is thermalized at 50 K. 4x lines on the cryoflex cable are used for transmitting the signal, while the other four will carry the return signal. Between the interfaces of the two Cryoflex cables sitting at 4 K, we attenuate the signal and the noise by 20 dB. The second Cryoflex cable runs from 4 K to the UC stage, and mechanical thermalization is realized at 1 K using custom-machined hardware. The thermal load of the RF cabling is well in line with the calculator software available at [80]. In our tests, we notice that the presence of the Cryoflex bundles in the configuration just reported does not significantly affect the 50 K and the 4 K stage temperatures; the UC stage temperature is affected by the presence of the Cryoflex with a 20 mK increase in dark configuration (250->270 mK base temperature) and 30mK increase in optical configuration (300->330 mK base temperature). The temperature increase is primarily due to the active load introduced by the power dissipation of 4x LNAs, model CITLF2 [81, 82]. After attenuating the noise and the signal again at 20dB at the UC stage, we are guaranteed that the base (off-resonance) noise is the lowest possible at 0.3 K: -203.8 $dBm/\sqrt{Hz}$. At this point, the probe tone interacts with the detectors: the UC attenuators are mounted directly on the Cryoflex harness for practicality. Coaxial isothermal copper cables connect the attenuators with the FPU signal distribution board for transmission and reception. The signal exits the FPU PCB and reaches the 4 K amplification stage through the same bundle. While the physical proximity of the transmit and return signal introduces some crosstalk, our measure determined that the crosstalk level, -40dB at maximum, does not interfere with our measures. The 4 K LNAs, the attenuator, and the custom-made power distribution board for the LNAs are mounted inside a custom-designed metal enclosure. This enclosure, visible in Figure 3.15, serves two purposes: avoid radiative heat coming from the LNAs to couple directly with the Helium evaporators of the sorption fridge, ensuring that the acoustic cryocooler dissipates as much heat as possible from the LNAs; allows easy transport of the chain's core components in case of deployment in a different cryostat. The specific LNA we use to amplify our signal will ultimately determine the RF SNR we will deal with at room temperature. We measure the noise temperature of the amplifiers to be 6 K. The diagram in Figure 3.14 account for that in the calculation of the final SNR. Getting out of the cryostat we filter the signal again to avoid spurs pickup in the line connecting the cryostat with the instrument rack and amplify the signal again with room temperature low noise amplifiers to match the power level expected by the receiver side of the SDR. The final SNR we obtain with -95 $dBm/\sqrt{Hz}/resonator$ should be -102 $dBc/\sqrt{Hz}/resonator$ but it is limited to $\sim$ -98 $dBm/\sqrt{Hz}/resonator$ @ 1 Hz by the performances of the SDR we are using, a N321 from Ettus Research [83] in shared local oscillator configuration (see section 3.4 and next subsection).

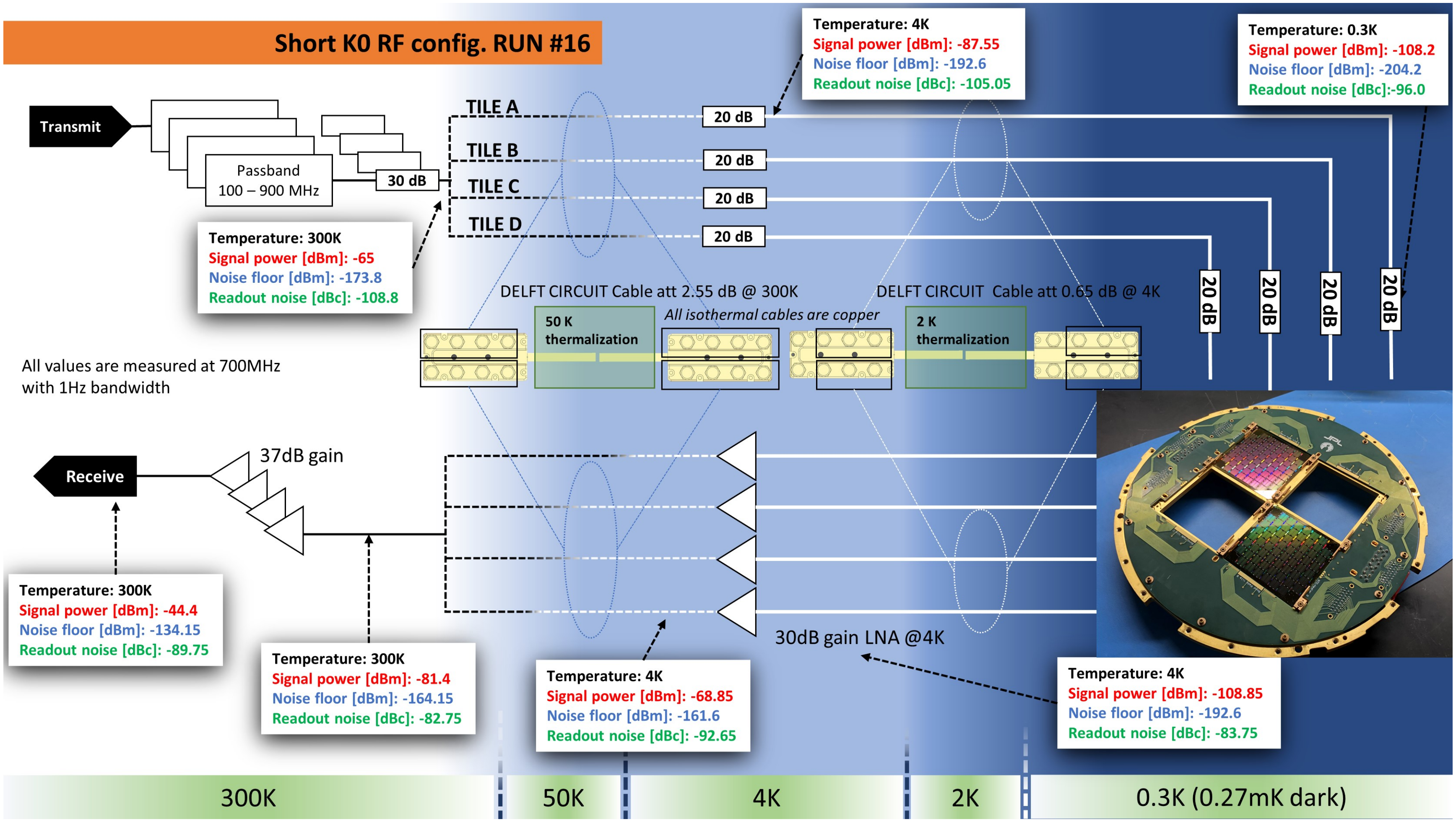

Figure 3.14: Example of a diagram used to record the run configuration. The bottom green bar divides the diagram in thermal zones, each withe line represent an RF transmission line. The white boxes keeps track of the expected noise at different stages. The black transit and receive blocks are the ADC/DAC interface of the SDR. The central cable schematic reports the measured attenuation of the cryogenic RF lines. The first set of triangular blocks, at 4 K, stands for 4x CITLF2 cryogenic LNAs. The room temperature set of amplifiers is described under Romm temperature electronics. This specific run was the first one with two different tiles on the focal plane. While all the RF lines arrive at the FPU, only two are connected. The remaining lines are either used in loopback configuration for diagnostic or connected to a prototype TKIDs chip installed under the UC stage as reference noise sample.

Room temperature electronics

This subsection focuses on the room temperature electronics used to read out the detectors. The main hardware platform that enabled the readout of TKIDs are the Ettus Research SDR radio from the X series and N series. Initially we started developing our readout infrastructure around the SDR model X300. This specific platform enabled us to stream a baseband of 200 MHz toward and from the devices through a 14-bit DAC and ADC. The X300 has two sets of full-duplex interfaces, customizable via daughter-cards. A daughter-card allows the user to filter, up-mix and down-mix the baseband signal with a signal generated by embedded voltage controlled oscillators, VCOs, realizing a superheterodyne transmit/receive architecture. The target frequency range external to the SDR (the RF range in which the resonators are, 700MHz for TKIDs) is determined by the VCOs internal to the daughter-card and programmatically controlled via interaction with the internal FPGA's firmware. Critically, the transmit and receive signal path use two different VCOs for upmix and downmix operations. The problem with using two independent oscillators is that the low frequency noise in the carrier phase and the long term stability of the carrier frequency are affected by two independent components. In an effort to reduce the RF chain noise we switched to the newer N321 platform, more similar in concept to a modern RFsOC but still utilizing a superhet architecture for carrier modulation. The main advantage of the N321 platform for our program was the flexibility exposed by a configurable local oscillators (LOs) signal path. Specifically, the possibility of using the same LO signal for receive and transmit operations. After successfully demonstrating the improvement to the noise introduced by this new platform, see Figure 3.16, we selected it as the main readout front-end for most of our experiments at Caltech and at JPL Luckily for us the heterogeneous software suite developed for the program, see section 3.4, was flexible enough to require minimum effort to switch platform.

The rest of the room temperature electronics is composed by commercial RF components widely available for off-the-shelf procurement. Because the aim of this goal is to have a deployable package, amplifiers, filters, attenuators, and relative power supplies have been condensed in a custom 3U rackmount enclosure. The enclosure, we will call it the RF box, contains all the hardware necessary to interface the cryogenic readout chain with the SDR platform. The N321 comes with embedded filter and amplification on both the RX and TX side. While this may mean that the RF box can be bypassed on paper, the filters and the amplifiers contained in the RF box are considerably more performant respect to the embedded version on the

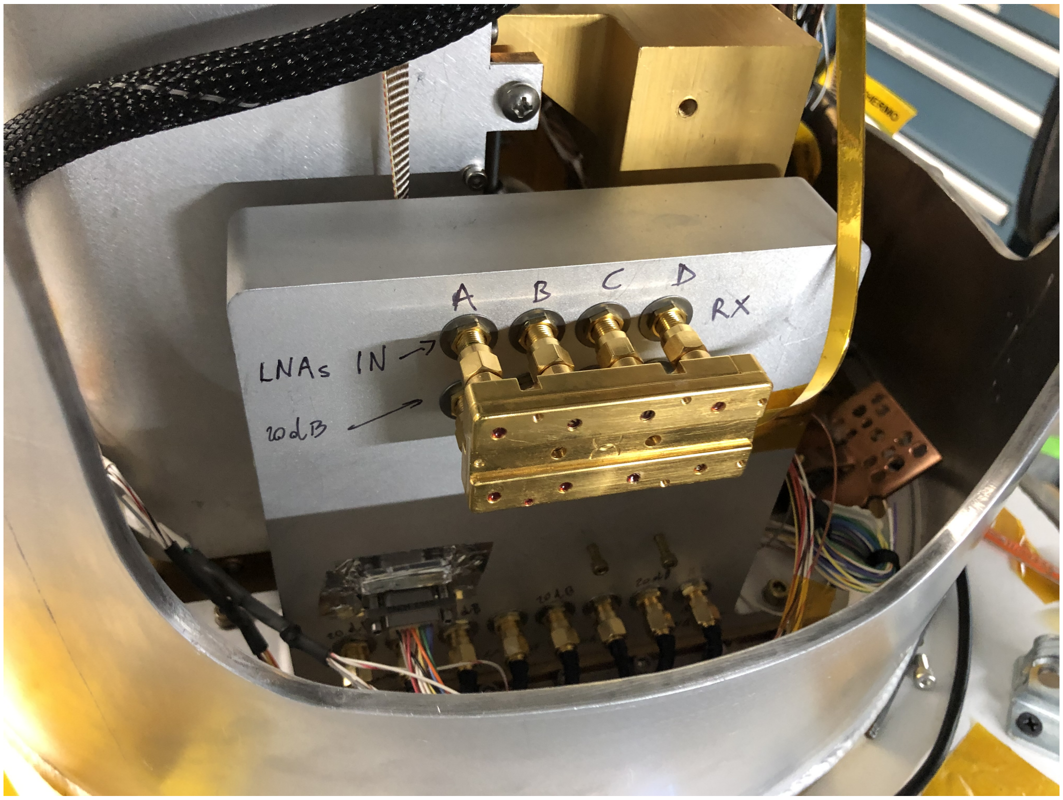

Figure 3.15: Picture of the 4 K stage durning the assembly phase of sK0. The large cylindrical containter exposing the window is the 4 K shield without the copper covers (side service windows open). Inside the 4K volume we can see the Gold plated harness of the Cryflex cable connecting the 4 K stage to the UC stage as well as its ribbon. The harness is attached to a custom machined Aluminum enclosure. The enclosure is the light-tight housing of the LNAs and 4 K attenuators. Annotations are clearly readable on the surface of the box, indicating which side of the harness is used for transmission or receive operations. At the bottom of the box a micro-d connector carries the power supplies, voltage sense and diode-based themoimeter signals. Below the micro-d connector, a row of SMA isothermal cable assemblies connect the LNAs enclosure to the 4 K stage bottom plate. The black cable in the foreground is a 100 way Copper interconnection cable carying calibration signals. The gold plated structure in the background is the sorption fridge mounting bracket. The aluminum box attached to the bracket is the fridge shielding.

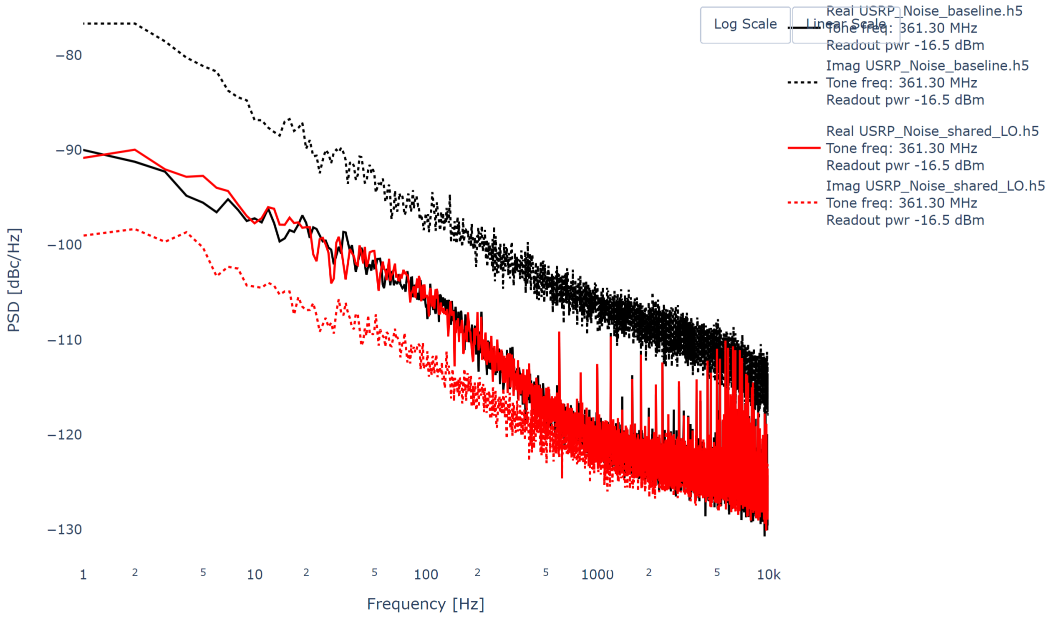

(a) Power spectrum of the power relative to carrier of two different configuration of the N321 platform: in black we use two different LOs for the transmit and receive signal mixing. In red We only generate the receiver path LO and inject it in the transmit path mixing. The noise is significantly reduced

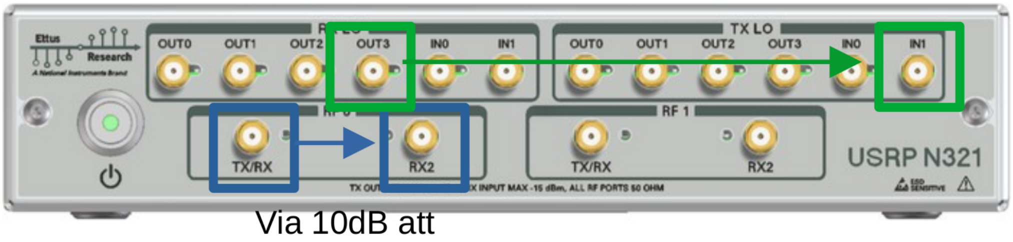

(b) Schematicc of the connections used to realized the shared LO configuration on the N321 platform

Figure 3.16: Sharing the Local Oscillators (LO) between the transmit and the receiver path reduces the noise associated with the carrier frequency instability and phase noise. Figure **a** reports a direct comparison of power spectra relative to the carirer in loopback configuration (TX -> passive attenuator -> RX). Figure **b** reports on the configuiration used to realize the LO sharing (API control needed, hardware connections are NOT sufficient to replicate) and loopback configuration.

N321. While the difference in noise performance is difficult to quantify, in more than one occasion the RF box was instrumental for the success of the test. A notable, recurring problem that the RF box handles is the interference of WiFi, Bluetooth and cellular signal with our measurements. Furthermore, the input power levels of signals coming from and to the cryostat can be set via different amplifiers and attenuators and the logistic of the deployment reduces to the movement of a single, AC powered, instrument. The RF box, internal view reported in Figure 3.17, can be powered by both a 110V or 220V 50/60 Hz elecrical line via three-prong panel connector. The AC is filtered with a passband filter and distributed to two linear, thermally compensated, PCB mounted power supplies unit from Acopian. The first power supply generates 12 V and powers the amplifiers, the current meter and two fans for air circulation. The second power supply provides 3.5 V, monitored by the current meter, used to power the LNAs inside the cryostat. Filters, and amplifiers are mounted on a aluminum sheet-metal frame and interconnected by double shielded SMA cable assemblies. The specific models of amplifier and filtering used cycled between different configurations with the evolution of our readout platforms and techniques but remained coherent around the following principle: the receive line takes in input the signal from the cryostat and has a passband filter and a low noise (NF<3) amplifier, output the signal to the receiver port of the SDR; the transmit path takes in input the trasmit port of the SDR and has an attenuator to target the right power-on-chip range and a passband filter. This structure is replicated four times, once per each TKIDs tile. The front panel exposes a display for the LNA ammeter, 4 isolated SMAs per tile and a general disconnect switch to turn off the box main power.

Focal pane unit board

The focal plane distribution board interfaces the silicon TKIDs tiles and the readout infrastructure. The mechanical support of the tiles, as well as most of the shape of the FPU PCB, is inherited by the previous deployment of the Keck receiver. We repurpose the available signal paths within this framework to accommodate the newly introduced RF scheme and a calibration signal network. The TDM architecture of a Keck cryostat envisions 6x 37-way micro-D connectors interfacing the non-isothermal cables (J-cables) with the tile-boded pads on the PCB. We recycle this concept and reuse the connectors to distribute our calibration signals to 4 TKIDs tiles. At the same time, we reposition every element of the board to make space for 8x SMA connectors. The shape and cut-out of the board are fixed parameters

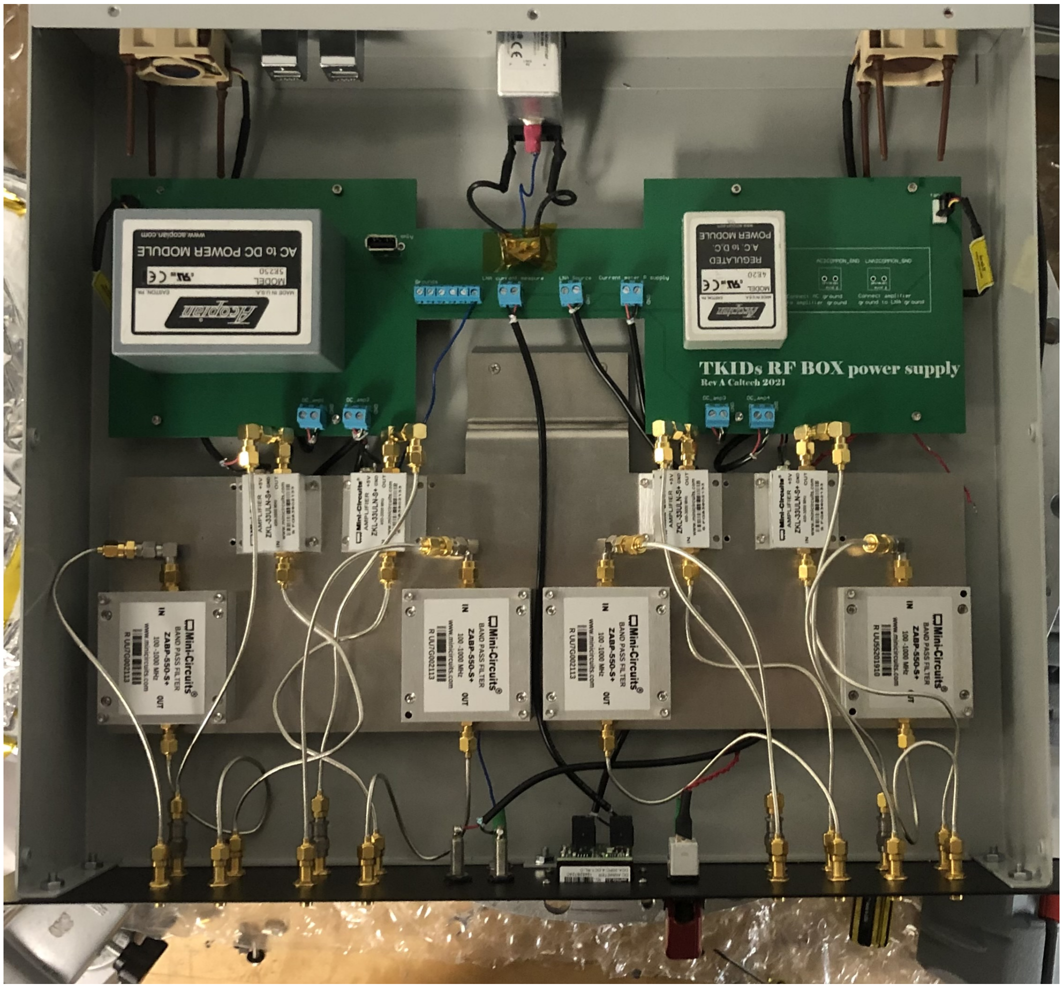

Figure 3.17: Top view of the internal components of the RF box. The box is meant to be a practical and self-contained way to manage the interface between the SDR platform and the cryostat. From the top we can see the main line filter, the two fans, the power supply board, the filters and amplifiers mounted on the aluminum frame and connection to the front panel.

given by FPU compatibility with Keck infrastructure (we envisioned the possibility of deploying with only FPU and readout chain). We use the board's topology to isolate the RF and calibration signal paths as much as possible. Once again, we interleave each signal layer with a double Copper weight ground layer, naturally forming the RF stripline morphology in the internal layers. We reserve the top layer for the calibration signals and use the internal layers for RF transmission. To achieve a rapid prototyping cycle, we engineer the microstrip dimensions around standard Rogers Corporation (series 4000) materials [84] that can easily be procured by fabrication facilities. Avoiding the impedance matching of fab facilities resulted in fundamental as the material characterization used for the process changes drastically

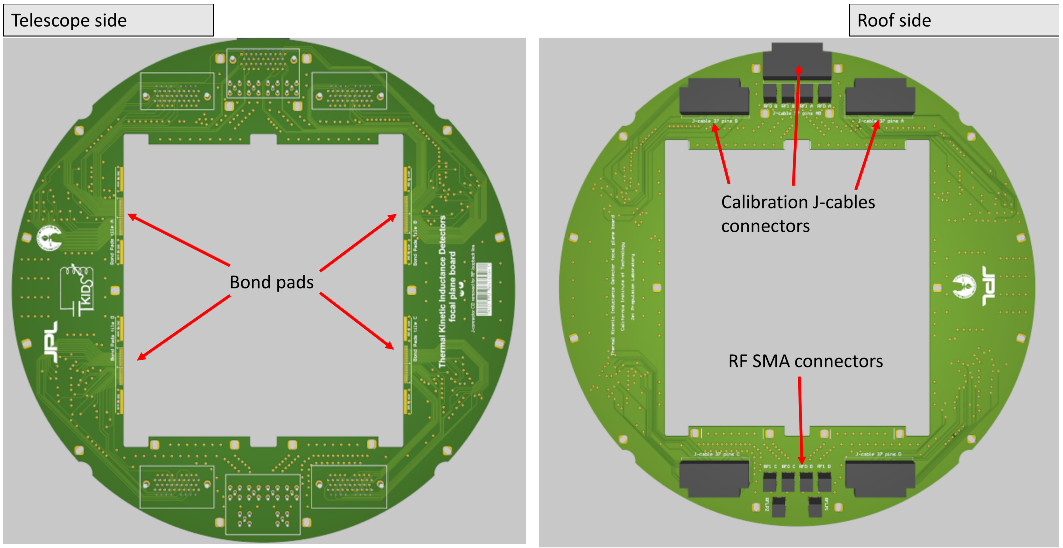

Figure 3.18: 3D rendering of the FPU signal distribution board. On the left, the side pointing toward the cryostat is rendered. The soft Gold plated bondpands for the tile assembly are visible. On the right side the layer of the PCB that should have pointed to the sky is rendered. The black boxes on the panel are placeholders representing the mechanical clearances of the various connectors. We can note on this specific version the absence of one of the six micro-d. The connector removed specifically carried redundant diagnostic information used exclusively during the material characterization phase of the project. The micro-d connector has been replaced by two additional SMA RF connectors for loopback testing of the board.

when considering cryogenic temperatures [85]. The final dimensioning of the RF stripline has been performed using the embedded calculator in Altium and modified material models. Alternative processes and materials (Rogers 5880) have been explored but quickly abandoned, given the project's finite lead time and resources. The resulting PCB, design available in Figure 3.18 and visible throughout this work, has been tested in a liquid Nitrogen bath, the single path attenuation (excluding cable, including connector), is 0.8 dB between 200 MHz and 1 GHz. The test has been performed on a different design in the PCB production panel, where two paths were shorted together bypassing the tile wirebond while retaining the overall geometry.

3.4 Fixed tones readout

The most straightforward way to extract signal from KIDs has always been using probe tones modulated by the detector-coupled device S_{21} [86]. We call this method fixed tones readout because once the power and frequency of the probe tones are set, they will not change for the whole measurement duration. This method has no feedback mechanism in place. Our implementation of the fixed tone method [87] predates the beginning of my work at Caltech. I started developing the readout system as an engineer at JPL to fulfill the needs for a flexible, cheap, and scalable readout system in various labs with very different desiderata [88]. In 2019, I created a fork on the software versioning [89] to maintain the software. This section focuses on the functionalities and selected internal details of the software suite called GPU_SDR. The idea behind GPU_SDR was to offload all the computations necessary to modulate and demodulate the probe tones on a GPU unit.

General purpose use of GPUs (we chose Nvidia GPUs for the availability of the programming documentation) units was already well established and the underlying programming language, CUDA, was developed enough that programming a kernel (code that runs on a GPU) was a significantly simpler task than programming an FPGA. At the same time, Ettus Research and other companies commercialized software Defined Radios sporting $\sim$ 200MHz of full-duplex bandwidth and reaching various RF bands via superhet techniques. The maturity of these SDRs' stock firmware and the API (Application Programming Interface) enabled the possibility of moving the full duplex band out of the FPGA space for processing via optical fiber on an adequately equipped computer. On the computer side, the PCIe bus, used for GPU-CPU data transfers, evolved so that a single machine could process data from multiple SDR frontends. GPU_SDR utilized the stock firmware on the Ettus platform via the C++ UHD API to program the SDR hardware parameters and stream the baseband data. Once the data is in the machine's RAM (called the server), it gets transferred to the GPU memory for processing and back to the CPU space for post-processing. Post-processing involves eventual triggering and the stream of the processed data to a secondary machine (called the client) that connects to a few network sockets to control the server. Separating client/server machines via network is necessary and proper for various reasons. First, the processes running on the server and interfacing with the FPGA must be run in real time. The effect of the scheduler provoking a context-switching event on a stream-handler process is the loss of data. While the memory on board the server and the GPU allows some flexibility in the processing delay, the buffers on the FPGA are less deep and saturate quickly with the delay introduced by a non-real-time process. While core affinity and priority scheduling alleviate the risk of contest switching, an adequately compiled real-time Linux kernel could not be used as it is not generally compatible with the Nvidia CUDA driver, and the overhead introduced would have been challenging to manage [90]. The final form of the GPU_SDR system operates on the following hardware:

- Ettus SDR: all the software defined radios compatible with the UHD API will work in a plug-and-play fashon with the system. The UHD API developed functional network discovery protocols that are hardware agnostic. Generally speaking, for the purpose of explaining this spercific system, the SDR can be seen as an FPGA connected to a DAC/ADC and a radio. The firmware on-board the FPGA communicates with the C++ API on trhe server computer via network. The system uses the stock firmware of each platform and does not require the user to interact with the underlying transport layer. That said, there is quite a bit of data processing happening on the FPGA. The stock firmware offers the possibility to reduce the baseband via FIR-based downsampling and perform direct up/down conversion operations using a CORDIC based RFnOC block.
- Networking: The data from the FPGA is streamed via optical fiber to and from the GPU server. The specific connection depends on the SDR model used and ranges from a 10Gbit fiber terminating in SFP+ connectors to a 40Gbit fiber terminating in a QSFP. For the purpose of testing the scalability of the system, a multi interface packet broker from Niagara networks was successfully used as a buffer interface between the SDRs and the GPU server. The endpoint on the GPU server has historically been a XL710 Networking chip from Intel but Mellanox connect-X (series 4/5) interfaces have been tested to work as well.
- GPU Server machine: The GPU server runs a program that uses the UHD API from Ettus and the CUDA runtime API from Nvidia to move data from the FPGA to the GPU and vice-versa. The way we approached the data transport in the server programs has been the instantiation of a finite number of data structures containing an initialized pointer to a data buffer and an expandable number of metadata, ranging from packet numbering to timestamps to processing stage and flow control logic. We will call this structure the buffer wrapper. Buffer wrappers are allocated at the beginning og the server pro-

gram executions in a number sufficient to buffer an eventual processing time jittering. A memory controller class manages a lockfree queue of pointers to all the allocated data structures. Once a new buffer is received from the FPGA, a buffer wrapper pointer is popped from the queue. The metadata field is populated and the internal buffer pointer is assigned to the incomiung data. The pointer to the buffer wrapper is then moved across the various stage of processing until the data is streamed to the client machine via network. At that point the buffer wrapper is stripped from metadata and pushed in the same queue managed by the memory controller object. This logic is replicated for outgoing packets. The principle behind moving only pointers to pre-allocated memory buffers is that avoiding memory allocation overhead time helps in managing the timing of realtime applications. This is especially true when the memory allocation is not a simple malloc call but a "pinned" memory allocation used to speed up the GPU transfert.

- GPU: While some triggering logic and data manipulation happens in the C++ code that runs on the CPU of the server, most of the data processing happens on the GPU. We upload the data from the FPGA to the GPU via asynchronous PCIe data transfer calls. The asynchronicity makes possible the overlap of data transfer and data processing from the previous buffer. The coherence of data transfer and kernel execution is managed via "CUDA streams" that essentially are queues of operations. The concept of streams allows us to use a single GPU to process incoming data from multiple frontends, and possibly SDRs, at the same time. Conversely, using streams to pipeline the processing operations allows the use of multiple GPUs to process data incoming from a single frontend. A more specific description of the algorithms running on the GPU will follow in the next subsection.
- Client/server networking: The server machine ultimately streams the data to a different machine on the same network, called the client machine. The client machines uses a Python API to connect to the server and exchange data. Specifically the server exposes a UDP socket for raw data streaming and a TCP socket for receiving instruction from the Python API and sending back diagnostic and service information.
- The Python client: The client machine operates a Python API to control the system and receive the data. Once the Python API connects to both the UDP and TCP socket of the server, functions for starting various kind

of measurements with the system are exposed. Once a measurement starts, the Python API takes care of accumulating data and metadata in a HDF5 [91] file format for storage further analysis. A vast and very specialised data analysis and plotting suite is also attached to the Python API. While we will not discuss nor document the full list of functionalities of the API in this thesis for practical reasons, a detailed documentation, complete with examples and a quickstart guide is available at [89].

GPU Kernels: Demodulators

The direct demodulator consists in a kernel that given a buffer containing a comb of tones, shift each tone at DC and performs low-pass filtering and decimation operations. The output of the direct demodulation kernel is a series of buffers where each buffer corresponds to the reduced complex timestream of a demodulated tone. The concept of demodulation is the following. Suppose you transmit a signal $S(t)$ so that:

$$S(t) = \sum_i A_i e^{j\omega_i t} \tag{3.1}$$

where A_i is the amplitude and initial phase of each transmitted tone ω_i is the frequency of each resonator. After the interaction with the resonator array we have a new signal $\hat{S}(t)$ so that:

$$\hat{S}(t) = \sum_i \hat{A}_i(t) \cdot e^{j\omega_i t} \tag{3.2}$$

where now $\hat{A}_i(t)$ is the modulation introduced by the local S_{21} variation of each resonator. In other words, $\hat{A}_i(t)$ is the signal of our detectors. In order to recover it we can do the following:

$$\hat{A}_i(t) = \hat{S}(t) \cdot e^{-j\omega_i t}. \tag{3.3}$$

Now we have the signal $\hat{A}_i(t)$ at DC and the rest of the tones $i \neq j$ moved around in the frequency space. Low pass filtering $\hat{A}_i(t)$ obtained in this way with a cutoff frequency that excludes the other demodulation products isolate the signal of a single probe tone. Successively, a reduction operation is performed to reduce the amount of data flowing in the application. The result is a complex timestream $\hat{A}_i(\hat{t})$ per eacxh detector, where $\hat{t}$ is proper to the new rate of the signal. Our specific implementation fuses the low-pass filtering and decimation in a FIR filter kernel implemented via the CUDA version of linear algebra operation library (CUBLAS). This method is very straightforward and allows in theory to read a detector out with the whole hardware bandwidth, very usefull if one wants to trigger on fast signals.

Luckily for us, the fact that the sensitive element of TKIDs is suspended on an island, limits the amount of material sensitive to cosmic ray interactions and thus we can move to better demodulation topologies, like the polyphase filterbank, without the need for any fast triggering. The problem with tqhe direct demodulator is that the demodulation operation must happen at the undecimated rate. This means that the memory bandwidth requirement grows linearly with the number of detectors. We have found that a Nvidia GTX 1080 Ti with GDDR5x memory can demodulate ~ 30 tones from a single SDR frontend running at 250 Msps. The polyphase filter bank (PFB) kernel allows for the same operations but, because of its efficient operation order, allows for ~ 200 channels per GPU.

GPU Kernels: VNA

One of the functionality needed to operate a fixed tones readout scheme is to locate and characterize the resonators in the frequency space. The dedicated instrument for this purpose is the Virtual Network Analyzer (VNA). A 2-port VNA typically measure the complex $S_{21}(f)$ of the device under test. The way we implement this instrument using the GPU_SDR system id to provide the transmit DAC with a continuous chirp signal where the frequency is moved in step. The same chirp signal is used on the receive side for the demodulation. Generating the signal in real time allows the parameter space of VNA scan to be arbitrarily big as we do not need to constrain the duration of the transmission with the length of a buffer. The probe signal $S(t)$ is generated onboard the GPU as:

$$S(t) = Ae^{-j\phi(t)} \qquad \phi(t) = 2\pi(f_0 t + kt^2) \tag{3.4}$$

where $\phi(t)$ is the phase of the probe signal, f_0 is the initial frequency of the chirp, t is a discrete time interval given by the DAC rate and k is the ramp rate or chirpness parameter, controlling the frequency increase of the chirp signal. As an example of kernel development I'm going to report in following listing. The kernel used to generate the packets for the VNA functionality.

```
__global__ void chirp_gen(

    float2* __restrict__ output,        //Pointer to the gpu buffer
    unsigned int output_size,           //Size of the buffer
    chirp_parameter* __restrict__ info, //Chirp metadata struct
    unsigned long int last_index,       //From last buffer
    float scale = 1                     //Scale the amplitude of the chirp

    ){
    //index relative to the current position
    //in signal generation (a single chirp may
    //be generated in more than one kernel call).
    unsigned long int effective_index;

    //actual frequency step in the chirp generation.
    unsigned long int frequency_index;

    //phase correction to allow parallel
    //coherent phase generation.
    unsigned long int phase_correction;

    //index to use in sinus and cosinus.
    int index;

    // Monolithic kernel design
    for(unsigned int offset = blockIdx.x * blockDim.x + threadIdx.x;
                offset < output_size;
                offset += gridDim.x*blockDim.x
        ){

        //take in account previous calls and bookeep phase
        effective_index =
        (last_index + offset) % (info->num_steps * info->length);

        //calculate current frequency to generate
        frequency_index = effective_index/info->length;

        unsigned long int q_phase =
        (frequency_index/2)*(frequency_index +1) +
        (frequency_index % 2)*((frequency_index +1)/2);

        //correct the phase.
        //needed for parallel chirp generation.
```

```
        phase_correction =
        ( info->chirpness * (info->length * q_phase) );

        //evaluate sine index
        index = effective_index *
        (info->f0 + frequency_index * info->chirpness )
        - phase_correction;

        output[offset].x = sinpi(((double)(index)/2147483647.5))*scale;
        output[offset].y = -cospi(((double)(index)/2147483647.5))*scale;
    }
}
```

Listing 3.1: Chirp generation GPU Kernel. This listing reports an example of CUDA programming. While the code has the same syntax of a C++ function, the code gets compiled in instructions executed by thousends of processing cores at once. The parallelization happens in the for loop structure. blockIdx.x is the core index, blockDim.x is the number of available core in a processing unit (group of processing cores) and threadIdx.x is the number of the processing unit.

A call to this kernel will populate a transmission buffer with samples from the specified chirp waveform. The demodulation Kernel generates the chirp waveform with the same parameters and demodulates the incoming packet into a DC signal. The chirp waveform will not necessairily increase in frequency at every sample. The kernel uses an "effective_index" variable that makes the chirp frequency linger for a set amount of time at every advancement interval. The variable "effective_index" effectively determines the IF bandwidth of each VNA point. The raw demodulation product then gets averaged down with a window synchronous with the frequency steps of the chirp waveform. The data accumulation results in a single comples S_{21} complex number per frequency step. The demodulation of course must take into the account the delay introduced by FPGA initialization time and equivalent length of the measured RF line. The delay is estimated before the VNA acquisition and compensated on the FPGA with a delay counter.

Resonant frequency reconstruction

Having the VNA and the fixed tone functionality defined by software and running on the same physical instrument allows us to perform a direct comparison between a narrow-band VNA scan of a single resonator and the noise acquisition the resonator itself. In Figure 3.19 show a classic diagnostic plot of noise acquisition. The coincidence of the VNA trace and the noise acquisition indicates a few things:

- The main structure of the S_{21} measured in the VNA is consistent with the average of the noise acquisition.
- The time and power spent characterizing the TKIDs device with the VNA are adeguate.
- No significant temperature shift is happening to the island.
- The setting of the system are consistent between the VNA and noise acquisition phases.

The last item above is significant because the properties of TKIDs devices can change significantly with the readout power [43] and the frequency offset of the probe tone [92] respect to the resonant frequency of the resonator.

The VNA acquisition data is fitted with the function reported in equation 2.8, the quality factors and the resonant frequency are extracted from the fit. File-wise, the VNA HDF5 file and the noise timestream HDF5 file are both tagged with attributes reporting the results of the fit per each resonator for long term data retention. We now need to transform $I(t), Q(t) \Rightarrow, Q_r(t)$ where $Q_r(t)$ is a total quality factor timesteam and $f_0(t)$ is the resonant frequency timetream. For this purpose (and to use the same notation of Gao's thesis [59]) let us consider a slightly modified verison of S_21 that includes a phasor, describing the cable delay.

$$S_{21} = A\exp(i\omega\Delta t)\left(1 - \frac{Q_r}{Q_c}\frac{1}{1+2iQ_r x}\right) \tag{3.5}$$

Then we take noise data at some frequency, and want to know what the resonator frequency timestream is based on the noise data. First, remove the amplitude scaling and time delay and subtract $1 - Q\_r/2Q\_c$ to recenter the resonator circle about the origin. The centered resonator function S_{21}^c is now:

$$S_{21}^c = -\frac{2Q_c}{Q_r}\left(\frac{S_{21}}{A\exp(i\omega\Delta t)} - 1 + \frac{Q_r}{2Q_c}\right) = \frac{1-2iQ_r x}{1+2iQ_r x}. \tag{3.6}$$

Because the resonator is now a (partial) unitary circle around the origin, we can rewrite it using the angle of an inscribed triangle θ as $\exp(i\theta) = 1 + 2iQ_r x$ so that S_{21}^c becomes simply $S_{21}^c = e^{-2i\theta}$ and the circle has angle $\theta(t) = -\mathrm{Arg}[S_{21}^c(t)]/2$.

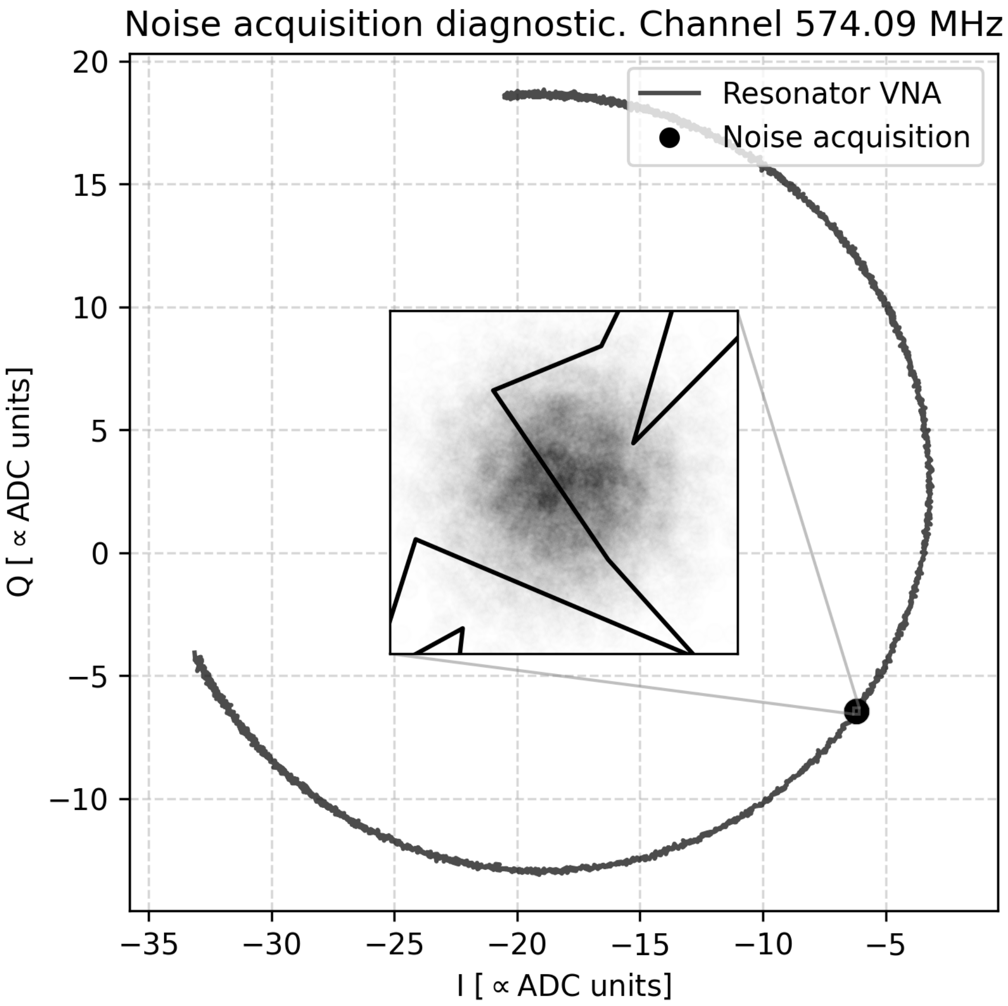

Figure 3.19: Diagnostic plot from the GPU_SDR system. The X and Y axis define a complex plane on which our S_{21} is defined. The units are equal between X and Y and proportional to the DAC and ADC units. The circle in the plot is the result of a VNA scan around a resonator. In this case the VNA scan has a bandwidth of 1 MHz around a resonator with f_0 sitting at 574.09 MHz. The IQ values from the VNA scan are plotted in the IQ space and result in the resonator circle. The two end of the circle represent the most off-resonance frequency scanned with the VNA. The point opposed to the circle aperture, close to f_0 is our readout point of choice because it maximizes the derivative of the S_{21} in the tangential direction. Once the readout frequency is set, we stream and demodulate a probe tone at that frequency. The resulting complex I/Q timestream is plotted as markers on the I/Q plane. A zoom in visible in the plot expose the overlap between the noise measurement and the VNA scan.

Frequency and quality factor timestreams can be obtained using some trigonometry as:

$$x(t) = \frac{1}{2Q_r}\tan(-Arg[S^c_{21}(t)]/2) \tag{3.7}$$

$$Q_r(t) = Q_r|S^c_{21}(t)|. \tag{3.8}$$

In our analysis the $Q_r(t)$ timesteam is only used as a check for measures quality control (we expect constant quality factor for small changes in T_i). The main signal we use is the resonant frequency timestream which would correspond to a tangential movement of the noise along the VNA trace in Figure 3.19. The GPU_SDR integrates functions that calculate the tranformed timestreams and store them alongside the raw data in the same file.

3.5 Fastchirp readout

Our TKIDs arrays are explicitly developed to operate at a load of 6pW of incident radiation with a bandwidth of 25% around 150 GHz and a thermal bath temperature of 300mK. Replicating these conditions in a laboratory environment is not only challenging but sometimes out of the scope of our research; for example, realizing a 150GHz, 6pW chopped source moving on an XY stage outside the cryostat. The load mismatch between a deployment environment and a laboratory environment is a well-known problem. TESs developed for the same scientific application have developed a double transition design [4] to overcome the challenge. In the case of TKIDs, a load significantly higher than the device specifications results in the resonators being over-coupled with the transmission line. Over-coupled resonators change the transmission function of the line significantly less in both phase and magnitude and, at the same time, exhibit an increased responsivity. These conditions make the traditional fixed tone readout [87] not an effective tool to optically characterize TKIDs in a laboratory environment. The main problem using the fixed tones readout consists of the resonators moving many linewidths away from the readout tone due to the sharp changes in load in laboratory tests, for example, the change in resonant frequency in Figure 4.10. Also, from Figure 4.10, we can see that it is not uncommon for resonators to cross another resonance in the array when using pixel-specific calibration strategies. The temporary overlap of resonators makes even tone-tracking readout systems, like SMuRF [93], lose the tracking and not be usable for optical characterization tasks. The conventional technique that remains viable is to perform VNAs (Virtual Network Analysis) and extract the position of the resonator via fitting. Implementing a fast enough system to resolve a chopped source via VNA scans would be impractical and slowing down the measurements

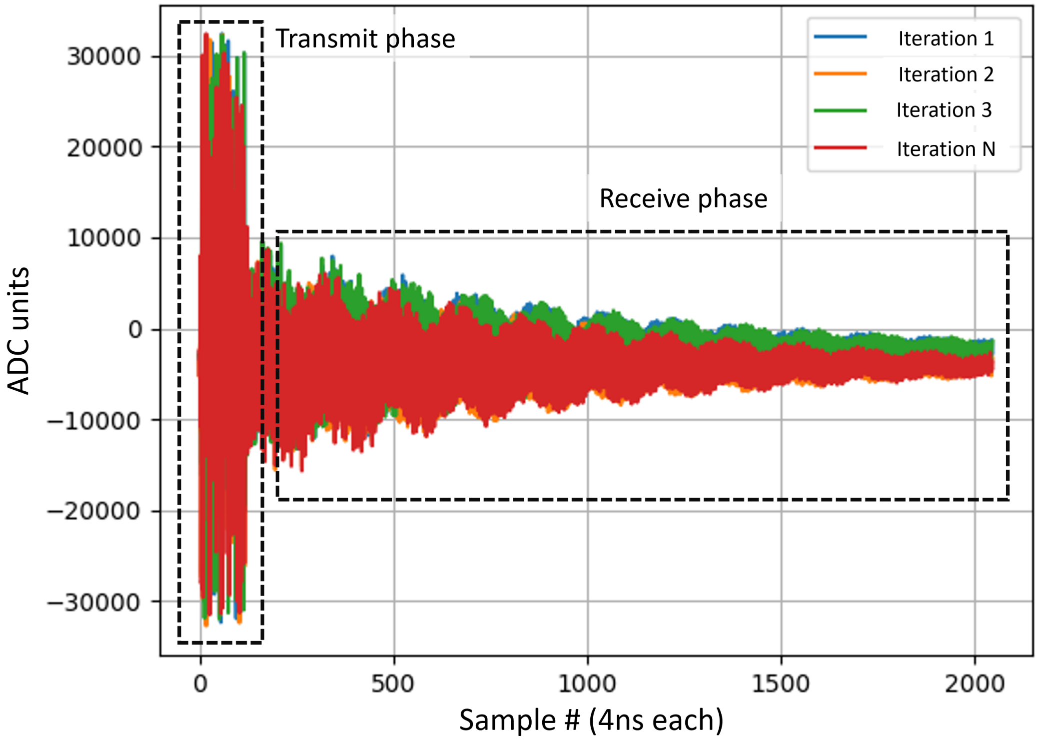

Figure 3.20: Real part of raw samples coming from a fastchirp acquisition. Each trace is an iteration of a fastchirp cycle. The fastchirp cycle is defined by a transmit (TX) phase, in which a chirp waveform is transmitted at high power across the whole available bandwidth (250MHz in this case), and a receive (RX) phase, where no signal is transmitted and the resonators' ringdown is observed. Samples in the receive phase from each iteration are synchronously accumulated and passed to the analysis pipeline, see Figure 3.21.

result in excessive measurement time and the introduction of additional systematic error.

Our solution to the characterization readout challenge was implementing a readout technique we labeled fastchirp. The fastchirp readout works by storing energy in the resonators and subsequently listening to the ringdown of the array. We implemented this readout scheme using software defined radios from Ettus Research [83] and the RFnOC framework [94]. The implementation allows us to store a very short buffer in the FPGA representing a chirp waveform spanning the whole available RF band, hence the name fastchirp. This $O(10\mu s)$ buffer is transmitted periodically (TX phase) and interleaved with a period $O(100\mu s)$ in which nothing is transmitted (RX phase), we call each TX RX phase iteration, a cycle. Charging the resonator requires the probe tone to have a significantly higher power that a classic probe tone based readout. If we used white noise or other form of wide-band stimulus

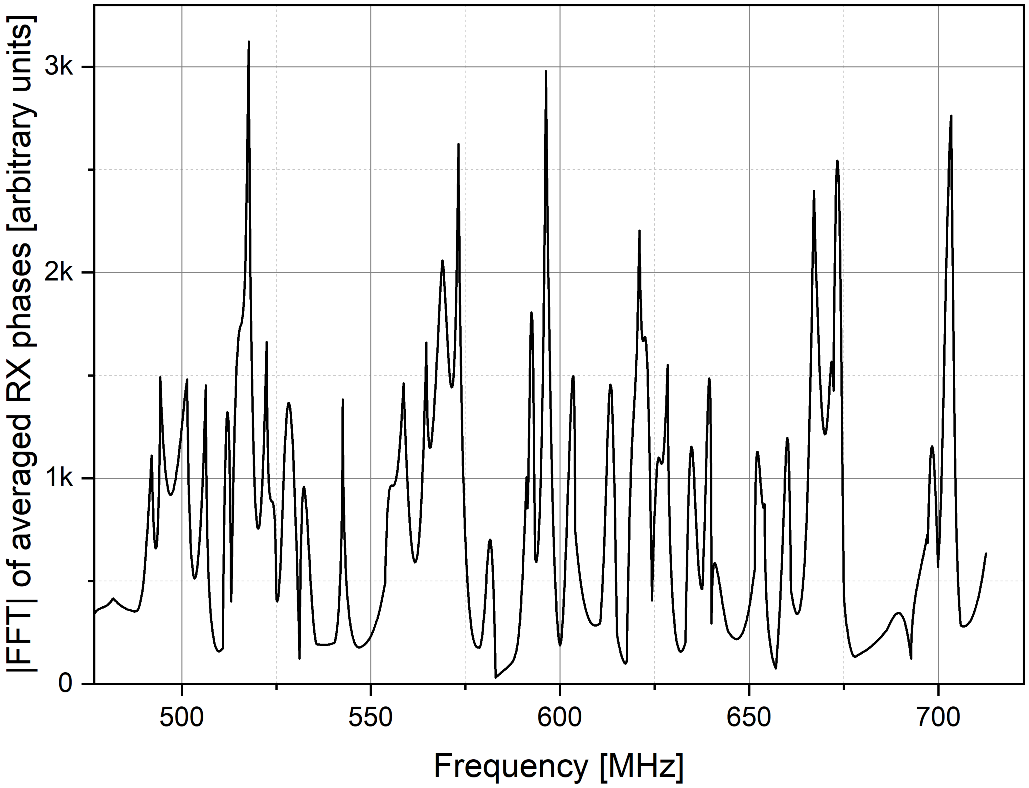

Figure 3.21: Fast chirp frame from the beam mapping pipeline this is with 500 avg and standard parameters. The black line in the plot is the magnitude of a FFT performed on 500 iteration of the RX phase described in Figure 3.20. The y axis is in arbitrary units because a scaler is used in the accumulation algorithm to avoid overflow. The falue of the scale and frequency with which it is applied are determined by the real-time nature of the acquisition. Each of the peaks visible in the plot corresponds to a resonator. By fitting the peak with a complex Lorentzian, we extract the resonator position.

to charge the array, the overall power implied would require a different cryogenic infrastructure. As seen from the ADC, iterations of the fastchirp cycle are plotted in Figure 3.20. Once each cycle is transmitted to a computer via optical fiber, the TX phase is discarded and multiple RX phases are synchronously accumulated to increase the signal to noise ratio. The result of the accumulation process is than Fourier transformed, as shown in Figure 3.21. We interpret each of the peaks present in Figure 3.21 as the energy released by a resonator and we fit each with a complex Lorentian function to extract the resonant frequency. Each transform, or frame, results in a sample per resonator. The resulting acquisition rate of the technique is, for a 250MHz complex base-band, around $1kSps$ per device.

The first few frames establish each resonator's initial position, label, or channel number. An array containing the current position of the resonators is yielded from each frame and channel numbers are matched with the previous frame by using the linear sum assignment algorithm [95], where weights are calculated using a function of the difference of resonant frequencies. In other words, in order to build a coherent time-stream per channels starting from potentially unordered resonator positions, we assume that between two frames each resonator has moved in frequency the least amount possible and we find a combination of channel and new frequencies so that the global sum of all shifts is minimized. This process is equivalent to finding the best permutation matrix P so that:

$$\min_{P}\left(Tr\left(P\times M\right)\right) \quad \text{where:} \quad M=\begin{bmatrix}\Delta_{11} & \Delta_{12} & \dots & \Delta_{1n}\\ \dots\dots & \dots\dots & \dots & \dots\dots\\ \Delta_{n1} & \Delta_{n2} & \dots & \Delta_{nn}\end{bmatrix} \quad \text{and} \quad \Delta_{nm}=F\left(f^{t0}_{ch:n}-f^{t1}_{ch:m}\right) \tag{3.9}$$

Where F is a function that prevents far away, static resonators from being exchanged, $f^{t0}_{ch:n}$ is the resonant frequency of channel n at time $t0$. The permutation matrix P is then used to sort the new frequency array and stored for further sorting. This technique allows us to track resonators across the whole RF front-end bandwidth and when they cross the frequency space of other resonators. A more detailed and rigorous description of fastchirp will be available in a separate work [96] which is currently under review.

Chapter 4

DEVICE CHARACTERIZATION

4.1 Detector characterization

In order to verify the adherence of the TKIDs design with the fabrication output and extract useful parameter for predicting the device behaviour we established cryogenic testing protocols. The following subsections are an overview of the main techniques and results.

Legs thermal conductance

The thermal conductivity of the legs suspending the TKIDs island plays a central role in modeling the device response to an optical load; see equation 2.10. In order to measure the thermal conductance of the legs, we cool down the samples in a cryostat in dark configuration (no optical load on the antennas). The dark configuration is required to use the UC stage temperature as an approximation of the island temperature, T_i: because the antennas are not exposed to a significant optical load, the island goes in thermal equilibrium with the silicon tile, and the silicon tile has a strong thermal link with the UC stage. Once we reach base temperature, the lowest achievable in the cryogenic run, we use the GPU_SDR system to acquire VNA scans of the devices while regulating the UC stage temperature at different points. We collect a VNA scan per stage temperature and extract the resonant frequency of the devices via model fitting; see Figure 4.1 for an example on a single device. The motivation for these VNA acquisitions is to build a correspondence between the island temperature and the resonant frequency of the devices, substantially calibrating the thermometric element of the bolometer over an extensive range of temperatures. We extract the f_0 parameter from the fit, see Figure 4.2, and as expected, we observe the resonant frequency dropping with temperature as more quasiparticles are generated due to phonon interaction. The quality factor and the overall depth of the device also decrease significantly with the increased island temperature. We can now build a linear interpolation function that maps resonant frequency shifts to island temperature changes, $F(f_0) \Rightarrow T_i$. Utilizing the calibration heater situated on the island, we apply a predetermined power to the island, and again, we keep track of the frequency shift of the device. In this case, we keep the stage temperature regulated at base temperature and track the frequency shift of the devices

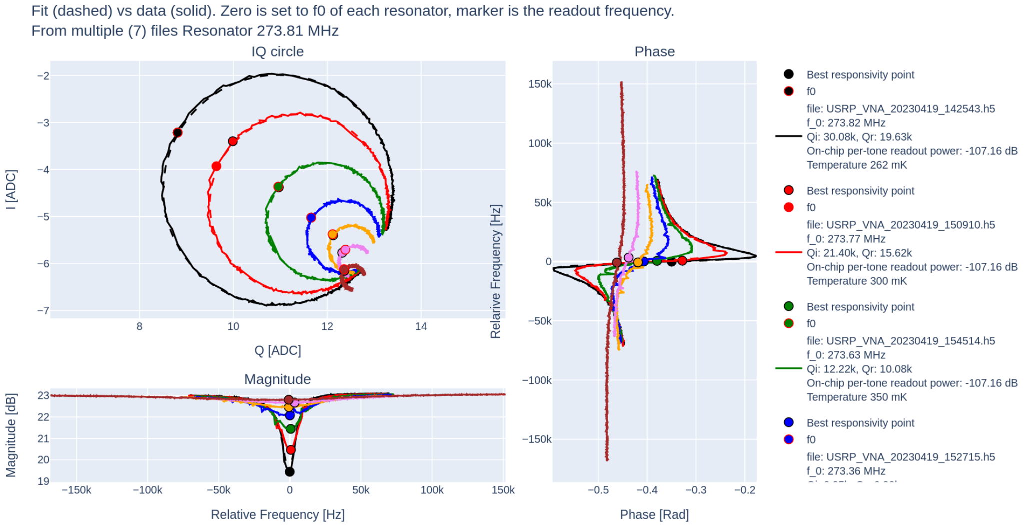

Fit (dashed) vs data (solid). Zero is set to f0 of each resonator, marker is the readout frequency.
From multiple (7) files Resonator 273.81 MHz

Figure 4.1: Screenshot of the GPU_SDR fit web visualizer. The upper left plot is the IQ complex plane; the lower left plot depicts magnitude in function of frequency; the right plot is a rotated plot of phase in function of frequency. In every plot, The solid line reports the data coming from the VNA scan, the dotted line is the fit and the solid marker is the fitted resonant frequency. The different traces correspond to the segment of the VNA scan centered on a device at 273.81 MHz @ 262mK. Each trace is a VNA scan performed at at a different stage temperature.

with a technique similar to Figure 4.1. Using $F(f_0)$, we can reconstruct the island temperature in function of power applied to the island and thus, knowing the bath temperature, calculate the thermal conductance $G(T_{\text{bath}})$ of the device. Furthermore, as shown in Figure 4.3 we can fit for the relation $P = K(T^{n+1} - T^{n+1}_{320\text{mK}})$ where P is the power dissipated by the heater, T is the island temperature, K is a material constant and n is a power law index related to the number of effective dimensions of the legs. We expect $n = 2$ because the main contributor to the thermal conductivity of the legs and the main design handle we have on G are the metal films we deposit on the legs; see section 2.4.

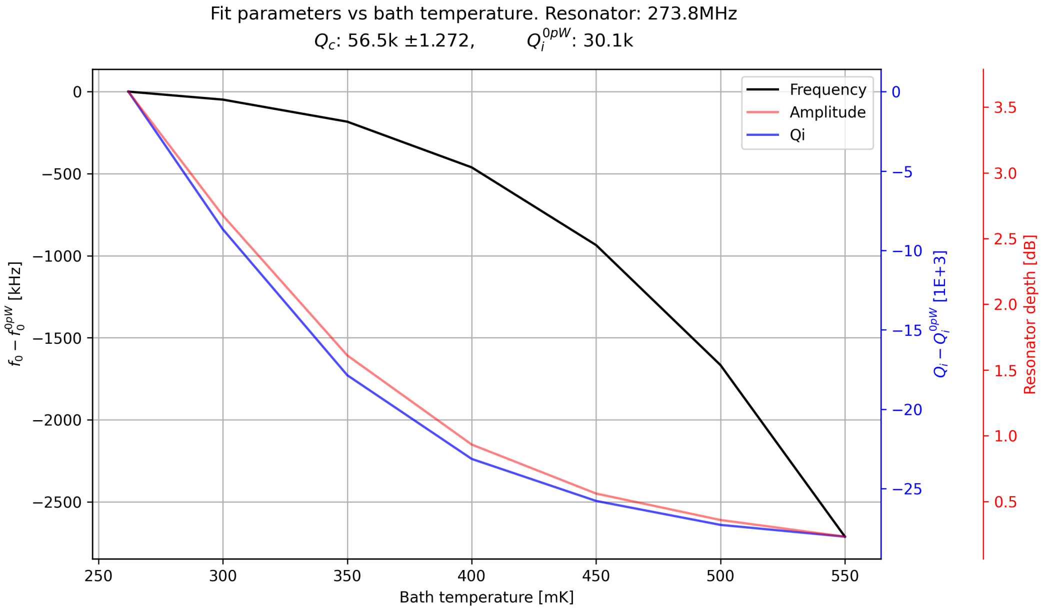

Figure 4.2: Parameters extracted from the fitting reported in Figure 4.1, in function of the UC stage temperature. Because of the good thermalization between the stage and the tile we approximate the bath (silicon tile) temperature with the UC stage temperature. Also, because these tests are performed in a dark configuration, the island temperature T_i is approximated with the UC stage temperature. On the Y axes there are the internal quality factor shift, the resonator depth and resonant frequency shift.

Device responsivity

While the characterization of the leg's thermal conductivity provides a correspondence between the device resonant frequency f_0 and the island temperature T_i over an extended temperature range, the estimation of the device responsivity provides a calibration constant, the responsivity R, to convert small fluctuations of f_0 into a measure of the power dissipated on the island by the heater. R is especially useful to determine if the internal noise of the device matches the models exposed in Chapter 2 and, more importantly, to determine if the detectors are suitable to measure B-mode polarization patterns in the 150GHz sky from the South Pole. To measure the responsivity, we cool down our devices in a cryostat in dark configuration and use the calibration instrument described in section 3.2 to keep the cryostat cycle stable and the LNA powered. We connect the optical fiber of the calibration instrument to a commercial optical signal transceiver and drive the apparatus with a benchtop function generator. The function generator is set to reproduce a square wave of frequency ~ 1 Hz. The optical signal causes the power applied to the heater to fluctuate around the bias set point. Small changes in the island temperature T_i

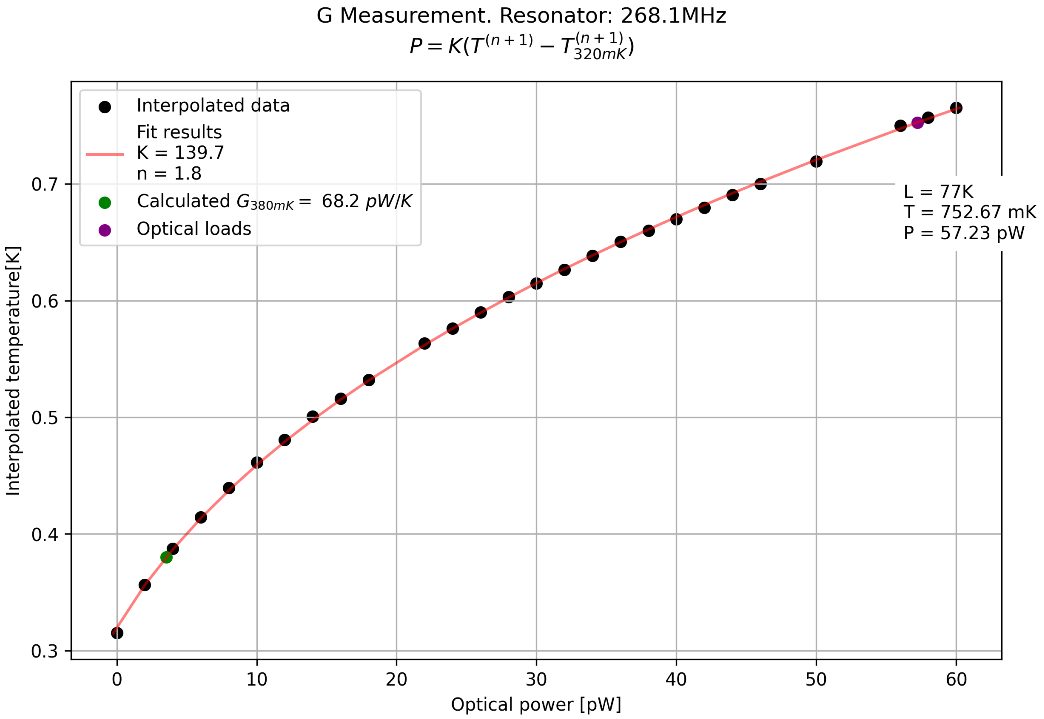

Figure 4.3: Using the data reported in Figure 4.2, we build an linear interpolation function that maps resonant frequency shifts to island temperature changes, $F(f_0) \Rightarrow T_i$; we use the calibration heater on the island to dump a controlled amount of power on the island and measure the frequency shift of the device. Using the function $F(f_0)$ we can build the plot in the figure. On the X-axis we report the dissipated optical power, on the Y-axis we report the interpolated island temperature. The black marker are data points, the red line is a fit to the function $P = K(T^{n+1} - T_{320\text{mK}}^{n+1})$. Where P is the power dissipated by the heater, T is the island temperature, K is a material constant and n is a power law index related to the number of effective dimensions of the legs. We expect $n = 2$ because the main contributor to the thermal conductivity of the legs are the deposited metal films, see section 2.4. The fitted function is used to calculate the thermal conductivity of the legs at the operating temperature of 380 mK, green marker. This result is used to inform the modeling of the internal detector noise.

cause small fluctuations in the resonant frequency $f0$ of the device, as shown in Figure 4.4. The fixed tones readout is used to measure the resonator fluctuation. As discussed in section 3.4, the VNA's fit is used to convert the IQ samples to a frequency timestream; a diagnostic plot verifies that the resonator is stable during the measurement and that the fluctuation is small enough not to alter the device properties, as shown in Figure 4.5. From the data reported in Figure 4.4, we can calculate a conversion constant, the responsivity, valid for small fluctuations around f_0. The responsivity, expressed in units of aW/Hz, allows us to convert the power spectrum of a frequency timestream, or NEF (noise equivalent frequency), to a NEP (Noise Equivalent Power) spectrum. The responsivity is also valuable for correctly subtracting the timestreams of the detector reading orthogonal polarization from the same pixel of the array. Slight inter-device variations in the fabrication process are to be expected, and often, result is slightly different responsivities for each TKID device. The signal of interest is of polarimetric nature; it is obtained as the difference between a pair of devices. Suppose the responsivity variation between two devices reading the same antenna is not accounted for. In that case, the resulting polarization measure will contain incorrect information, ultimately mixing E, B, and T maps [97]. However, calibration of the detectors using heaters is unnecessary for deployment operations. The deployment calibration is performed directly using the sky temperature map. The heater calibration is a tool for exploring the internal Physics of the devices and performing quality control checks on the tiles.

4.2 Noise performances

The instrument described in section 3.2 is used to apply a 6 pW bias to the island heater. The 6 pW value is the same power we expect from instrument + atmospheric optical load in a deployment scenario. We keep the cryostat in dark configuration so to completely control the island loading via the heaters. We transform the frequency timestreams coming from the detector's simulated optical power timestreams using the previously measured responsivity R around 6pW. For each pair of detectors (two detectors coupled to the same antenna on different polarization summing networks), we simulate a polarization measurement by building a pair difference timestream, $D(t)$, as $D(t) = R_1 \cdot S_1(t) - R_2 \cdot S_2(t)$ so to compensate for an eventual difference in calibration. We transform the result and obtain a Noise Equivalent Power (NEP) spectrum we can directly compare with the desiderata established in Chapter 1. As detailed in Figure 4.6, the pair difference spectrum exceeds the noise requirement of $45aW/\sqrt{Hz}$ @ 1Hz. If we suppose our predictions about the dominant noise

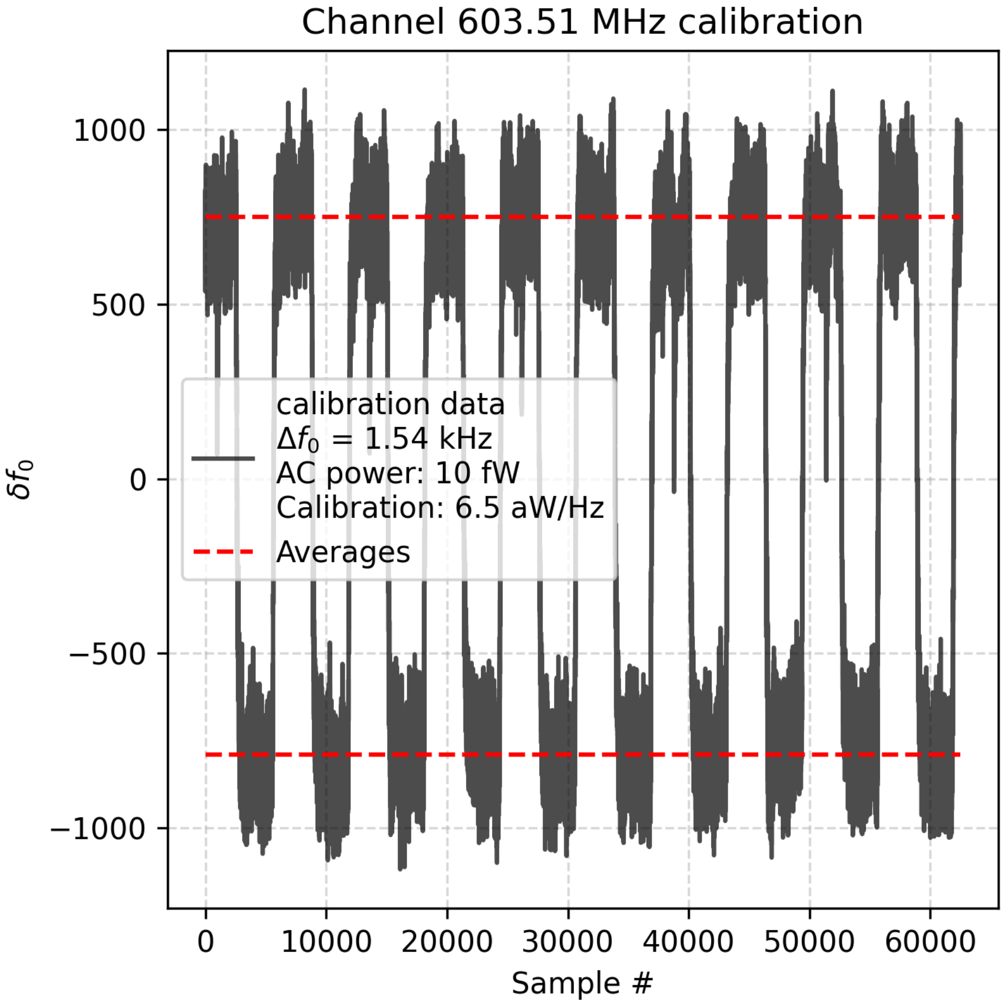

Figure 4.4: Timestream, in units of $f(t) - f_0$, of the device calibration phase. The Y-axis is the frequency shift of the device respect to the steady optical bias position in Hz, the X-axis is the sample number. The calibration is obtained by estimating the frequency shift of the resonator in response to a small fluctuation of the power dissipated on the island. In this case we use a square wave to drive the current source and we measure the frequency shift as difference between the top and bottom mean rail position. The average of the top and bottom rail are reported as red dashed lines. Knowing the peak to peak amplitude of the square wave (AC power in the plot) we can determine the responsivity of a TKID.

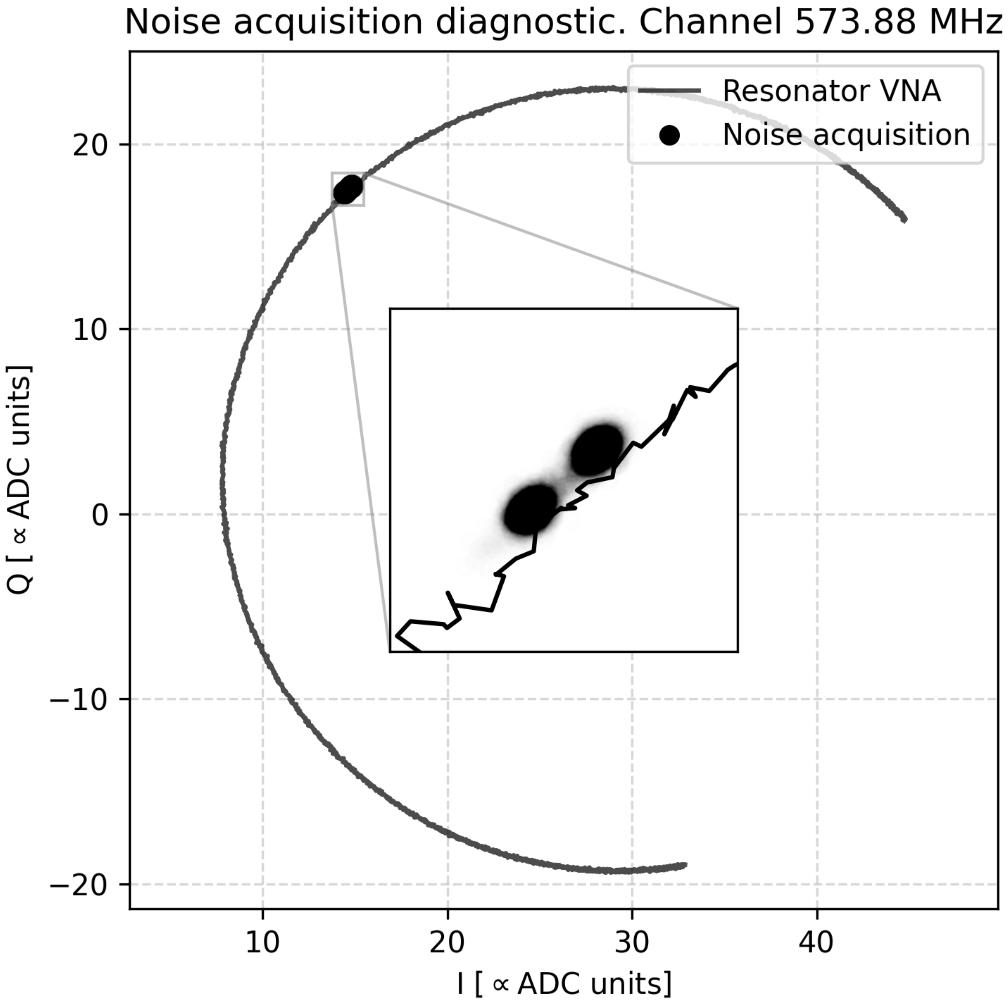

Figure 4.5: Diagnostic plot of the measure plotted in Figure 4.4. The X and Y axis represent the complex resonator plane, in units proportional to the ADC units, the solid line is the VNA acquisition data and the faded markers are the data from the noise acquisition in the calibration phase. A zoom in on the markers reveal the two rails of the calibration square wave as two separate spots on the resonator circle.

hierarchy are correct (in what order noise generation phenomena are dominant), we can fit the difference spectrum for two separate single poles functions: the phonon noise and the GR (generation-recombination) noise and a plateau given by TLS (Two Level System) and readout noise. The analysis can then be repeated on measures performed with a different simulated optical bias and a different readout power. The results of the fits are then compared to the theoretical expectation for the total noise and individual noise components, see Figure 4.7 where the model for the noise has been regenerated to account for the specific properties of the devices tested (i.e., specific G, R, K, n). While there is general agreement with the theoretical prediction on the noise, we can clearly see in Figure 4.7 that further modeling is required to fully explain the intrinsic noise of TKIDs. Nonetheless, these measures demonstrate the validity of the technology as a photon noise-limited detector for cosmological observations.

4.3 Near field beams

A pixel's near-field beam map (NFBM) characterizes how each antenna illuminates the telescope aperture in the time-reversed sense [98]. The functional role of NFBM data collected on these devices is to ensure compatibility with their TES counterpart. De facto, the demonstrator camera intends to use the membrane-suspended KIDs as a drop-in thermometric element, and thus, in order to demonstrate the technology, we need to make sure that the pixel beams are comparable to what was previously deployed. The dual polarization slot antenna design is well known [39], and we have already replicated the performance on TKIDs test chips [99]. However, the array scale fabrication process may introduce undesired effects in the beam shape. We measure the NFBM using an XY motorized stage, suspended at $\sim 12in$ from the focal plane, to move an incandescent, chopped ceramic source in front of the telescope aperture. The chopping frequency is 17Hz to avoid other noise sources, allowing for a straightforward demodulation of the mapper signal. The optical load of the mapper structure, $300K$, results in the array's resonators having very high responsivity and extremely high coupling with the RF line. Furthermore, the optical load generated by the chopped source, $\sim 500K$, moves the resonators by $O(kHz)$ around the initial, unloaded position. The fastchirp readout technique, previously described in section 3.5, allows us to track most of the devices accurately. The measurement consists of moving the chopped source in $0.25in$ steps across a plane encompassing the aperture of the telescope. Position and timing data from the stage motors movement is then used to partition the detector signal timestream in

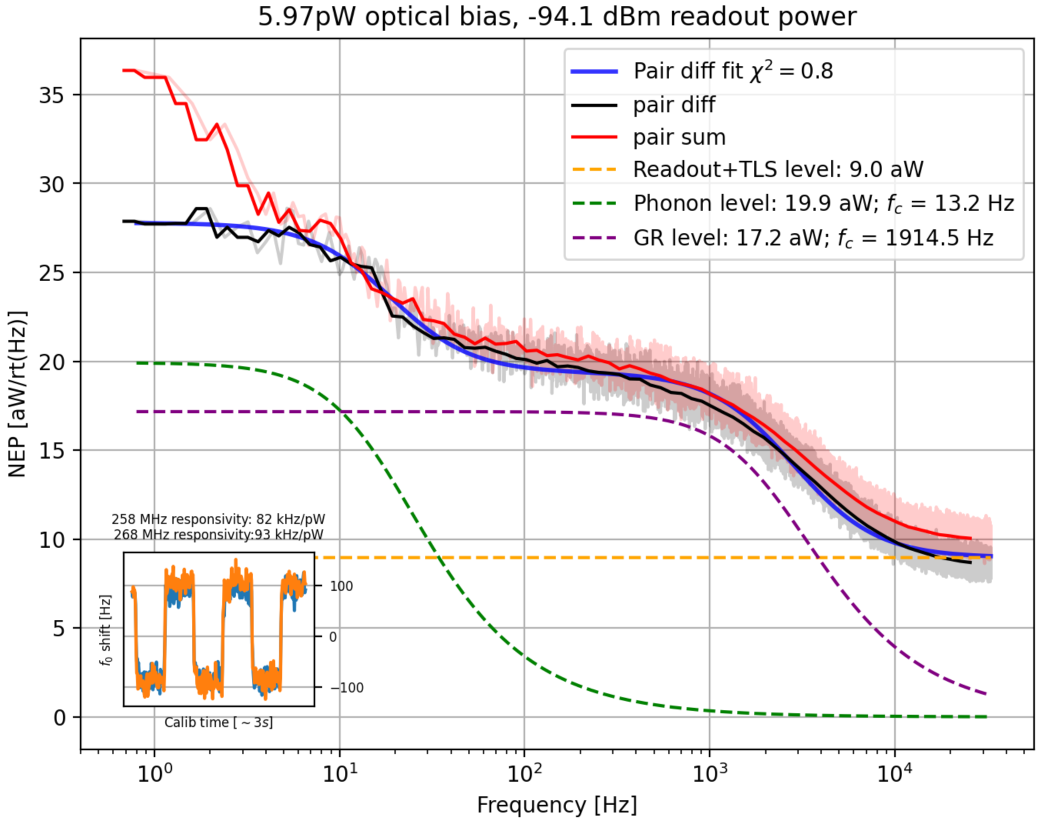

Figure 4.6: Noise Equivalent Power (NEP) spectrum of a pair of TKIDs. The NEP is acquired with a simulated optical loading of 6 pW in a cryostat with no optical coupling. The spectra reported in this plot as faded black and faded red are: the pair difference NEP, obtained as the transform of a responsivity weighted subraction of detector timestreams; the pair sum NEP obtained as the weighted sum of the detector timestrams. The solid lines are a logdecimated (constant number of points per decade) version of the spectra, plotted for clarity. The dashed lines are the noise components fits and the blue solid line is the total noise fit. In the lower left corner we report a chunk of the calibration timestream of both detectors for diagnostic purpose. Towards the low frequency end of the spectrum we notice how the pair subtraction attenuates the low frequency fluctuation of the signal. On the high frequency side we notice a slight difference in the levels of the pair sum and pair difference; this is the result of common mode high frequency noise injected by the use of an off-resonance probe tone for RF line fluctuation compensation.

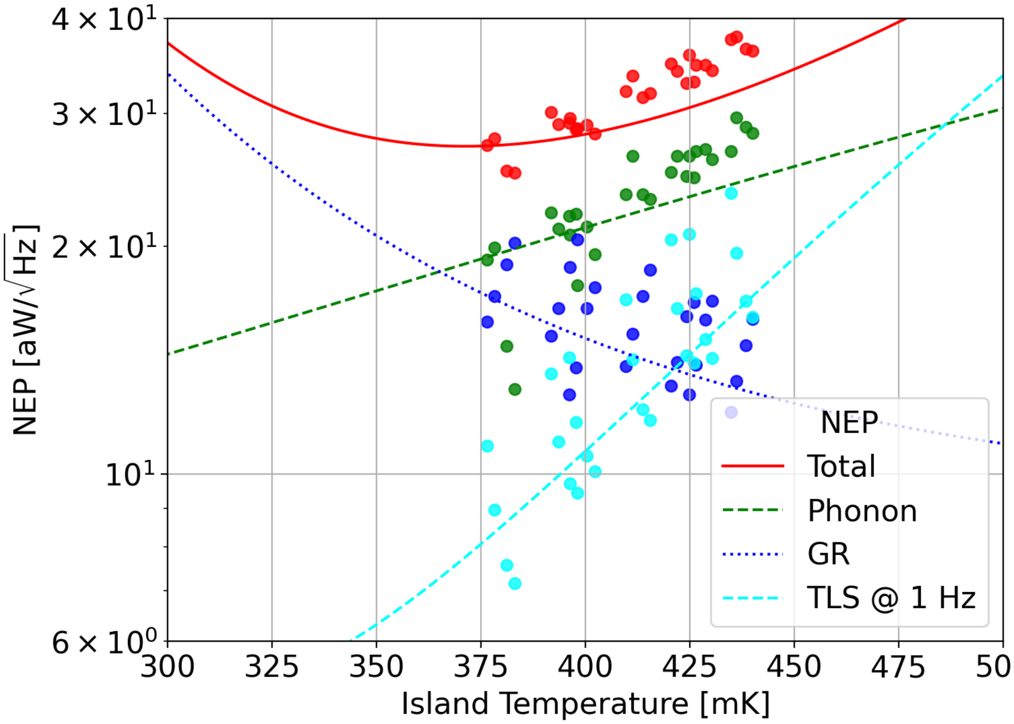

Figure 4.7: Zoomed in version of Figure 2.4. The thermal conductance of the devices legs is used to convert the total power dissipated on the island, $P_{\text{readout}} + P_{\text{opt}}$ in this case, to an island temperature, T_i. Various readout power and optical bias are measured, for each measure a pair-difference NEP spectrum is fitted with the noise model, see Figure 4.6 for an example. The component noise level resulting from each fit is reported on this plot as a marker. The lines represent the theoretical prediction of the noise levels in function of the T_i. While the overall trend and levels of the predicted and measured noise are not far from accordance, more modeling is required to better understand the data spread. Specifically, we measure a significant shift in the composition of the noise with the change in readout power.

spatial bins. For each detector and each spatial bin, the intensity of the copped signal is estimated via demodulation of the $\sim 17Hz$ periodic signal obtained by synchronously digitizing the chopper feedback. In Figure 4.8, we report, under the data subplot, the raw image we built for the NFBM of a single detector. The raw data is then fitted with a rotated 2D Gaussian. The resulting widths σ_x and σ_y are compared with the expected beam from the detector, reported as the analytical model in Figure 4.8. The expected near field beam pattern is given by approximating the antenna as a square aperture, the expected beam with reported in Figure 4.9 is obtained by fitting a Gaussian function to the main lobe of the pattern.

The sampled number of devices affords a statistically robust representation of the array, encompassing 77 beams across the 128 devices fabricated on the wafer.

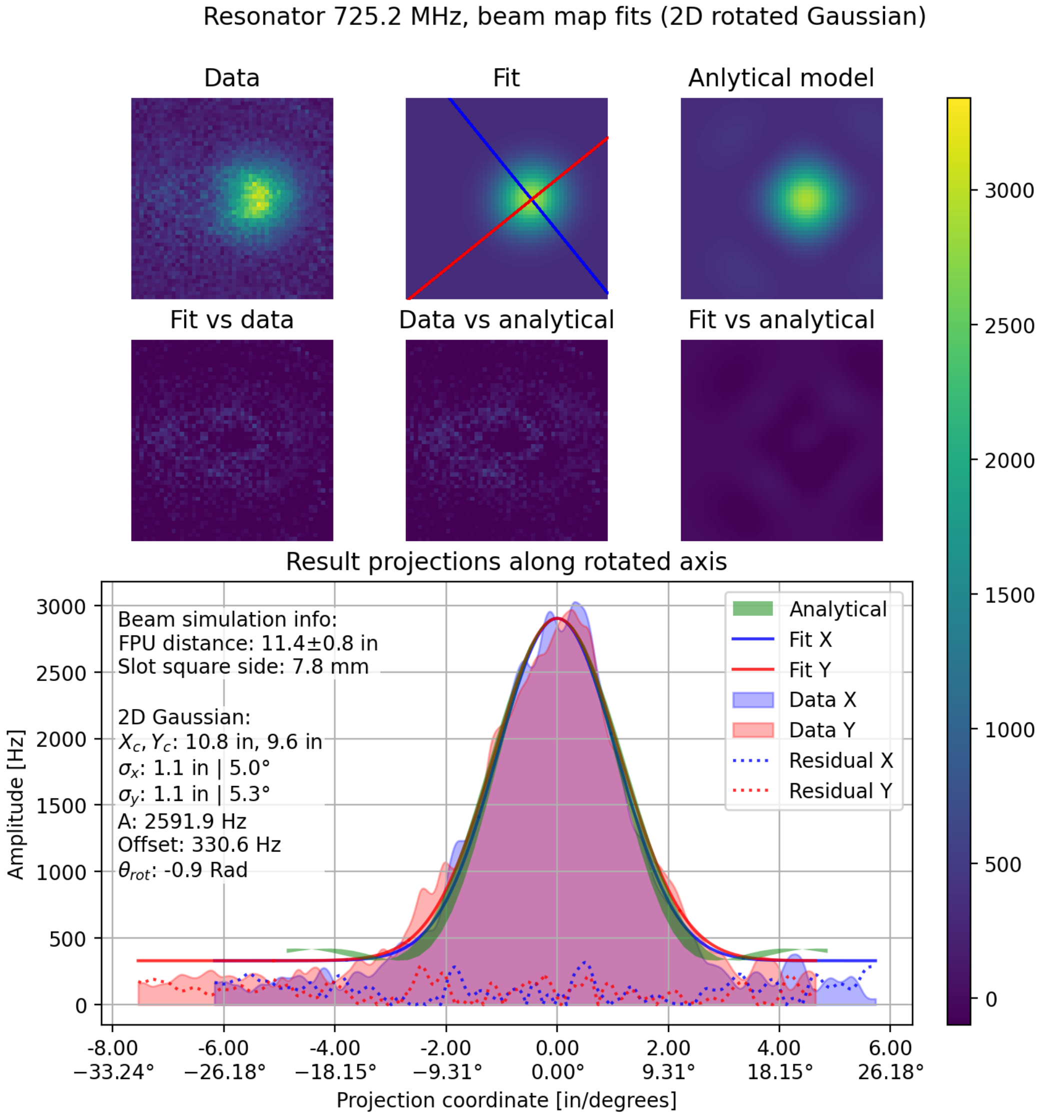

Figure 4.8: Near field beam mapping results for a single device. The figure's upper portion is divided into six plots reporting the spatially binned data, Gaussian fit, analytical model, and respective differences. The color scale to read the heatmaps is reported on the side in Hz. The bottom part of the plot represents the same data as the top part projected along the axis of the Gaussian fit. The X-axis is reported in inches and degrees, where the degree projection is obtained using the geometry of the mapper apparatus. The Y-axis and the color scale report the amplitude of the response to the chopped signal in Hz. The analytical model is plotted as a green area as we account for the mapping plane irregularities.

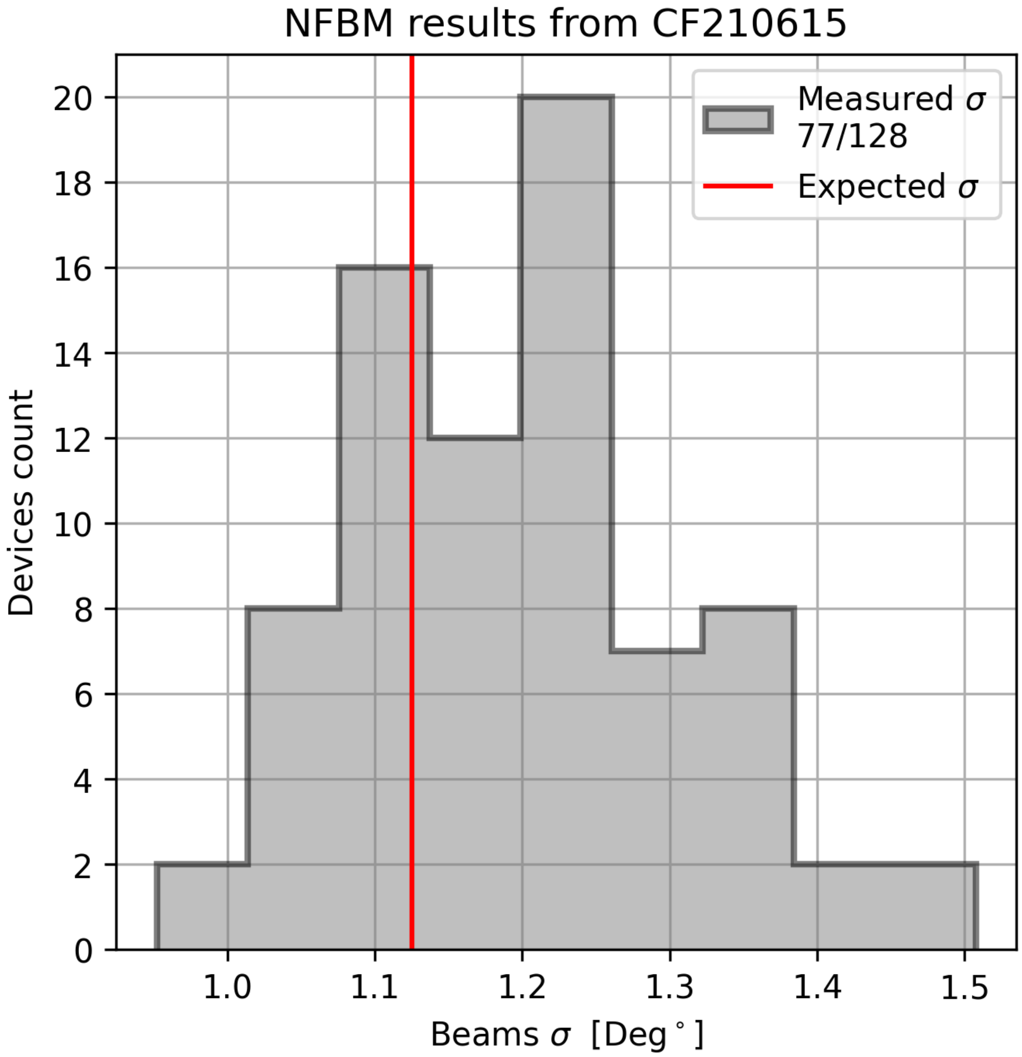

Figure 4.9: Distribution of the fitted beam widths σ resulting from the analysis of NFBM data from the tile labeled CF210615. The σ reported in this plot is a geometric average of σ_x and σ_y for each device. See an example in Figure 4.8. The expected σ, reported in the plot as a vertical red line, is obtained by fitting a Gaussian curve to the main lobe of a square aperture near-field pattern. The number of detectors that yielded a significant NFBM is less than the array's resonator yield because of fabrication defects and readout challenges due to the test optical load being significantly higher than the design specification.

Notably, the tile under investigation exhibited a post-trimming yield of 101 out of 128 devices. Among the 101 devices observed without loading, 9 manifested negligible optical responses, indicative of fabrication imperfections in the antennas. Furthermore, 15 devices exhibited resonators excessively over-coupled or overlapped under the laboratory optical loading conditions. As illustrated in Figure 4.9, the fabrication process developed for TKID arrays yields 150GHz antennas compatible with the expected beam profile.

4.4 Optical efficiency

We have a way to directly measure or calibrate the responsivity of TKIDs: a Kelvin resistance measure of the heater on the island allows us to inject a precise amount of power. We can then record the frequency shift of the resonator and use the device as a calibrated thermometer of the island temperature. In the top portion of Figure 4.10, we expose the aperture of the telescope to a 77 K optical load, realized via a back body in a liquid Nitrogen bath. We bias the island heaters with a power ranging from 83 to 0 pW. We acquire a VNA scan for each heater bias, resulting in a row in Figure 4.10. During this measure, we can observe the devices equipped with the heater increasing their resonant frequency as the island temperature decreases while all the other devices remain static. As plotted in the mid portion of Figure 4.10, we keep the on-device heaters to 0 pW and proceed to let the liquid Nitrogen bath slowly evaporate. The change in optical load drastically affects all detectors on the array except for a few devices intentionally designed with no antenna (dark devices). This process is necessary for large arrays where laboratory optical conditions have increased the responsivity because minor array-wise variations in devices' responsivity and efficiency and resonator overlapping can confuse the identifications of unique devices. This method allows us to track each device resonant frequency during the optical load temperature transition between 77 K and 300 K. Once the Nitrogen bath is fully evaporated, we swap the optical load with a "dry" one to make sure the temperature is stable at 300 K. We perform one final VNA scan, reported in the bottom part of Figure 4.10. We match the position of the resonators equipped with heaters at 300K (bottom part) with the position of the same resonator under 77K optical load plus heater power. The matching operation is highlighted in Figure 4.10 as dotted white lines. The power needed to achieve the same resonant frequency corresponds to the difference in optical power dissipated on the island by a 300 and 77 K loads, namely $\Delta P_{300/77}$. We define the optical efficiency as:

$$\frac{dP_{\text{opt}}}{dT} \approx \frac{\Delta P_{300/77}}{300K - 77K} = \eta \cdot k_b \cdot \left(\frac{\Delta\nu}{\nu_0}\right) \cdot \nu_0 \tag{4.1}$$

where η is the optical efficiency, ν_0 is the center of the optical band and $\Delta\nu$ is the optical bandwidth. For the purpose of the estimation of the optical efficiency we consider the design nominal $\nu_0 = 150GHz$ and $\Delta\nu = \nu_0/4$. As reported in the full tile distribution in Figure 4.12, the measured optical efficiency per detector, corrected for dark stimulation effects (see section 4.6), meets or exceeds the requirements set by the TES counterpart [32], $\eta > 30\%$.

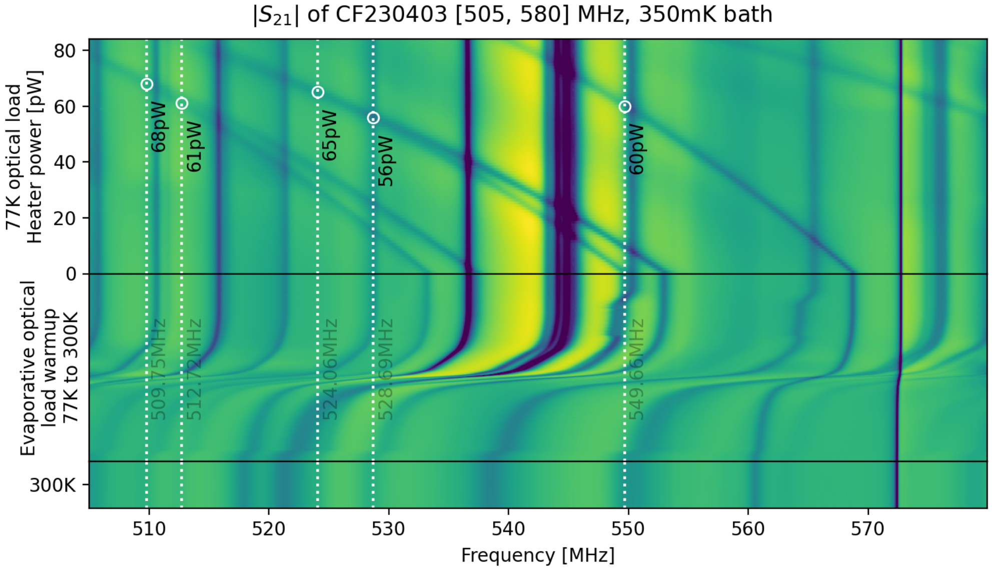

Figure 4.10: Waterfall plot of the partial S_{21} of a TKIDs array during the optical efficiency measurement. The plot has three parts delimited by black horizontal lines. The plot's X-axis is the frequency at which S_{21} is measured across all plot sections. The color scale is a function proportional to S_{21}; the scaling of S_{21} is needed in this plot to enhance the contrast and visualize over-coupled resonators. The Y-axis has a different role in each section of the plot, as during this measurement, we control two variables: the power applied to the TKIDs calibration heaters and the optical load temperature, which ranges from 77 K to 300 K. In the upper section, the Y-axis is the power applied to each heater in pW, the optical load is kept at 77 K with a bath of liquid Nitrogen; in the midsection, the devices heaters are not used, and the Y-axis represents the change in optical load temperature during the uncontrolled evaporation of the Nitrogen bath. The bottom part has a single value for the Y-axis indicating that the optical load has been swapped for a 300K, dry black body. The white dotted lines link the resonant frequency of each heater equipped device at 300K with the power needed to achieve the same resonant frequency under a 77 K optical load condition.

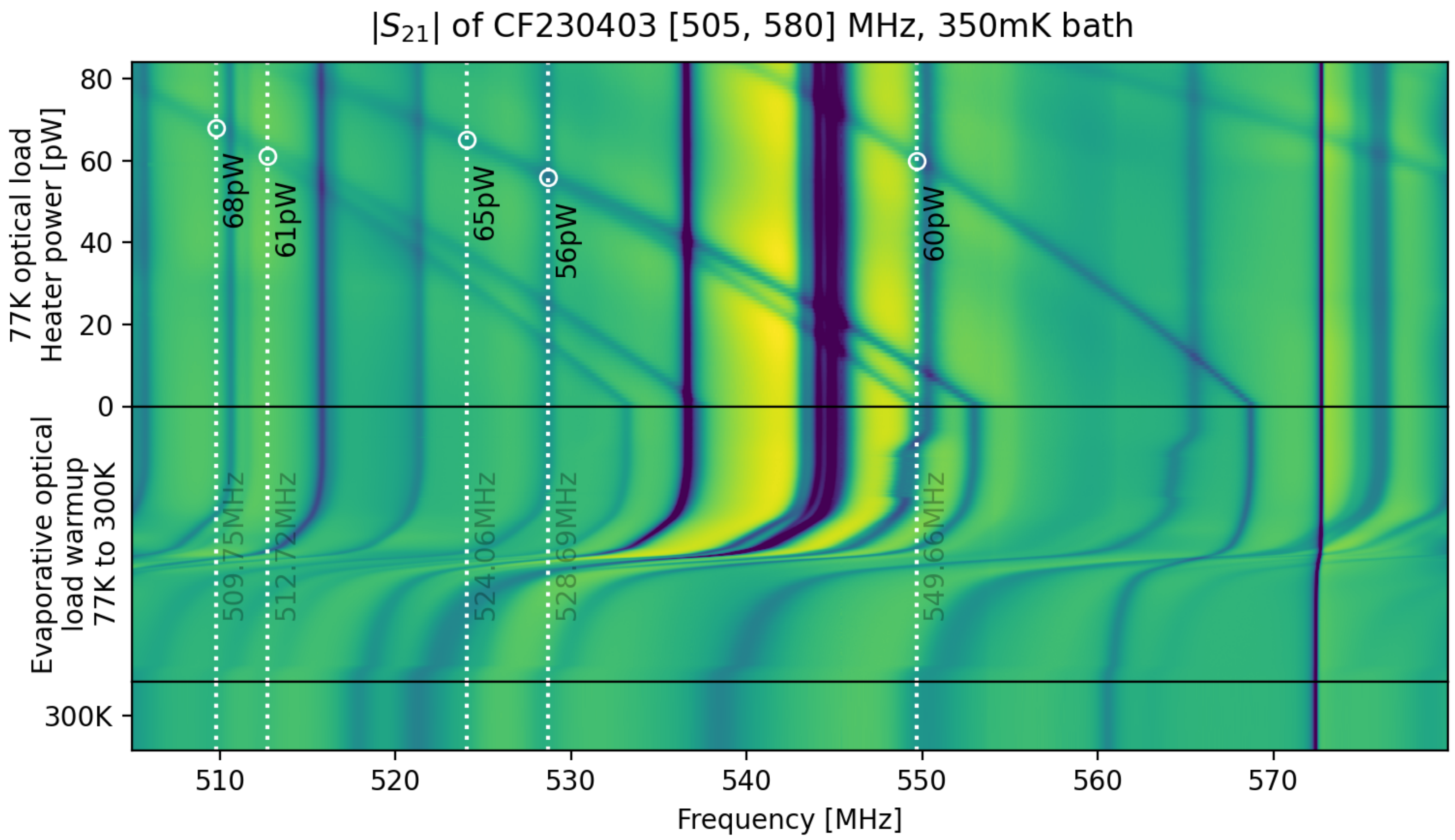

Figure 4.11: Full page view of Figure 4.10

4.5 Optical band

To measure the optical band-pass of TKIDs on the array, we use a Martin-Puplett Fourier Transform Spectrometer (FTS) that can be mounted directly onto the aperture of the telescope. This spectrometer has a thermal source that is differential between 77 K and 300 K. The FTS instrument and the methodology used to determine the optical band are in line with the standard BICEP Array techniques [100]. We use the fastchirp readout technique, described in section 3.5, to measure the resonant frequency of our detectors while we move the primary mirror of the FTS. Plotted in the top portion of Figure 4.13, there is the spectrum of the fastchirp response, where the resonator of interest has been highlighted. The observed spectral profile contains a multitude of overlapped resonators, extremely overcoupled due to the 300K optical load. The spectral profile is significantly different from the profile shown in Figure 3.21 : the dark devices retain their sharp ringdown profile while the antenna-coupled detectors emit a significantly broader ringdown profile. The beam of the FTS instrument requires a precise alignment with the antenna of the detector and thus, tracking all the devices available in the band is not necessary. To better reconstruct the FTS signal, we limit our post-processing analysis to a spectral band around the resonator and fit each frame with a complex Lorentian assuming a single resonator is present in the region of interest. The interferogram resulting from fitting the resonator, bottom part of Figure 4.13, is clearly visible in non-averaged data. The dark line is the fitted mean of the distribution and each column in the background heatmap represent a fast-chirp frame. To boost the signal to noise ratio, the final optical band plot, reported in Figure 4.15 is measured averaging 100 mirror passes, where each pass has been alligned using timing data collected from the FTS instrument. We look at the timestream corresponding to optical response ranging from 5GHz to 300GHz and we determine that the only region containing signal is the one reported in Figure 4.15. Because the working principle of the FTS is based on optical load temperature difference and we do have a calibration for our devices, we can report the optical band in Figure 4.15 directly in units of efficiency. The number of devices analyzed using the FTS, four in total, is not statistically significant. We do not require full spectral band verification of every pixel on the array as the measurement is intended to detect egregious source of stimulation coming from the insertion of membrane suspended KIDs as a thermometric element of the detector or the possible impact of TKIDs fabrication strategies on the antenna performance. The quality control of every legacy geometric features, such as antennas, necessary for deployment is out of the scope of this work. The measured optical band is well

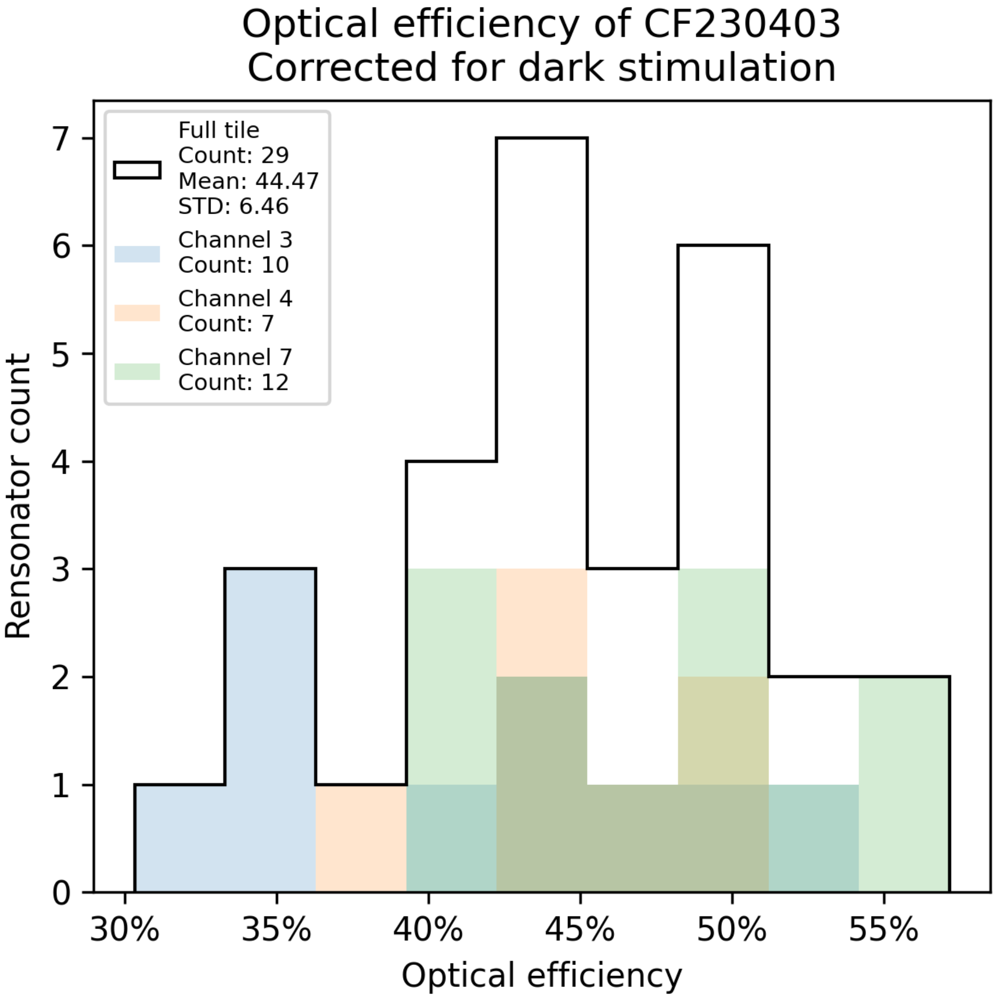

Figure 4.12: Optical efficiency distribution for the TKIDs tile labeled CF200403. The distributions reported in different colors refer to the distribution of optical efficiencies of detectors connected to different heater line. Each heater line has 16 heaters in series, each places on an individual island. The number of detector measured here is significantly lower than the resonator yield of the tile as not all the resonators on the array are equipped with a heater on the island.

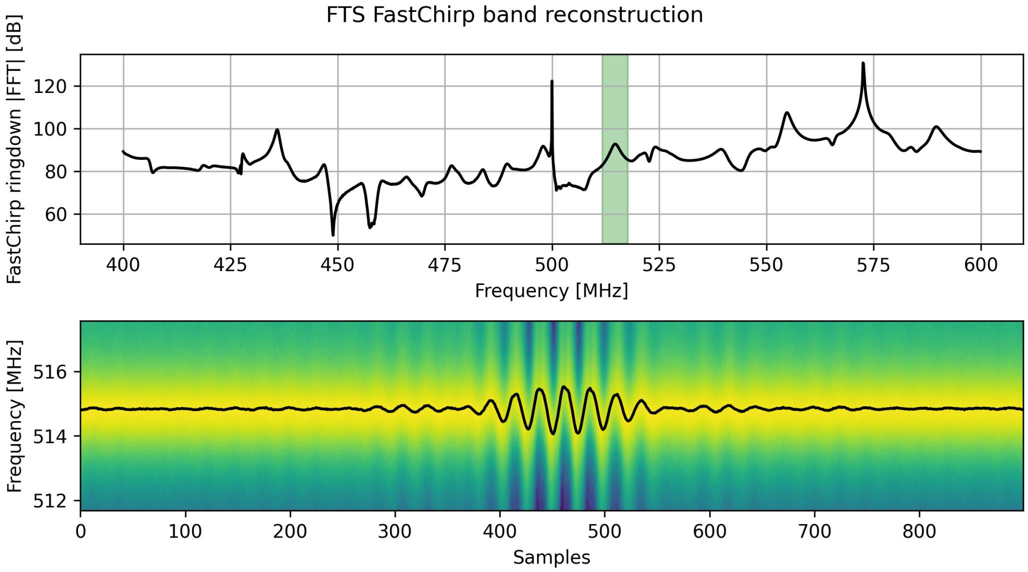

Figure 4.13: Example of the FTS data collected from a single device on the array. The top portion of the plot reports the FFT of averaged fastchirp cycles collected on a TKID array or, equivalently, a single fastchirp frame. The Y-axis reports the magnitude in dB units of the Fourier transform of accumulated ADC units, the X-axis is the frequency of the response. The small peaks are gererated by the ringdown of antenna-coupled devices, over-coupled to the RF line because of the high optical loading; the sharp peaks are devices without an antenna. The frequency region highlighted by the green band on the plot represents the region considered for resonator fitting. The same frequency region is reported on the Y-axis of the bottom part of the plot. The X-axis of the bottom plot is sample number or, equivalently fastchirp frame number, proportional to time. The time interval shown corresponds to the portion of mirror movement generating the detectable part of the FTS interferogram. The colorscale correspond to the Y-axis of the top plot. The black line over-plotted to the heatmap is the resonant frequency resulting from fitting each frame (column) in the plot.

in line with the design parameters. No significant out-of-band optical signal was absorbed.

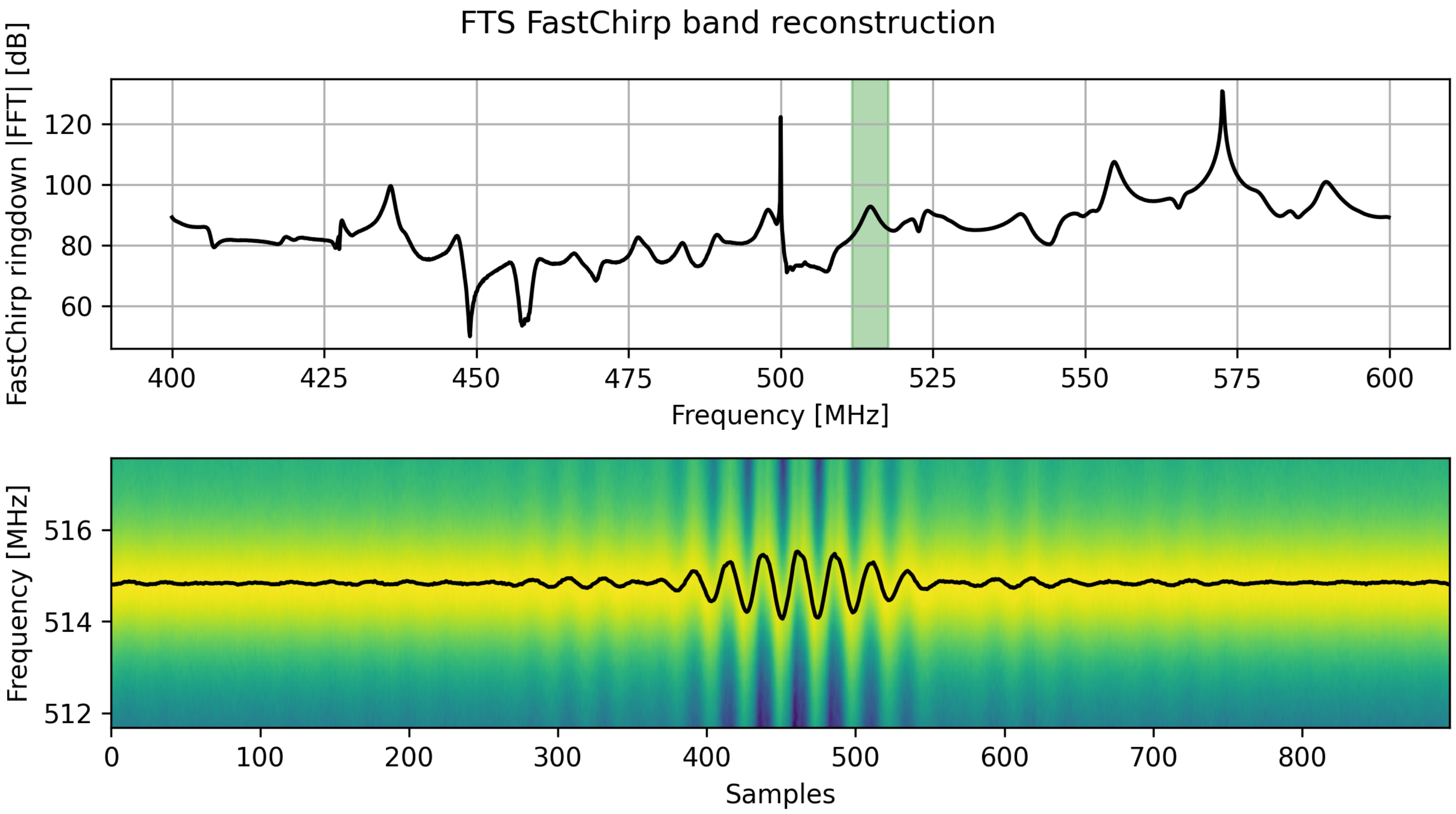

Figure 4.14: Full page view of Figure 4.13

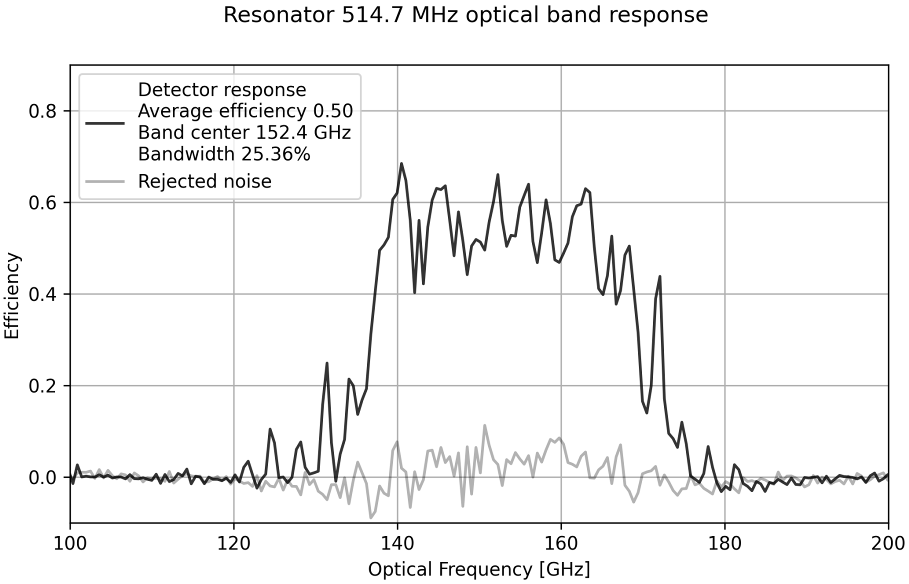

Figure 4.15: Optical band of a TKID from an array, resulting from FTS measurements. The X-axis is the frequency of the optical radiation incident on the device antenna. The Y-axis represent how efficiently the device measure optical radiation at a certain frequency. The black trace represent the detector band while the grey trace represents the noise rejected via zero path subtraction rotation [101].

4.6 Direct stimulation

As visible in the middle portion of Figure 4.10, the dark resonator (device not connected to an antenna) present in the band changes resonant frequency slightly during the optical load warm-up. A closer look at all the dark devices present on a tile, reported in Figure 4.17 reveals that a significant frequency shift is common to all dark devices. A first attempt at explaining the signal in dark detectors upon optical load change, is the presence of direct stimulation of the thermometric element: the geometric layout of the TKID absorbs optical radiation. In this scenario, we should be able to measure optical response in the band outside the designed optical band. No out of band response was measured for antenna coupled devices. The dark detectors response to an optical load change could also be explained by supposing that, even if the temperature of the FPU (Focal Plane Unit) is regulated, the local temperature of the tile changes in response to the load due to radiation leakage in the camera tube filter stack. A small rise in the tile temperature would result in a global shift of the array resonant frequencies.

Regardless of the heating mechanism, in order to direct absorption effecst, we first measure that the thermal responsivity, $R_t \equiv \partial f_0/\partial T_b$ of the dark detectors does not change significantly with different optical load temperatures, nominally 77 and a 300

K. In order to measure R_t, we measure the frequency shift of the resonators while varying the thermal bath temperature by about 30mK in both optical load conditions. As reported in Figure 4.17, the thermal responsivity of antenna-coupled (optical devices) devices R_t^o increases noticeably while there is no significant increase in the thermal responsivity of dark devices, R_t^d. We define the quantity $\Delta R_t = R_t^o / R_t^d$ as the ratio measured in Figure 4.17b. In order to estimate the contribution of local heating to the measure of the optical efficiency, we write that the frequency shift of a resonator, Δf_0, due to thermal bath fluctuations is:

$$\Delta f_0 = \delta T_b \cdot R_t \cdot G(T_b) \tag{4.2}$$

where δT_b is the fluctuation in bath temperature, and $G(T_b)$ is the thermal conductivity between the TKID island and the tile at a given bath temperature. We can estimate the frequency shift induced by local heating in optical devices by considering the equation 4.2 separately for dark and optical devices:

$$\frac{\Delta f_0^o}{\Delta f_0^d} = \frac{R_t^o}{R_t^d} \cdot \frac{G(T_b)^o}{G(T_b)^d} \quad \Rightarrow \quad \Delta f_0^o = \Delta f_0^d \cdot \Delta R_t \tag{4.3}$$

where we approximate $G(T_b)^o \sim G(T_b)^d$ because we assume the fabrication of the array to be uniform. In order to get the dark stimulation correction mentioned in Figure 4.12, we calculate the thermal Δf_0^o contribution to the optical device frequency shift measured on a load change, middle portion of Figure 4.10, using equation 4.3. For each device, we calculate the optical efficiency using equation 4.1 where $\Delta P_{300/77}$ accounts for Δf_0^o. The resulting power correction results to be $< 8\%$ in the worst case.

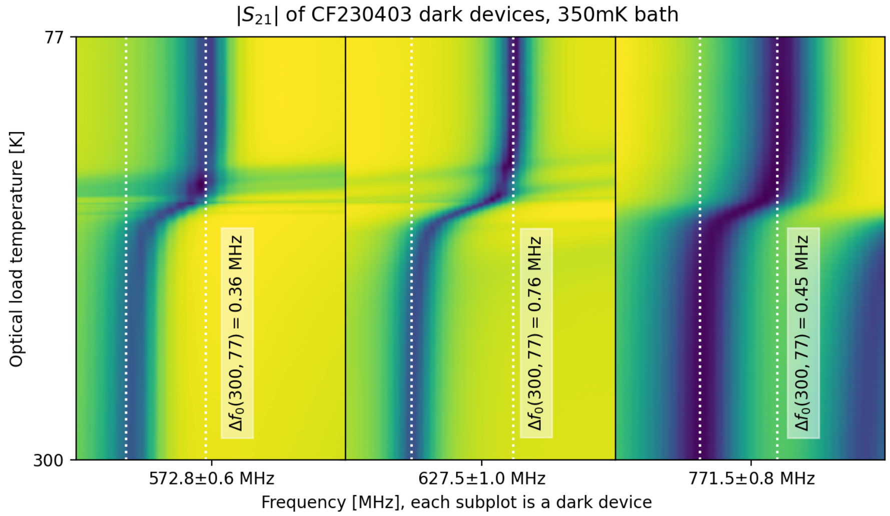

Figure 4.16: Response of detectors without antenna coupling (dark detectors) to variation in optical load from 77K to 300K. This Figure reports data for the experiment plotted in the middle portion of Figure 4.10. The Y-axis reports the optical load temperature during the uncontrolled evaporation of the Nitrogen bath, The X-axis id divided in 3 portion and represents three different frequency regions, one around each dark resonator. The colorscale is proportional to the $|S_{21}|$ function of the device. The white dotted lines show the resonant frequency of the resonators in both end-cases, 77 and 300K. The optical response of dark resonators is attrinuted to a local heating effect rather than direct stimulation because of there is no trace of out-of-band radiation absorption is the FTS spectra.

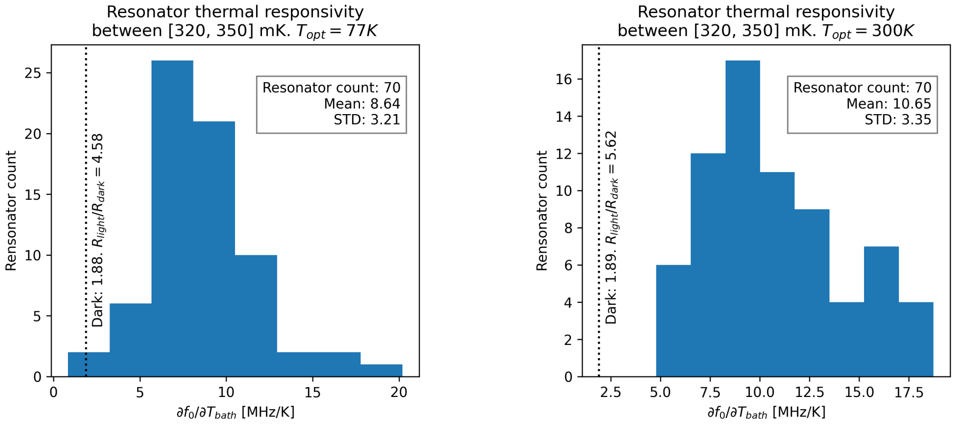

(a) 77K optical load, eccosorb in liquid Nitrogen bath

(b) 300K load, room temperature dry eccosorb

Figure 4.17: Histograms of thermal responsivity, $R_t \equiv \partial f_0/\partial T_b$, measured with different optical loads. R_t is measured as $(f_0^{320mK} - f_0^{350mK})/30mK$ for each resonator. Only resonators clearly identifiable in the 300K case were considered for this test. The number of non-optically coupled resonators (dark) is reported as a black dotted vertical line as we only have 3, the distribution plotted represent the optically coupled resonators. The purpose of this measurement is to show that the responsivity of the dark resonators does not change with the optical load. This fact implies that there is negligible optical radiation absorption in devices not coupled with an antenna.

Chapter 5

CONCLUSIONS

A crucial goal of future physics experiments involving bolometers, ranging from dark matter [102] to observational cosmology [23], is to increase detector counts to increase sensitivity of otherwise background noise limited sensors. The sensitivity needs of modern physics experiments often require superconducting thermometers and the scalability of the technology used has become a limiting factor [5]. Thermal Kinetic Inductance Detectors (TKIDs) are KIDs in which the inductive component of the resonator is suspended on a thermally isolated membrane alongside a resistive element, dissipating power received from an antenna. The Jet Propulsion Laboratory (JPL) and the California Institute of Technology have been leading the effort to deploy a demonstration TKIDs camera [103] to advance the readiness level of the TKIDs technology. The development of the prototype targets the performance and requirements of the 150GHz polarimetric camera tube of the BICEP Array observatory [32].

This work demonstrates that Thermal Kinetic Inductance Detectors are a suitable candidate for cosmological observations and specifically for the measurement of B-mode polarization pattern from the South Pole sky. The demonstration follows a state-of-the-art characterization of the optical performance of the detectors and a study of the intrinsic noise characteristics. We validate the thermal, electrical, and mechanical compatibility of the TKID's cold and room temperature support infrastructure with existing instrumentation. Furthermore, this work delivers a functional cryogenic camera system equipped with two science grade TKIDs tiles and with support for two more.

BIBLIOGRAPHY

[1] P. Ade, Z. Ahmed, R. W. Aikin, et al. "Constraints on Primordial Gravitational Waves Using Planck, Wmap, and New Bicep2/keck Observations Through the 2015 Season". In: *Physical Review Letters* 121.22 (Nov. 2018). ISSN: 1079-7114. DOI: `10.1103/physrevlett.121.221301`. URL: `http://dx.doi.org/10.1103/PhysRevLett.121.221301`.

[2] Shaul Hanany, Marcelo Alvarez, Emmanuel Artis, et al. "Pico: Probe of Inflation and Cosmic Origins". In: *arXiv e-prints*, arXiv:1902.10541 (Feb. 2019), arXiv:1902.10541. arXiv: `1902.10541 [astro-ph.IM]`.

[3] Maximilian H. Abitbol, Zeeshan Ahmed, Darcy Barron, et al. "Cmb-s4 Technology Book, First Edition". In: *arXiv e-prints*, arXiv:1706.02464 (June 2017), arXiv:1706.02464. arXiv: `1706.02464 [astro-ph.IM]`.

[4] P. Ade, R. W. Aikin, M. Amiri, et al. "Antenna-coupled Tes Bolometers Used In Bicep2, Keck Array, and Spider". In: *The Astrophysical Journal* 812.2 (Oct. 2015), p. 176. DOI: `10.1088/0004-637x/812/2/176`. URL: `https://doi.org/10.1088/0004-637x/812/2/176`.

[5] S. Fatigoni, P. A. R. Ade, Z. Ahmed, et al. "Results and Limits of Time Division Multiplexing for the Bicep Array High Frequency Receivers". In: (2023). arXiv: `2310.10849 [astro-ph.IM]`.

[6] L. Perivolaropoulos and F. Skara. "Challenges for λcdm: An Update". In: *New Astronomy Reviews* 95 (Dec. 2022), p. 101659. ISSN: 1387-6473. DOI: `10.1016/j.newar.2022.101659`. URL: `http://dx.doi.org/10.1016/j.newar.2022.101659`.

[7] Rodrigo Calderon, Arman Shafieloo, Dhiraj Kumar Hazra, et al. "On the Consistency of λcdm With Cmb Measurements In Light of the Latest Planck, Act and Spt Data". In: *Journal of Cosmology and Astroparticle Physics* 2023.08 (Aug. 2023), p. 059. ISSN: 1475-7516. DOI: `10.1088/1475-7516/2023/08/059`. URL: `http://dx.doi.org/10.1088/1475-7516/2023/08/059`.

[8] T. Misner and Wheeler K. Thorne. *Gravitation*. 1973.

[9] P. de Bernardis, P. A. R. Ade, J. J. Bock, et al. "A Flat Universe From High-resolution Maps of the Cosmic Microwave Background Radiation". In: *Nature* 404.6781 (Apr. 2000), pp. 955–959. ISSN: 1476-4687. DOI: `10.1038/35010035`. URL: `http://dx.doi.org/10.1038/35010035`.

[10] P. A. R. Ade, N. Aghanim, M. Arnaud, et al. "Planck 2015 Results: Xiii. Cosmological Parameters". In: *Astronomy & Astrophysics* 594 (Sept. 2016), A13. ISSN: 1432-0746. DOI: `10.1051/0004-6361/201525830`. URL: `http://dx.doi.org/10.1051/0004-6361/201525830`.

[11] Edwin Hubble. “A Relation Between Distance and Radial Velocity Among Extra-galactic Nebulae”. In: *Proceedings of the National Academy of Science* 15.3 (Mar. 1929), pp. 168–173. DOI: `10.1073/pnas.15.3.168`.

[12] D. J. Fixsen. “The Temperature of the Cosmic Microwave Background”. In: *The Astrophysical Journal* 707.2 (Nov. 2009), p. 916. DOI: `10.1088/0004-637x/707/2/916`. URL: `https://dx.doi.org/10.1088/0004-637X/707/2/916`.

[13] A. A. Penzias and R.W. Wilson. “A Measurement of Excess Antenna Temperature At 4080 Mc/s.” In: *Applied Physics Journal* 142 (July 1965), pp. 419–421. DOI: `10.1086/148307`.

[14] Ahmed Zeeshan, BICEP collaboration, et al. “Measurements of Degree-scale B-mode Polarization With the Bicep/keck Experiments At South Pole”. In: *arXiv: Cosmology and Nongalactic Astrophysics* (2018). URL: `https://api.semanticscholar.org/CorpusID:118940114`.

[15] Marc Kamionkowski, Arthur Kosowsky, and Albert Stebbins. “Statistics of Cosmic Microwave Background Polarization”. In: *Phys. Rev. D* 55 (12 June 1997), pp. 7368–7388. DOI: `10.1103/PhysRevD.55.7368`. URL: `https://link.aps.org/doi/10.1103/PhysRevD.55.7368`.

[16] Antony Lewis, Anthony Challinor, and Anthony Lasenby. “Efficient Computation of Cosmic Microwave Background Anisotropies In Closed Friedmann-robertson-walker Models”. In: *The Astrophysical Journal* 538.2 (Aug. 2000), p. 473. DOI: `10.1086/309179`. URL: `https://dx.doi.org/10.1086/309179`.

[17] Marc Kamionkowski and Ely D. Kovetz. “The Quest for B Modes From Inflationary Gravitational Waves”. In: *Annual Review of Astronomy and Astrophysics* 54.Volume 54, 2016 (2016), pp. 227–269. ISSN: 1545-4282. DOI: `https://doi.org/10.1146/annurev-astro-081915-023433`. URL: `https://www.annualreviews.org/content/journals/10.1146/annurev-astro-081915-023433`.

[18] Matias Zaldarriaga and Uro Seljak. “All-sky Analysis of Polarization In the Microwave Background”. In: *Phys. Rev. D* 55 (4 Feb. 1997), pp. 1830–1840. DOI: `10.1103/PhysRevD.55.1830`. URL: `https://link.aps.org/doi/10.1103/PhysRevD.55.1830`.

[19] P.J.E Peebles. *Principles of Physical Cosmology*. Vol. 99. Princeton University Press, 2019. ISBN: 9780691209814. URL: `http://www.jstor.org/stable/j.ctvxrpxvb` (visited on 04/11/2024).

[20] L. H. Ford. “Inflation Driven By A Vector Field”. In: *Phys. Rev. D* 40 (4 Aug. 1989), pp. 967–972. DOI: `10.1103/PhysRevD.40.967`. URL: `https://link.aps.org/doi/10.1103/PhysRevD.40.967`.

[21] Scott Dodelson. *Modern Cosmology*. Academic Press, Elsevier Science, 2003.

[22] Y. Akrami, F. Arroja, M. Ashdown, et al. "Planck2018 Results: Constraints on Inflation". In: *Astronomy & Astrophysics* 641 (Sept. 2020), A10. ISSN: 1432-0746. DOI: `10.1051/0004-6361/201833887`. URL: `http://dx.doi.org/10.1051/0004-6361/201833887`.

[23] P. Ade, Z. Ahmed, M. Amiri, et al. "Improved Constraints on Primordial Gravitational Waves Using Planck, Wmap, and Bicep/keck Observations Through the 2018 Observing Season". In: *Physical Letter Review* 127 (15 Oct. 2021), p. 151301. DOI: `10.1103/PhysRevLett.127.151301`. URL: `https://link.aps.org/doi/10.1103/PhysRevLett.127.151301`.

[24] Katherine Freese. *Natural Inflation.* 1993. DOI: `https://doi.org/10.48550/arXiv.astro-ph/9310012`. arXiv: `astro-ph/9310012 [astro-ph]`.

[25] N. Aghanim, Y. Akrami, M. Ashdown, et al. "Planck2018 Results: Viii. Gravitational Lensing". In: *Astronomy & Astrophysics* 641 (Sept. 2020), A8. ISSN: 1432-0746. DOI: `10.1051/0004-6361/201833886`. URL: `http://dx.doi.org/10.1051/0004-6361/201833886`.

[26] Ioana A. Zelko and Douglas P. Finkbeiner. "Impact of Dust on Spectral Distortion Measurements of the Cosmic Microwave Background". In: *The Astrophysical Journal* 914.1 (June 2021), p. 68. ISSN: 1538-4357. DOI: `10.3847/1538-4357/abfa12`. URL: `http://dx.doi.org/10.3847/1538-4357/abfa12`.

[27] François-Xavier Désert. "The Interstellar Dust Emission Spectrum: Going Beyond the Single-temperature Grey Body". In: *Astronomy &; Astrophysics* 659 (Mar. 2022), A70. ISSN: 1432-0746. DOI: `10.1051/0004-6361/202142617`. URL: `http://dx.doi.org/10.1051/0004-6361/202142617`.

[28] N. Aghanim, Y. Akrami, M. I. R. Alves, et al. "Planck2018 Results: Xii. Galactic Astrophysics Using Polarized Dust Emission". In: *Astronomy & Astrophysics* 641 (Sept. 2020), A12. ISSN: 1432-0746. DOI: `10.1051/0004-6361/201833885`. URL: `http://dx.doi.org/10.1051/0004-6361/201833885`.

[29] K. C. Westfold. "The Polarization of Synchrotron Radiation." In: *Applied Physics Journal* 130 (July 1959), p. 241. DOI: `10.1086/146713`.

[30] D. de Burca and A. Shearer. "Circular Polarization of Synchrotron Radiation In High Magnetic Fields". In: *Monthly Notices of the Royal Astronomical Society* 450.1 (Apr. 2015), pp. 533–540. ISSN: 0035-8711. DOI: `10.1093/mnras/stv576`. eprint: `https://academic.oup.com/mnras/article-pdf/450/1/533/18753616/stv576.pdf`. URL: `https://doi.org/10.1093/mnras/stv576`.

[31] P. A. R. Ade, Z. Ahmed, R. W. Aikin, et al. "Constraints on Primordial Gravitational Waves Using *planck*, Wmap, and New Bicep2/*keck* Observations Through the 2015 Season". In: *Phys. Rev. Lett.* 121 (22 Nov. 2018), p. 221301. DOI: `10.1103/PhysRevLett.121.221301`. URL: `https://link.aps.org/doi/10.1103/PhysRevLett.121.221301`.

[32] A. Schillaci, P. A. R. Ade, Z. Ahmed, et al. "Design and Performance of the First Bicep Array Receiver". In: *Journal of Low Temperature Physics* 199.3–4 (Feb. 2020), pp. 976–984. ISSN: 1573-7357. DOI: `10.1007/s10909-020-02394-6`. URL: `http://dx.doi.org/10.1007/s10909-020-02394-6`.

[33] K.D. Irwin and G.C. Hilton. "Transition-edge Sensors". In: *Cryogenic Particle Detection*. Ed. by Christian Enss. Berlin, Heidelberg: Springer Berlin Heidelberg, 2005, pp. 63–150. ISBN: 978-3-540-31478-3. DOI: `10.1007/10933596_3`. URL: `https://doi.org/10.1007/10933596_3`.

[34] C. Zhang et al. "Characterizing the Sensitivity of 40 Ghz Tes Bolometers for Bicep Array". In: *J. Low Temp. Phys.* 199.3-4 (2020), pp. 968–975. DOI: `10.1007/s10909-020-02411-8`. arXiv: `2002.05219 [astro-ph.IM]`.

[35] Kevork Abazajian, Arwa Abdulghafour, Graeme E. Addison, et al. *Snowmass 2021 Cmb-s4 White Paper*. 2022. arXiv: `2203.08024 [astro-ph.CO]`.

[36] Maximilian H. Abitbol, Zeeshan Ahmed, Darcy Barron, et al. *Cmb-s4 Technology Book, First Edition*. 2017. arXiv: `1706.02464 [astro-ph.IM]`.

[37] National Academies of Sciences Engineering and Medicine. *Pathways To Discovery In Astronomy and Astrophysics for the 2020s*. Washington, DC: The National Academies Press, 2023. ISBN: 978-0-309-46734-6. DOI: `10.17226/26141`. URL: `https://nap.nationalacademies.org/catalog/26141/pathways-to-discovery-in-astronomy-and-astrophysics-for-the-2020s`.

[38] M. Crumrine, P. A. R. Ade, Z. Ahmed, et al. *Bicep Array Cryostat and Mount Design*. 2018. arXiv: `1808.00569 [astro-ph.IM]`.

[39] C. L. Kuo, J. J. Bock, J. A. Bonetti, et al. "Antenna-coupled Tes Bolometer Arrays for Cmb Polarimetry". In: *Millimeter and Submillimeter Detectors and Instrumentation for Astronomy Iv*. Ed. by William D. Duncan et al. Spie, Aug. 2008. DOI: `10.1117/12.788588`. URL: `http://dx.doi.org/10.1117/12.788588`.

[40] Albert Wandui. "Albert Thesis on the Development of Tkids". Available on the Caltech thesis public release portal upon release. PhD thesis. 1200 E California Blvd. Pasadena, 91125, CA: California Institute of Technology, July 2024.

[41] Albert K. Wandui, James J. Bock, Clifford Frez, et al. "Antenna-coupled Thermal Kinetic Inductance Detectors for Ground-based Millimeter-wave Cosmology". In: *Millimeter, Submillimeter, and Far-infrared Detectors and Instrumentation for Astronomy X*. Ed. by Jonas Zmuidzinas and Jian-Rong Gao. Vol. 11453. International Society for Optics and Photonics. Spie, 2020, 114531e. DOI: `10.1117/12.2563373`. URL: `https://doi.org/10.1117/12.2563373`.

[42] P. A. R. Ade, R. W. Aikin, M. Amiri, et al. "BICEP2. II. Experiment and Three-year Data Set". In: *The Astrophysical Journal* 792.1 (Aug. 2014), p. 62. ISSN: 1538-4357. DOI: `10.1088/0004-637x/792/1/62`. URL: `http://dx.doi.org/10.1088/0004-637X/792/1/62`.

[43] Albert Wandui, James J. Bock, Clifford Frez, et al. "Thermal Kinetic Inductance Detectors for Millimeter-wave Detection". In: *Journal of Applied Physics* 128.4 (July 2020), p. 044508. ISSN: 0021-8979. DOI: `10.1063/5.0002413`. eprint: `https://pubs.aip.org/aip/jap/article-pdf/doi/10.1063/5.0002413/15252752/044508\_1\_online.pdf`. URL: `https://doi.org/10.1063/5.0002413`.

[44] Randol W. Aikin, P. A. Ade, S. Benton, et al. "Optical Performance of the Bicep2 Telescope At the South Pole". In: *Millimeter, Submillimeter, and Far-infrared Detectors and Instrumentation for Astronomy V*. Ed. by Wayne S. Holland and Jonas Zmuidzinas. Vol. 7741. International Society for Optics and Photonics. Spie, 2010, p. 77410v. DOI: `10.1117/12.857868`. URL: `https://doi.org/10.1117/12.857868`.

[45] Peter Day, Henry Leduc, Benjamin Mazin, et al. "A Broadband Superconducting Detector Suitable for Use In Large Arrays". In: *Nature* 425 (Oct. 2003), pp. 817–21. DOI: `10.1038/nature02037`.

[46] Megan E. Eckart, B. A. Mazin, B. Bumble, et al. "Microwave Kinetic Inductance Detectors: Large Format X-ray Spectral Imagers for the Next Generation of X-ray Telescopes". In: *Aas/high Energy Astrophysics Division #9*. Vol. 9. AAS/High Energy Astrophysics Division. Sept. 2006, 18.19, p. 18.19.

[47] J.E. Sauvageau and D.G. McDonald. "Superconducting Kinetic Inductance Bolometer". In: *IEEE Transactions on Magnetics* 25.2 (1989), pp. 1331–1334. DOI: `10.1109/20.92541`.

[48] A. Giachero, A. Cruciani, A. D'Addabbo, et al. "Development of Thermal Kinetic Inductance Detectors Suitable for X-ray Spectroscopy". In: *Journal of Low Temperature Physics* 193.3–4 (July 2018), pp. 163–169. ISSN: 1573-7357. DOI: `10.1007/s10909-018-2043-8`. URL: `http://dx.doi.org/10.1007/s10909-018-2043-8`.

[49] Andrey V Timofeev, Visa Vesterinen, Panu Helistö, et al. "Submillimeter-wave Kinetic Inductance Bolometers on Free-standing Nanomembranes". In: *Superconductor Science and Technology* 27.2 (Dec. 2013), p. 025002. DOI: `10.1088/0953-2048/27/2/025002`. URL: `https://dx.doi.org/10.1088/0953-2048/27/2/025002`.

[50] S. Pirro and P. Mauskopf. "Advances In Bolometer Technology for Fundamental Physics". In: *Annual Review of Nuclear and Particle Science* 67.Volume 67, 2017 (2017), pp. 161–181. ISSN: 1545-4134. DOI: `https://doi.org/10.1146/annurev-nucl-101916-123130`. URL: `https://www.annualreviews.org/content/journals/10.1146/annurev-nucl-101916-123130`.

[51] John C. Mather. "Bolometer Noise: Nonequilibrium Theory". In: *Appl. Opt.* 21.6 (Mar. 1982), pp. 1125–1129. DOI: `10.1364/ao.21.001125`. URL: `https://opg.optica.org/ao/abstract.cfm?URI=ao-21-6-1125`.

[52] John C. Mather. "Bolometers: Ultimate Sensitivity, Optimization, and Amplifier Coupling". In: *Appl. Opt.* 23.4 (Feb. 1984), pp. 584–588. DOI: `10.1364/ao.23.000584`. URL: `https://opg.optica.org/ao/abstract.cfm?URI=ao-23-4-584`.

[53] P. L. Richards. "Bolometers for Infrared and Millimeter Waves". In: *Journal of Applied Physics* 76.1 (July 1994), pp. 1–24. ISSN: 0021-8979. DOI: `10.1063/1.357128`. eprint: `https://pubs.aip.org/aip/jap/article-pdf/76/1/1/18668463/1\_1\_online.pdf`. URL: `https://doi.org/10.1063/1.357128`.

[54] Jonas Zmuidzinas. "Superconducting Microresonators: Physics and Applications". In: *Annual Review of Condensed Matter Physics* 3.Volume 3, 2012 (2012), pp. 169–214. ISSN: 1947-5462. DOI: `https://doi.org/10.1146/annurev-conmatphys-020911-125022`. URL: `https://www.annualreviews.org/content/journals/10.1146/annurev-conmatphys-020911-125022`.

[55] Michael Tinkham. *Introduction To Superconductivity*. Courier Corporation, 2004.

[56] C. M. Wilson and D. E. Prober. "Quasiparticle Number Fluctuations In Superconductors". In: *Physical Review B* 69.9 (2004), p. 094524.

[57] P. D. Mauskopf. "Transition Edge Sensors and Kinetic Inductance Detectors In Astronomical Instruments". In: *Publications of the Astronomical Society of the Pacific* 130.990 (2018), p. 082001.

[58] H McCarrick, D Flanigan, G Jones, et al. "Horn-coupled, Commercially-fabricated Aluminum Lumped-element Kinetic Inductance Detectors for Millimeter Wavelengths". In: *Review of Scientific Instruments* 85.12 (2014).

[59] Jiansong Gao. “The Physics of Superconducting Microwave Resonators”. PhD thesis. California Institute of Technology, 2008. URL: `https://resolver.caltech.edu/CaltechETD:etd-06092008-235549`.

[60] Jiansong Gao, Miguel Daal, Anastasios Vayonakis, et al. “Experimental Evidence for A Surface Distribution of Two-level Systems In Superconducting Lithographed Microwave Resonators”. In: *Applied Physics Letters* 92.15 (2008), p. 152505. DOI: `10.1063/1.2906373`. eprint: `https://doi.org/10.1063/1.2906373`. URL: `https://doi.org/10.1063/1.2906373`.

[61] Michael L. Waskom. “Seaborn: Statistical Data Visualization”. In: *Journal of Open Source Software* 6.60 (2021), p. 3021. DOI: `10.21105/joss.03021`. URL: `https://doi.org/10.21105/joss.03021`.

[62] James C. Rautio. “Recent Technology Developments In the Sonnet Suites of Planar Electromagnetic Analysis Software”. In: *2011 Ieee International Symposium on Antennas and Propagation (apsursi)*. 2011, pp. 2720–2723. DOI: `10.1109/aps.2011.5997087`.

[63] Vanessa Bohm and Jia Liu. *Impact of Covid-19 on Astronomy: Two Years In*. 2022. DOI: `https://doi.org/10.48550/arXiv.2203.15621`. arXiv: `2203.15621 [astro-ph.IM]`.

[64] *Hpd Rainier 103 Adr Cryostat*. `https://www.formfactor.com/download/hpd-rainier-103-adr-cryostat-datasheet/`. Accessed: 2024-05-07.

[65] *Pt407 Cryocoolers*. `https://bluefors.com/products/pulse-tube-cryocoolers/pt407-pulse-tube-cryocooler/`. Accessed: 2024-05-07.

[66] *Niobium-titanium Cables*. `https://www.bruker.com/en/products-and-solutions/superconductors/superconductors/niobium-titanium-superconductor.html`. Accessed: 2024-05-07.

[67] C. Sheehy, Peter Ade, R. Aikin, et al. “The Keck Array: A Pulse Tube Cooled Cmb Polarimeter”. In: *Proceedings of SPIE - The International Society for Optical Engineering* 7741 (Apr. 2011). DOI: `10.1117/12.857871`.

[68] D. Singh, A. Pandey, M.K. Singh, et al. “Heat Radiation Reduction In Cryostats With Multilayer Insulation Technique”. In: *Journal of Instrumentation* 15.07 (July 2020), P07032–p07032. ISSN: 1748-0221. DOI: `10.1088/1748-0221/15/07/p07032`. URL: `http://dx.doi.org/10.1088/1748-0221/15/07/P07032`.

[69] R.S. Bhatia, S.T. Chase, S.F. Edgington, et al. “A Three-stage Helium Sorption Refrigerator for Cooling of Infrared Detectors To 280 Mk”. In: *Cryogenics* 40.11 (2000), pp. 685–691. ISSN: 0011-2275. DOI: `https://doi.org/10.1016/S0011-2275(00)00072-2`. URL: `https://www.sciencedirect.com/science/article/pii/S0011227500000722`.

[70] *Chase Helium Refrigerators*. `https://www.chasecryogenics.com/products`. Accessed: 2024-05-08.

[71] D. Flanigan, B. R. Johnson, M. H. Abitbol, et al. "Magnetic Field Dependence of the Internal Quality Factor and Noise Performance of Lumped-element Kinetic Inductance Detectors". In: *Applied Physics Letters* 109.14 (Oct. 2016). ISSN: 1077-3118. DOI: `10.1063/1.4964119`. URL: `http://dx.doi.org/10.1063/1.4964119`.

[72] *Lakeshore 370 Ac Resistance Bridge*. `https://www.lakeshore.com/products/categories/overview/discontinued-products/discontinued-products/model-370-ac-resistance-bridge-`. Accessed: 2024-05-09.

[73] *Model 218 Cryogenic Temperature Monitor*. `https://www.lakeshore.com/products/categories/overview/temperature-products/cryogenic-temperature-monitors/model-218-temperature-monitor`. Accessed: 2024-05-09.

[74] *Custom Cable Assembly Supplyer*. `https://www.pickeringtest.com/en-us/products/connectivity-cables/cables-connectors`. Accessed: 2024-05-10.

[75] Jonathon Robert Hunacek. "Time: A Millimeter-wavelength Grating Spectrometer Array for [cii] / Co Intensity Mapping". `https://thesis.library.caltech.edu/13683/1/thesis-jhunacek-20200427b.pdf`. PhD thesis. 1200 E California Blvd. Pasadena, 91125, CA: California Institute of Technology, Apr. 2020.

[76] Haishan Cao, Biqiang Liu, and Lingxiao Qin. "Sorption Cryogenic Cooling: Fundamentals, Progress, and Outlook". In: *Applied Thermal Engineering* 213 (2022), p. 118680. ISSN: 1359-4311. DOI: `https://doi.org/10.1016/j.applthermaleng.2022.118680`. URL: `https://www.sciencedirect.com/science/article/pii/S135943112200624X`.

[77] *Lt30xx Chip Family Datasheets*. `https://www.analog.com/en/products/lt3045.html`. Accessed: 2024-05-10.

[78] C.K. Boggs, A.D. Doak, and F.L. Walls. "Measurement of Voltage Noise In Chemical Batteries". In: *Proceedings of the 1995 Ieee International Frequency Control Symposium (49th Annual Symposium)*. 1995, pp. 367–373. DOI: `10.1109/freq.1995.483923`.

[79] *Lt66xx Chip Family Datasheets*. `https://www.analog.com/en/products/ltc6655.html`. Accessed: 2024-05-10.

[80] *Delft Circuit Cryoflex Products*. `https://delft-circuits.com/cri-oflex-technology/core-technology/`. Accessed: 2024-05-11.

[81] *Low Noise Amplifier Datasheet*. `https://www.cosmicmicrowavetechnology.com/`. Accessed: 2024-05-11.

[82] Sander Weinreb, Joseph C. Bardin, and Hamdi Mani. “Design of Cryogenic Sige Low-noise Amplifiers”. In: *IEEE Transactions on Microwave Theory and Techniques* 55.11 (2007), pp. 2306–2312. DOI: `10.1109/tmtt.2007.907729`.

[83] *Ettus Research N321.* `https://www.ettus.com/all-products/usrp-n321/`. Accessed: 2024-03-30.

[84] *Low Temperature Rf Laminates for Pcb Fabrication.* `https://www.rogerscorp.com/advanced-electronics-solutions/ro4000-series-laminates`. Accessed: 2024-05-11.

[85] A. Paghi, G. Trupiano, C. Puglia, et al. *Estimation of the Fr4 Microwave Dielectric Properties At Cryogenic Temperature for Quantum-chip-interface Pcbs Design.* 2023. arXiv: `2310.01171 [physics.ins-det]`.

[86] Philip R. Maloney, Nicole G. Czakon, Peter K. Day, et al. “Music for Sub-/millimeter Astrophysics”. In: *Millimeter, Submillimeter, and Far-infrared Detectors and Instrumentation for Astronomy V*. Ed. by Wayne S. Holland and Jonas Zmuidzinas. Vol. 7741. International Society for Optics and Photonics. Spie, 2010, 77410f. DOI: `10.1117/12.857751`. URL: `https://doi.org/10.1117/12.857751`.

[87] Lorenzo Minutolo, Bryan Steinbach, Albert Wandui, et al. “A Flexible Gpu-accelerated Radio-frequency Readout for Superconducting Detectors”. In: *IEEE Transactions on Applied Superconductivity* 29.5 (2019), pp. 1–5. DOI: `10.1109/tasc.2019.2912027`.

[88] *Original Repository of the Gpu_sdr System.* `https://github.com/nasa/GPU_SDR`. Accessed: 2024-05-11.

[89] *Maintained Repository of the Gpu_sdr System.* `https://github.com/LorenzoMinutolo/GPU_SDR`. Accessed: 2024-05-11.

[90] Michael M. Madden. “Challenges Using Linux As A Real-time Operating System”. In: *Aiaa Scitech 2019 Forum.* DOI: `10.2514/6.2019-0502`. eprint: `https://arc.aiaa.org/doi/pdf/10.2514/6.2019-0502`. URL: `https://arc.aiaa.org/doi/abs/10.2514/6.2019-0502`.

[91] Brand Fortner. “Hdf: the Hierarchical Data Format”. In: *Dr Dobb’s J Software Tools Prof Program* 23.5 (1998), p. 42.

[92] Shubh Agrawal, Bryan Steinbach, James J. Bock, et al. “Strong Negative Electrothermal Feedback In Thermal Kinetic Inductance Detectors”. In: *Journal of Applied Physics* 130.12 (Sept. 2021), p. 124503. ISSN: 0021-8979. DOI: `10.1063/5.0064723`. eprint: `https://pubs.aip.org/aip/jap/article-pdf/doi/10.1063/5.0064723/13254302/124503\_1\_online.pdf`. URL: `https://doi.org/10.1063/5.0064723`.

[93] Cyndia Yu, Zeeshan Ahmed, Josef C. Frisch, et al. “Slac Microresonator Rf (smurf) Electronics: A Tone-tracking Readout System for Superconducting Microwave Resonator Arrays”. In: *Review of Scientific Instruments* 94.1 (Jan. 2023). issn: 1089-7623. doi: `10.1063/5.0125084`. url: `http://dx.doi.org/10.1063/5.0125084`.

[94] *Rfnoc Frsamework*. `https://kb.ettus.com/Getting_Started_with_RFNoC_Development`. Accessed: 2024-03-30.

[95] Lyle Ramshaw and Robert E. Tarjan. “A Weight-scaling Algorithm for Min-cost Imperfect Matchings In Bipartite Graphs”. In: *2012 Ieee 53rd Annual Symposium on Foundations of Computer Science*. 2012, pp. 581–590. doi: `10.1109/focs.2012.9`.

[96] Bryan Steinbach, Lorenzo Minutolo, and et al. Wandui Albert. “Chirped Pulsed Readout of Thermal Kinetic Inductance Detectors”. In: *N/d* ().

[97] Tyler St Germaine, P.A.R. Ade, Zeeshan Ahmed, et al. “Analysis of Temperature-to-polarization Leakage In Bicep3 and Keck Cmb Data From 2016 To 2018”. In: *Millimeter, Submillimeter, and Far-infrared Detectors and Instrumentation for Astronomy X*. Ed. by Jonas Zmuidzinas and Jian-Rong Gao. Spie, Dec. 2020. doi: `10.1117/12.2562729`. url: `http://dx.doi.org/10.1117/12.2562729`.

[98] C. L. Kuo, J. J. Bock, and J. A. Bonetti et al. “Antenna-coupled Tes Bolometer Arrays for Cmb Polarimetry”. In: *Millimeter and Submillimeter Detectors and Instrumentation for Astronomy Iv*. Ed. by William D. Duncan et al. Vol. 7020. International Society for Optics and Photonics. Spie, 2008, p. 70201i. doi: `10.1117/12.788588`. url: `https://doi.org/10.1117/12.788588`.

[99] Lorenzo Minutolo, Albert Wandui, and James J. et al Bock. “Thermal Kinetic Inductance Detectors Camera: System Level Design, Strategy and Performance Forecast”. In: *IEEE Transactions on Applied Superconductivity* 31.5 (2021), pp. 1–4. doi: `10.1109/tasc.2021.3069732`.

[100] T. St Germaine, P. A. R. Ade, and M. et al Amiri. “Optical Characterization of the Keck Array and Bicep3 Cmb Polarimeters From 2016 To 2019”. In: *Journal of Low Temperature Physics* 199.3–4 (Feb. 2020), pp. 824–832. issn: 1573-7357. doi: `10.1007/s10909-020-02392-8`. url: `http://dx.doi.org/10.1007/s10909-020-02392-8`.

[101] Peter Griffiths and James Haseth. *Fourier Transform Infrared Spectrometry, Second Edition*. June 2006, pp. 112–114. isbn: 9780471194040. doi: `10.1002/9780470106310.ch9`.

[102] A.H. Abdelhameed, G. Angloher, and et al. Bauer. “First Results From the Cresst-iii Low-mass Dark Matter Program”. In: *Physical Review D* 100.10 (Nov. 2019). issn: 2470-0029. doi: `10.1103/physrevd.100.102002`. url: `http://dx.doi.org/10.1103/PhysRevD.100.102002`.

[103] B. A. Steinbach, J. J. Bock, H. T. Nguyen, et al. “Thermal Kinetic Inductance Detectors for Ground-based Millimeter-wave Cosmology”. In: *Journal of Low Temperature Physics* 193.3-4 (Nov. 2018), pp. 88–95. doi: `10.1007/s10909-018-2016-y`. arXiv: `1803.06413 [astro-ph.IM]`.